Exploring the relative polarization of the two photons from para-positronium decays using GEANT4 simulation toolkit

A Thesis

submitted to
Indian Institute of Science Education and Research Pune
in partial fulfillment of the requirements for the
MS Degree Programme

by

Chetan Agrawal

Registration Number

20222009

Supervisor: Prof. Seema Sharma

Indian Institute of Science Education and Research Pune
Dr. Homi Bhabha Road,
Pashan, Pune 411008, INDIA.

December 2025

Certificate

This is to certify that this dissertation entitled **"Exploring the relative polarization of the two photons from para-positronium decays using GEANT4 simulation toolkit"** towards the partial fulfillment of the MS degree program at the Indian Institute of Science Education and Research, Pune represents study/work carried out by Chetan Agrawal at Indian Institute of Science Education and Research under the supervision of Prof. Seema Sharma, Professor, Department of Physics , during the academic year 2024-2025.

Supervisor
Prof. Seema Sharma
Professor
IISER Pune

Expert
Prof. Bhas Bapat
Professor
IISER Pune

Declaration

I hereby declare that the matter embodied in the report entitled **"Exploring the relative polarization of the two photons from para-positronium decays using GEANT4 simulation toolkit "**, are the results of the work carried out by me at the Department of Physics, Indian Institute of Science Education and Research, Pune, under the supervision of Prof. Seema Sharma and the same has not been submitted elsewhere for any other degree.

Chetan Agrawal
MS student (20222009)
IISER Pune

Contents

List of Figures

List of Tables

Acknowledgments

First and foremost, I would like to extend my heartfelt thanks to my supervisor, Professor Seema Sharma at the Indian Institute of Science Education and Research (IISER) Pune, for her unwavering support, insightful guidance, and continuous encouragement. Her expertise, patience, and dedication have been instrumental in shaping this project and my overall academic growth.

I am deeply grateful to my thesis advisory committee member, Professor Bhas Bapat at IISER Pune, for mentoring me through different stages of my project and offering valuable feedback during the evaluation process.

I am also sincerely thankful to Dr. Rajdeep Mohan Chatterji at Tata Institute of Fundamental Research (TIFR), Mumbai for closely following my work and for his valuable time, discussions, and feedback at various stages. I would further like to thank Dr. Tuhin Roy, Dr. Shilpi Jain, Dr. Rudrajyoti Palit and all other collaborators at TIFR, Mumbai, for their discussions on the theoretical aspects of positronium physics as well as the challenges for designing the detectors to study the positronium decay.

I gratefully acknowledge the Ministry of Education, Government of India, for the financial support provided through the institute fellowship at IISER Pune. This fellowship has offered crucial economic support, enabling me to pursue my studies and research at IISER.

My heartfelt thanks go to my seniors, Alpana and Bhumika, for their invaluable assistance in getting familiar with analysis methodologies and the tools essential for my research. Their patient guidance laid a strong foundation for my work. I also extend my gratitude to my lab members — Tanay, Somanko, Bapi, Archana, and others, for their insightful discussions and contributions during our group meetings, which significantly enriched my research experience.

I am profoundly thankful to my parents, Shri Biharilal Agrawal and Smt. Kiran Lata Agrawal, for their unconditional love, constant support, and encouragement, and to my elder sister, Ms. Srishti Agrawal, supporting me different at stages in my career and guiding

me since childhood. A special thanks to my colleague and friend Aswini Bala for his valuable discussions and encouragement throughout my coursework and thesis project.

Finally, I would like to acknowledge all my dear friends and seniors at IISER Pune for their camaraderie and support during my time here. I am also grateful to the administrative, technical, security, housekeeping staff at IISER Pune for their very nice behaviour and timely assistance whenever needed throughout my stay at IISER.

–Chetan

Abstract

Quantum Electrodynamics (QED) is an example of success of Quantum Field theory. A positronium atom is a bound state of an electron and positron, which decays to two, three or higher multiplicity of the photons. Being a purely leptonic system, positronium provides a very clean probe for testing the accuracy of QED calculations. Studying the photons from the decay of positronium provides a possibility to search for physics beyond the Standard Model as well as plays a crucial role in medicine and biology also to diagnose the healthiness of the tissue material.

In this thesis we have focused on studying some of the crucial aspects of detection of the photons from the positronium decay using the GEANT4 simulation toolkit. Our studies include the mechanisms by a which a sub MeV range photon deposit its energy in the material, energy resolution and efficiency of the detectors and measuring the polarization of a photon in an experimental setup.

Chapter 1

Introduction

Quantum Electrodynamics (QED) is an example of the success of quantum field theory. Precise measurements of many physical quantities such as anomalous electron and muon magnetic moments, hyperfine splitting of hydrogen, Lamb shift, etc. have provided the values matching with the theoretical predictions to a very high precision.

In addition to annihilation, the interaction between an electron (e^-) and it's antiparticle positron (e^+), can result into a bound state also, known as **positronium**. Such scenario can happen only when the electron and positron are almost at rest, otherwise direct annihilation takes place instead of forming a bound state. Positronium is a very light purely leptonic system, where the only interaction possible between these charged leptons (e^- and e^+) are the electromagnetic and weak interactions. The absence of strong interactions (governed by Quantum Chromodynamics) makes positronium a very clean probe for testing the accuracy of QED calculations for bound states as well as the searches for new physics beyond the standard model.

The positronium system is very unstable (ground state binding Energy 6.8 eV). Positronium atom can decay into two or more photons. Different aspects of the positronium decay such as lifetime, decay modes, spectroscopy, etc has attracted many studies. [15]. Positronium, being a bound state of two fermions can be formed as a spin singlet state ($^1S_0$) known as para-positronium (p-Ps, lifetime 125 ps in vacuum) or as spin triplet state ($^3S_1$) known as ortho-positronium (o-Ps, life time 142 ns in vacuum). The p-Ps has charge conjugation (C) +1. therefore it decays to even number of photons (C = -1). On the other hand o-Ps has charge conjugation -1 so it decays to odd number of photons.

Studies on o-Ps decay caught much attention because of its longer lifetime. At such long time scale, QCD processes doesn't play any role which makes the decay process much

cleaner to analyze. Of particular interest are the invisible decay and production of even number of photons in the decay of o-Ps. Such phenomenons indicate towards some new physics [15] like violation of some basic conservation laws (C,P,T), millicharged particles [16], presence of axion like particles (ALPs) [17] etc. These decay modes also suggest some disappearance mechanisms, such as mirror worlds [18] and extra dimensions [19, 20].

Apart from these exotic things, positronium finds its importance in some very important real life applications also. The mean life time and the formation probability of positronium depends significantly on the molecular environment where positronium is formed. This finds its application in medicine and biology. The positrons emitted from the β decay of some radioactive nuclei like Na-22 can be injected into some tissues to form a positronium atom there. Studying the photons from the decay of that positronium can help to diagnose the healthiness of the tissue material [21].

Looking at such a wide range of interesting aspects of positronium decay, I was excited to study the photons from decay of positronium in GEANT4 simulation. In this thesis, we have presented our work on studying some of the crucial aspects of detection of the photons (similar to the one from p-Ps decay) such as mechanisms by a which a sub MeV range photon deposit its energy in the material, energy resolution and efficiency of the detectors, measuring the polarization of a photon in an experimental setup.

In chapter 2 of this thesis, we have given an overview of workflow in GEANT4 simulation toolkit and have and explained some important aspects of a detector simulation program. In chapter 3, first we briefly introduce the mechanisms by which a sub MeV energy range photon deposits its energy inside the material. Following that we have presented our work to study how the probability of these mechanism depend on different factors such as incident photon energy, detector material and material thickness. In the same chapter, we have also presented our work on studying the energy resolution and efficiency of scintillator detectors using the distribution of scintillation photons produced in the material. We have also shown there that how resolution and efficiency of the detector gets affected by the detector material, material thickness and the energy of the incident photons. In chapter 4, we discuss the polarization aspect of Compton scattering and using it as a tool to experimentally measure the polarization of the incoming photons. There we have presented our studies in a J-PET like detector geometry in the simulation for two different cases having single and two photon events.

Chapter 2

GEANT4: A toolkit for detector simulation

Over the past three decades, the success of international high-energy physics (HEP) experimental programs such as CMS [22] and ATLAS [23] at Large Hadron Collider [24], CERN [25], Geneva, has depended heavily upon the precise simulation of particle-matter interactions and the modeling of detector geometries. This is evident by the fact that they produced physics results of exceptional quality more quickly than any previous hadron collider experiment [2]. For an instance, simulations provided physicists with insights into the signatures the Higgs boson might produce in the proton-proton collision data obtained by these experiments, as well as the methods for identifying them within extensive datasets.

Modern nuclear and particle physics experiments frequently feature complex combinations of detector technologies and their sizes. When the experiments are not feasible or are not practicable due to their expense and complexity, simulation tools can be useful for providing information on system design and for optimizing the system performance.

GEANT4: a detector simulation toolkit

GEANT4 (**GE**ometry **AN**d **T**racking) [26] is a detector simulation toolkit which was developed as a collaborative effort of the two groups led by CERN [25] and KEK [27] in 1990s. In the past, outcome of detectors in experiments were modeled using simple analytic or back-of-the-envelope calculations, toy simulations, or parametrization based on theoretical predictions.

The development of GEANT can be traced back to the release of GEANT1 in 1975. It

provided a user-defined output with histograms and it was driven by a very simple framework. A more comprehensive collection of physics models, including multiple scattering, particle decay, energy loss, and electromagnetic (EM) showers based on a subset of the Electron Gamma Shower (EGS) package, were then included in GEANT2, which was released in 1976. In 1980 the breakthrough came with GEANT3, which was an upgrade of the GEANT2 program and included a data structure to describe the complicated geometries at the level needed by the experiments at that time. Various experiments at Large Electron Positron Collider (LEP) used GEANT3 for modelling their detectors. In 1993, following the success of GEANT3, the two groups at CERN and KEK started a collaboration to use different computing techniques available that time for improvements in the GEANT3 program. Thus, the development of GEANT4 got started.

Status of GEANT4

GEANT4 is a collection of C++ class libraries, which extensively uses the object oriented programming and MC simulation to model the tracing of particles through matter. Being a toolkit, GEANT4 allows the experimenters to have a complete control over defining geometry, material specifications, and external fields. Apart from this, GEANT4 gives the users ways to track particles by means of well-defined physics list composed of a subset of many available physics models in various combinations, to visualize the interactions and derive the intended simulated data. The GEANT4 [28] simulation toolkit serves as the foundation for detector simulation in the most recent experiments.

Applications of the GEANT4 toolkit span a broad spectrum of dimensions and energies, ranging from nanometers to planetary scales in lengths and from eV to PeV in energies. Apart from using GEANT4 as a tool for detector and background simulation in High Energy Physics experiments (see an example in Fig. 2.1), the scope of application of GEANT4 has been quickly widened to nuclear physics experiments, simulation of accelerator setups, studies in medical imaging and treatment, simulation of space radiation and its effects on spacecraft instruments.

Apart from GEANT4, there are other simulation tools also available, such as FLUKA [29] and MARS [30]. FLUKA is a comprehensive particle physics modeling program with numerous uses in shielding, HEP and engineering, dosimetry, medical physics, radiobiology, cosmic ray research, detector and telescope design, and more. The MARS is a software package, which is widely used to model enclosures having radiation shielding.

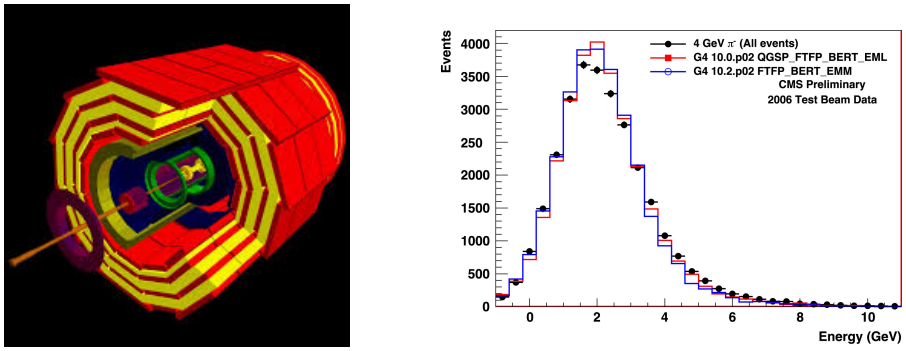

(a) (b)

Figure 2.1: (a) A visualization of the full detector geometry of the CMS detector in GEANT4 simulation [1], (b) Plot showing the measurements of response function for 4 GeV pions incident onto a solid angle slice of the CMS Electromagnetic Calorimeter [2]. The plot compares the 2006 CMS test beam data measurements with GEANT4 simulation with two different choices of physics lists.

2.1 Some key building blocks of a GEANT4 simulation program

GEANT4 extensively utilizes the object oriented programming to create a structure of class categories which are at the heart of simulation program. Using such an approach provides a modular structure of various components in the simulation code, which gives user an ease of adding new stuff without changing everything in the code. Fig. 2.2 shows the different class categories in GEANT4 and the relationship among them. As shown in the figure, a class category is represented by a box and its relation to another class category is represented by a straight line. Each straight line contains a blob which means that the class category which has this blob uses the category from where the straight line is drawn [26].

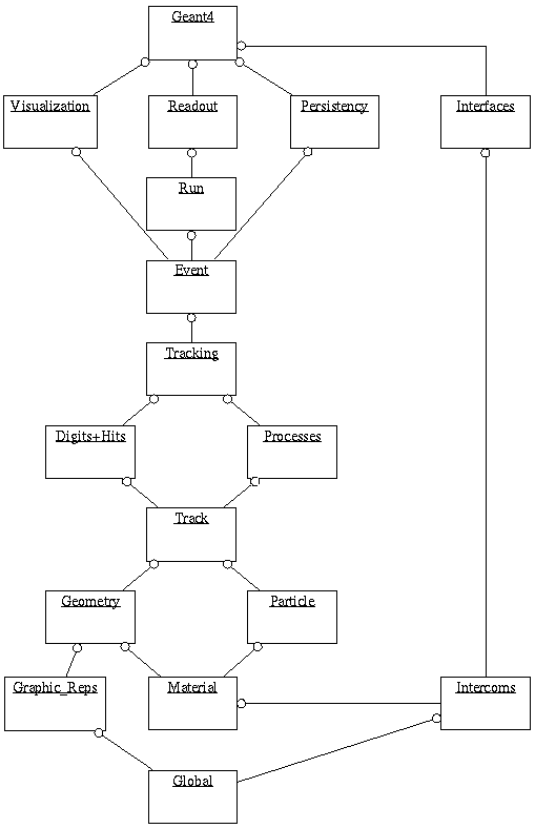

Figure 2.2: Hierarchy of different classes in GEANT4

Following is the description of some of the key class categories shown in class category diagram shown in Fig. 2.2:

- **Kernel:** GEANT4 kernel initializes and manages the run configurations, handles particles, tracks and materials, and enables the simulation of the physics processes. Kernel also enables the user to visualize the setup and the particle trajectories in events using various graphical visualization systems[31].

- **Run:** The largest unit of simulation is a 'Run' which is represented by 'G4Run' class object. A run is a collection of events within which particle source, the detector geometry and the set of physics processes etc are configured by the user [31] (See Fig. 2.4a). Once a run is started these things cannot be changed in between by the user.

- **Event:** An 'Event' is the basic unit of simulation.'G4Event' class object represents an event which contains all the inputs and outputs from the detector components (See

Fig. 2.4b). For example in our simulation, shooting one photon from the gun initiates an event and the completion of tracking of primary photon and all the secondary particles produced finishes that event.

Stacking mechanism in an event: Primary particles are generated at the beginning of an event. After that these particles are kept in a 'stack' and gets popped up one by one and traced through the detector volumes. If there are secondary tracks produced while tracing of the primary particles, they are also pushed into the stack. Those secondary tracks pops up from the stack one by one after the tracking of primary particle gets completed. An event is processed until the stack becomes empty.

A stack in GEANT4 works in a simple "last-in-first-out" mode, i.e. the particle which is produced later, pops up from the stack first. Fig 2.3 shows the tracking of a particle where secondaries are produced at multiple steps. The order of tracking is as follows:

$$T_1 \rightarrow T_3 \rightarrow T_5 \rightarrow T_7 \rightarrow T_4 \rightarrow T_6 \rightarrow T_2.$$

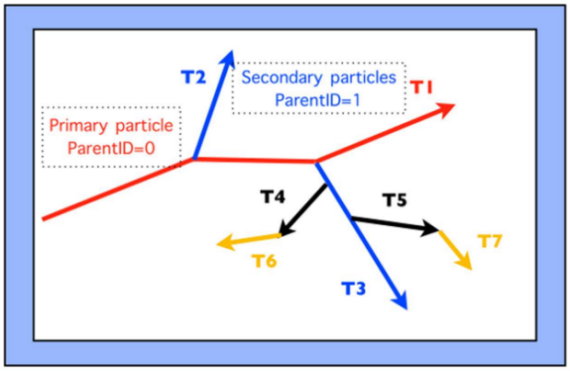

Figure 2.3: An image showing the production of secondary particles at different stages of the trajectory of the particle. GEANT4 manages them all by a stacking mechanism [3].

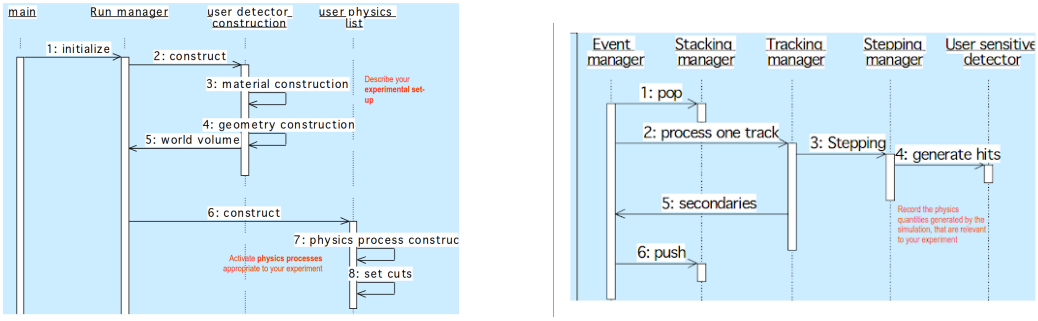

(a) (b)

Figure 2.4: Schematic diagram of the workflow in GEANT4: (a) initialization of a simulation program, (b) workflow of tracing the particles in an event

- **Track:** In GEANT4, a particle at any instance is referred as a 'track'. It is managed by G4Track class. An object of this class has physical quantities of the particle at the current instance only. It does not contain any record of the previous instance. As an example any physical information such as position, kinetic energy, current volume etc. about the primary photon or an electron can be accessed using the methods in a track object.

- **Step:** A 'step' contains the "delta" information of a particle while being traced in the simulation. The energy deposition between two points, time of flight etc. of a particle can be accessed using the step information. Here it should be noted that a **track** is not a collection of the **steps**. Instead, a track gets updated by a step. A step in GEANT4 is composed of two 'step points':

  1. **Pre-step point:** It contains the information about the track at an instance just before.
  2. **Post-step point:** It contains the information about the track at the current instance.

  Information from a pre-step point and a post-step point can be used to get some key information about any particle. For example, in Compton scattering of a photon, the scattering angle can be determined by calculating the angle between the photon momentum directions at pre- and post-step points (see Fig. 2.5a). Information from the step can also be used to tell whether a particle crossed the boundary between two volumes (see Fig. 2.5b). The volumes containing the pre- and post-step points

can also be accessed to check whether a particle crossed the boundary between the volumes from a specific direction.

- **Process:** In GEANT4, there is a list of applicable processes which a particle can undergo while traversing a material. At each step, all physics processes involved proposes their physical interaction lengths. Among these processes a step is decided by the process which has the smallest value of the interaction length. In GEANT4, particle **'transportation'** by which a particle interacts with geometrical **volume boundaries** and fields of any kind, is also considered as a process.

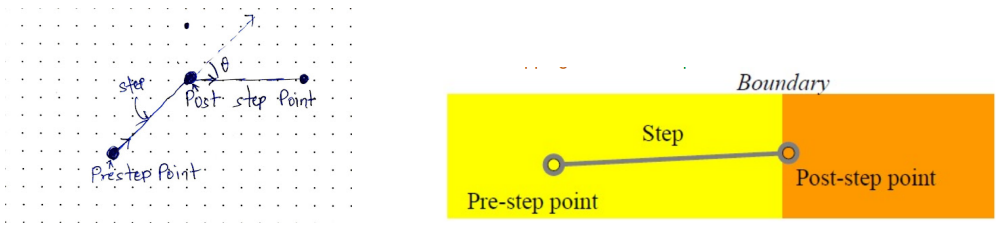

(a) (b)

Figure 2.5: Use cases of step points in GEANT4 simulation: (a) calculating scattering angle from the photon momenta at pre- and post-step points, (b) determining if a particle is crossing the boundary between the two volumes

2.2 Some key aspects of creating a simulation program in GEANT4

There are multiple aspects of defining a simulation program in GEANT4. In this section, we will give an overview of some important aspects used in the work presented in this thesis.

Defining the geometry

Any detector geometry is composed of a number of volumes. The largest volume, in which all the others volumes reside is called 'World Volume'. A user needs to define three types of "volumes" to create any volume in the geometry: (1) **solid volume**, which represents the physical dimensions of a volume, (2) **logical volume**, which contains the information about the material of the volume, sensitive detector behaviour and some other attributes like color, opacity etc in the visualization and (3) **physical volume**, which contains information about

the position and rotations of a logical volume in the geometry. It also contains the hierarchy of different detector volumes that if a volume is contained inside any other volume.

Generating primary particles

GEANT4 provides a set of particles which can be used in the simulation. A particle can be identified from its characterizing properties such as mass, charge, spin, decays, etc. In GEANT4, each particle is represented by its own class derived from G4ParticleDefinition, which contains values of all its characterizing properties. GEANT4 gives flexibility to a user to define a custom particle also by providing the values of the characterizing properties of the particle.

In GEANT4 simulation, generation of primary particles is handled by 'PrimaryGeneratorAction' class. A 'G4ParticleGun' object is defined there to use it as an actual primary particle generator. A user provides the values of different attributes required (e.g. momentum, point of origin, polarization etc.) to generate a primary particle. These attributes can have a value, which is fixed over all the events or can be sampled using GEANT4's random value generator or can be read from an external ROOT tree generated from any event generator like Pythia [32] and MadGraph [33] etc.

Defining the physics process and cuts

In GEANT4 there are different modules of physics processes, known as 'physics list' to handle the interaction of particles with the material. In GEANT4, there are seven major categories of physics processes : electromagnetic, hadronic, transportation, decay, optical, photolepton-hadron, and parameterisation [34]. A user can can make a choice on what modules to include in the program among the above seven modules. GEANT4 enables a user to choose the cross section of a process from different physics models also. For example, cross section for photoelectric effect can be chosen from Penelope model [35] or Livermore model [36].

To save the computational resources, a user can define some threshold for production of secondary particles also known as production cuts. These production cuts are particle specific i.e. can have different values for different particles.

Extracting the useful information from the detectors

1. **Hit:** A 'hit' is a snapshot of the physical interaction of a track in a sensitive detector. In a hit object, user can store information associated with a G4Step object (e.g. position, time, energy etc). GEANT4 provides a 'G4VHit' abstract class based on which a user writes a customized class for hit. Methods for filling the information and accessing those filled information are defined in the custom hit class, which enables the user to decide which information of the interaction to store in a hit object.

2. **Sensitive detector:** The main purpose of a sensitive detector is to construct the 'hit' objects when a track comes into its physical volume. User can write a custom class for sensitive detectors to process the hits produced. The 'ProcessHits()' method of 'G4VSensitiveDetector' class performs this task using the 'G4Step' objects as an input. 'G4VSensitiveDetector' is an abstract base class which represents a sensitive detector. Conditions to register a hit are defined in that custom class and information in the hits are filled. All hits of an event can be stored in an vector, which can be accessed further in an event by the user.

Visualization and parallelization

GEANT4 enables the user to graphically visualize the simulation program by visualizing the detector components, particle trajectories etc. The visualization in GEANT4 supports a diverse family of graphical systems such as QpenGL and Qt.

To save the time to run a simulation program, GEANT4 enables a user to take the advantage of parallelism by the means of 'mutithreading'. A user can run the simulation in the multiple CPU threads available in the machine. The events in a run can be distributed among all these threads, which make the whole simulation program to run significantly faster compared to running the program in a single CPU thread.

Chapter 3

Energy resolution and efficiency of scintillation detectors

Energy resolution and efficiency of a particle detector plays a crucial rote in characterizing its performance. These two parameters critically determines the suitability of a detector material and dimension for a given experimental application. A comprehensive study of these characteristics is essential for optimizing the detector design as well as accurate interpretation of the measured data.

3.1 Particle interactions with matter and their simulation

To measure the energy of the incoming particle in the detector, we need to understand the processes by which a particle (specifically photons in our case) interacts with the detector material. Photons can deposit their energy mainly via the following three processes:

1. **Photoelectric absorption:** This process involves a complete absorption of a photon by an atom of a material with the subsequent ejection of the bound electron from the atom with nucleus absorbing the recoil momentum. Dependence of photoelectric absorption cross section on incident photon energy (E_γ) and atomic number (Z) is popularly approximated as:

$$\boxed{\sigma_{photo} = constant \times \frac{Z^n}{E_\gamma^{3.5}}} \tag{1}$$

   Here n can vary between 4 and 5 depending on the energy of the incident photon.

This strong dependence of photoelectric absorption probability on Z indicates that higher Z (atomic number) materials are most favored for photoelectric absorption.

2. **Compton scattering:** This process refers to scattering of photons by free electrons of atoms in the material. The electrons in the material are bound to the atom but if the photons energy is high with respect to the binding energy of an electron, then electrons can be treated as essentially free. The cross section of Compton scattering in a material goes as

$$\boxed{\sigma_{compton} = constant \times Z\frac{lnE_\gamma}{E_\gamma}} \tag{2}$$

Compton scattering can be used as a tool to experimentally measure the polarization of photons, which is discussed in Chapter 4.

3. **Pair production of electron and positron:** If energy of an incident photon exceeds twice of the rest mass energy of an electron ($1.022\ MeV$), the photon can produce a pair of electron and positron. In our case the photons coming from the decay of para-positronium (at rest) will carry 511 keV energy at the most. Therefore pair production process is not relevant for studies presented in this thesis.

Fig. 3.1 shows the comparison of cross section of Compton scattering and photoelectric effect as a function of incident photon energies for lead (left) and carbon (right). It shows that for E_γ=511 keV Compton and photoelectric cross section are similar for high Z materials while Compton cross section dominates for low Z materials.

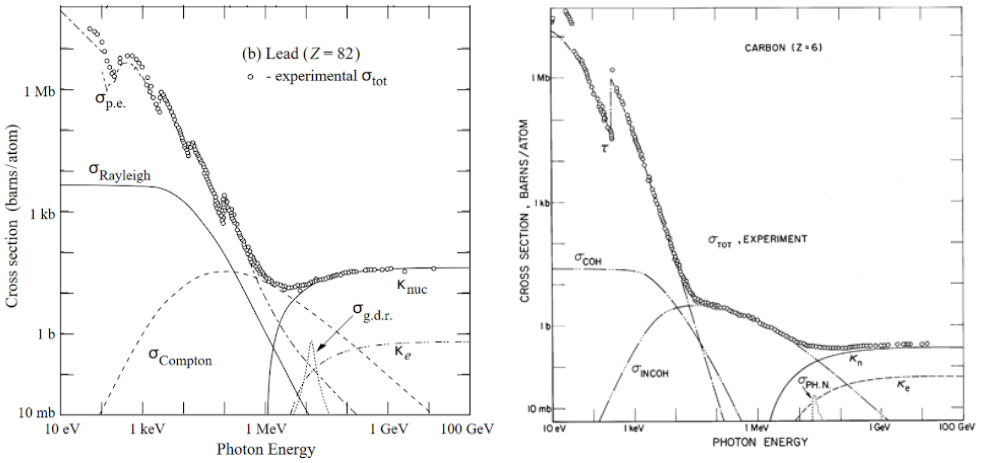

(a) (b)

Figure 3.1: Comparing the cross section for Compton scattering and photoelectric absorption of the photons as a function of incident energy: (a) in a high Z material [4], (b) in a low Z material [5].

Scintillators

Scintillation detectors are commonly employed in nuclear and particle physics experiments as particle detection devices. These materials emit photons, called **scintillation photons**, when radiation or particles loose energy interacting with them. These scintillation photons are also referred as optical photons in the thesis. Energy deposited by the interacting radiation in the scintillators excites molecules of the material. These molecules de-excite to the ground states by emitting photons [7]. These scintillation photons can be converted into an electrical pulse by coupling them to an amplifying device such as a photomultiplier tube (see Fig 3.2). These electrical pulses can be further analyzed to get various information about the incident radiation.

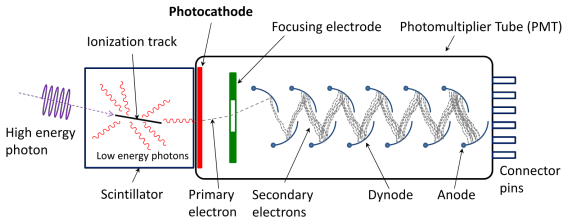

Figure 3.2: An schematic diagram of a scintillation detector coupled to a photomultiplier tube (PMT). [6]

3.2 Modeling of scintillation in GEANT4 simulation

GEANT4 does not simulate molecular excitation and de-excitations to produce the scintillation photons. Instead, it statistically models the number of optical photons produced using scintillation parameters of the material provided by the user [37]. Number of scintillation photons produced, the energy spectrum of the scintillation photons and the distribution of emission times are the characterizing properties of any scintillator material.

3.2.1 Number of scintillation photons

Number of scintillation photon produced per MeV of energy deposit (termed as **Scintillation Yield**) for a given material is experimentally measured and is provided to the GEANT4 by the user. However, the production of scintillation photons is a stochastic process and there is a variation in the scintillation yield for a given value of incident energy of a particle. In GEANT4, this event-by-event scintillation yield is sampled from a distribution with a mean close to the scintillation yield provided by the user [37]. In GEANT4, the number of optical photons to be produced at every step is calculated as follows:

- The mean number of optical photons to be produced in a step is calculated as product of the **Scintillation Yield**, yield factor defined as the ratio of fast component yield to the total yield, and total energy deposit.
- If the calculated mean is less than or equal to 10, the actual number of scintillation photons is sampled from a Poisson distribution with that mean, then converted to an integer.
- The number of scintillation photons is sampled from a Gaussian distribution with calculated mean, if the computed mean is larger than 10. The standard deviation of that Gaussian distribution is computed as the square root of the calculated mean times a user supplied factor known as the **'Resolution Scale'** [38].

3.2.2 Time evolution of scintillation photons

In a scintillator material, after a molecule is excited, the de excitation process can occur immediately after excitation (within $10^{-8}\ ns$) termed as **fluorescence** or can occur after a long time (ranging from a few microseconds to hours depending on the material) termed as **phosphorescence** [7].

One can describe the time evolution of the re-emission process roughly as a simple exponential decay [7]. However, the time evolution of scintillation is more complex in some materials, which can be approximated by a two component exponential:

$$N = A\ \exp\left(\frac{-t}{\tau_f}\right) + B\ \exp\left(\frac{-t}{\tau_s}\right) \tag{3}$$

where, A and B are constants , τ_f and τ_s are the decay constants of the fast and slow components, respectively. User needs to provide the value of these decay constants and the scintillation yield of these fast and slow components to model the scintillation in GEANT4 simulation framework.

Distribution of time of scintillation photons produced by incident photons of 511 keV energy in a 5 cm thickness of the $PbWO_4$ tile is shown in Fig 3.3. Details of the detector geometry etc. is given in Section 3.4. The distribution presented here corresponds to 10000 incident photons. To verify the model used for the time evolution of scintillation photons, we fitted the distribution with the two component exponential function as mentioned in the eq. Eq. (3) with time constants as the free parameters. After fitting we got back the fast and slow component of the decay approximately equal to the values which we provided, namely 1 ns and 10 ns, respectively.

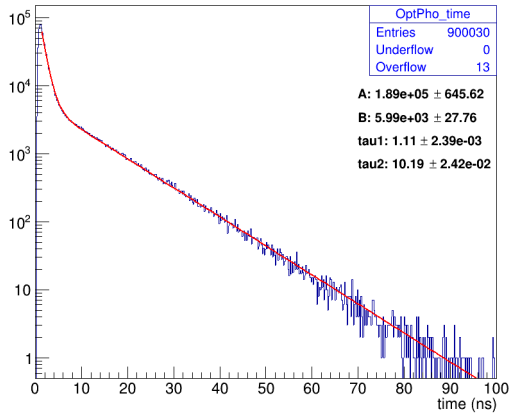

Figure 3.3: Time response of the scintillator in simulation

3.2.3 Energy of the scintillation photons (emission spectra)

Energies of all the scintillation photons emitted are not identical. To model this feature of the scintillation photons, the energy of an optical photon is sampled from a probability

distribution called emission spectrum. This emission spectra is a list of relative intensities, corresponding to different photon energies. In GEANT4, a user has to define the emission spectra for the fast and slow component of the scintillation. When scintillation photons are produced, their energies are sampled from this list randomly, with a higher chance of picking an energy with higher relative intensity.

3.3 Energy resolution and efficiency of a detector

Energy resolution of a detector

The energy resolution of detector is a measure of its capability to distinguish between two closely spaced energies of the incoming particles (see Fig. 3.4). A possible way to measure the energy resolution of a detector is to send a beam of radiation with fixed energy into the detector and observe the distribution of measured energy. Instead of a delta function at the incident energy, the distribution of measured energies has a finite width. It is usually Gaussian in shape peaking at the incident energy. This width arises because of stochastic nature of the process involved in dissipation of energy by the particles. It results in variation in the recorded signals e.g. fluctuation in number of scintillation photons produces, fluctuations in the secondary electron production in the PMTs etc.

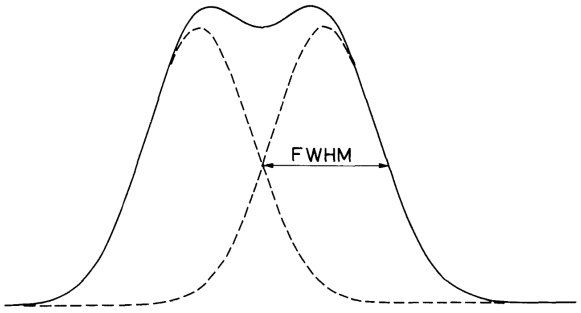

Figure 3.4: An image the showing the meaning of resolution: two closely spaced incident energy are distinguished by a detector only if there distance is larger than the energy resolution of the detector [7].

Usually resolution is given in terms of the full width at half maximum of the peak (FWHM). In high energy physics, it is common to use the standard deviation ((σ)) instead

of FWHM for the purpose. The relative resolution at energy E is given by the expression:

$$\text{Resolution} = \frac{\Delta E}{E} \tag{4}$$

where ΔE is the width of the gaussian with mean E.

In this thesis, we have defined this width in terms of the standard deviation (σ) of a gaussian function with mean μ. Thus, we have quantified the resolution of the detector as σ/μ. This is discussed in detail later in this chapter in Section 3.5.4.

As we see in Eq. (4), the resolution of a detector varies with the incident energy. Here the Poisson or Poisson like statistics of ionization and excitation plays a role. The number of ionization events rises with energy, which causes the relative fluctuations to decrease [7]. Using the expressions of mean and FWHM (in our case σ) of the Poisson distribution, we get the dependence of resolution on energy deposited as

$$E \propto \frac{1}{\sqrt{E}} \tag{5}$$

This illustrates that the relative energy resolution improves with the energy deposited, hence the incident energy of photons (or charged particles).

Efficiency of a detector

Depending on the detector material and its geometry, an incoming photon can deposit all of its energy in the detector or it can leave the detector with partial or no energy deposit. In our case, by efficiency we mean the fraction of events where incoming photons completely deposit their energy in the detector.

$$\text{Efficiency} = \frac{\text{number of events with full energy deposited by photons}}{\text{total number of events}} \tag{6}$$

3.4 Simulation setup

3.4.1 Detector geometry

For our studies presented in this thesis, we aim to create a 4π hermitic detector around a radioactive source. For the preliminary studies to understand the various ingredients of the

GEANT4 simulation framework, we added the elements shown in Fig. 3.5 for our detector geometry:

1. **World volume:** A cube of dimension $1\ m \times 1\ m \times 1\ m$ filled with air placed at (0,0,0).

2. **Photon source:** A photon gun placed at the center of the world volume (0,0,0), which shoots photons of certain predefined energy in $+z$ direction. See Fig. 3.5b for the choice of co-ordinate system.

3. **Detector tiles:** We make an cubical enclosure made from 6 trapezoidal scintillator tiles. We test a few scintillator materials using this geometrical setup and a few detector dimensions. The inner dimension of the enclosure is fixed $20\ cm \times 20\ cm \times 20\ cm$ and we vary the thickness of tiles between $1\ cm$ to $10\ cm$.

   For the studies presented in the following sections, out of the 6 detector tiles in the enclosure, we take energy deposits and optical photon produced in one tile only, where the primary photon is incident. We kill any particle (both primary and secondary particles) if it leaves the detector tile. Also, we are not tracing the optical photons through the detector volume for these studies, we kill an optical photon once it reaches the detector boundary.

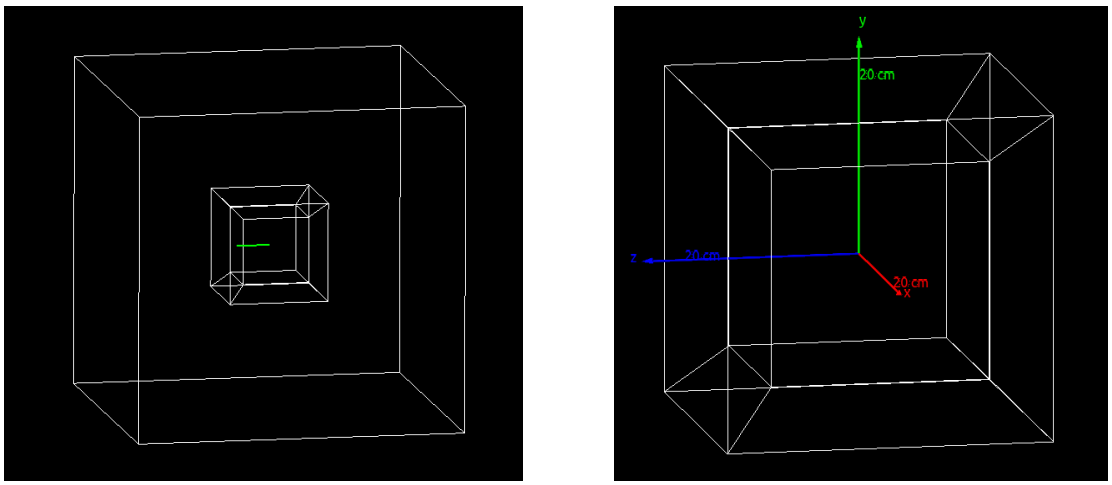

(a) (b)

Figure 3.5: Detector setup in simulation: (a) visualization of the primary photon incident on a detector tile, (b) coordinate axes used in simulation setup

Following give scintillator materials have been used in our studies presented here:

(a) Lead Tungstate ($PbWO_4$)

(b) Bismuth Germanate ($Bi_4Ge_3O_{12}$) termed as BGO

(c) Cerium doped Lutetium–yttrium oxyorthosilicate (general composition: $Lu_{2(1-x)}Y_{2x}SiO_5$, used: $Lu_9Y(SiO_5)_5$) termed as LYSO(Ce)

(d) Cerium doped Gadolinium Aluminum Gallium Garnet ($Gd_3Al_2Ga_3O_{12}$) termed as GAGG(Ce).

(e) Cerium doped Lanthanum Bromide ($LaBr_3$(Ce))

4. **Physics list:** For our studies in this chapter, we are using the two models of physics list relevant for our case: (1) 'G4EmStandardPhysics_option4' (handles the electromagnetic interactions in the lower energy levels) and (2) 'G4OpticalPhysics' (to handle the optical photons).

Fig. 3.6 illustrates the energy deposited by 511 keV photons inside a 5 cm thick $PbWO_4$ material via different processes for 10000 simulated events. Energy deposited via Compton scattering and photoelectric absorption is calculated as the difference of kinetic energies of a primary photon after and before the interaction happens. As visible in Fig. 3.6a, Compton edge is observed at the energy less than the incoming photon energy. It means that in Compton scattering, a photon does not transfer all of its energy to the free electron of the atom. Full energy deposit can happen only via photoelectric absorption (see Fig. 3.6b).

The total energy deposited shown in Fig. 3.6c is calculated as the sum of energy deposited by all the particles (both primary and secondary particles) in the event. There we see a sharp spike at the 511 keV, because energy deposited is calculated using the "truth" information extracted from the 'steps' in the simulation. As mentioned earlier in this chapter, total energy measured in the detector will have some fluctuations around 511 keV. In simulation, we determine the energy deposited in a realistic way by analyzing the distribution of number of scintillation (optical) photons produced in the detector.

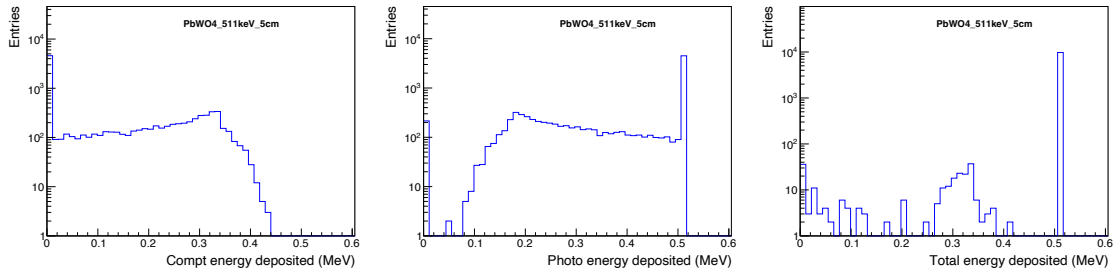

(a) (b) (c)

Figure 3.6: Energy deposited by 511 keV photons in 5 cm thick $PbWO_4$ material: (a) energy deposited by Compton scattering, (b) by photoelectric absorption, (c) total energy deposited.

Fig. 3.7 compares the energy deposited by 511 keV photons in three different thickness of $PbWO_4$:(1) 2.5 cm, (2) 5 cm, (3) 10 cm. It shows that 2.5 cm thickness of $PbWO_4$ material is sufficient to stop the 511 keV photons.

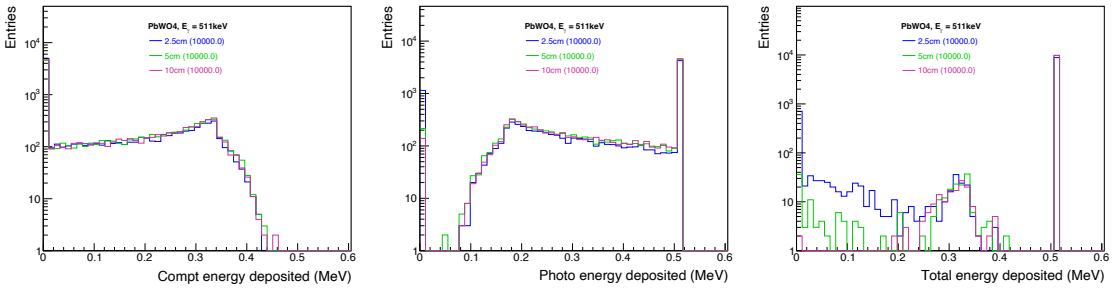

(a) (b) (c)

Figure 3.7: Comparing the energy deposited by 511 keV photon in three thicknesses of $PbWO_4$: 5cm, 2.5cm, 10cm: (a) via Compton scattering, (b) via photo-electric absorption, (c) total energy deposited

Fig. 3.8 compares the energy deposited in 5 cm thick $PbWO_4$ by the photons having different incident energies. We see that for higher values of incident photon energies, there are more events in the partial energy deposits because photoelectric cross section decreases with higher values of incident photon energies.

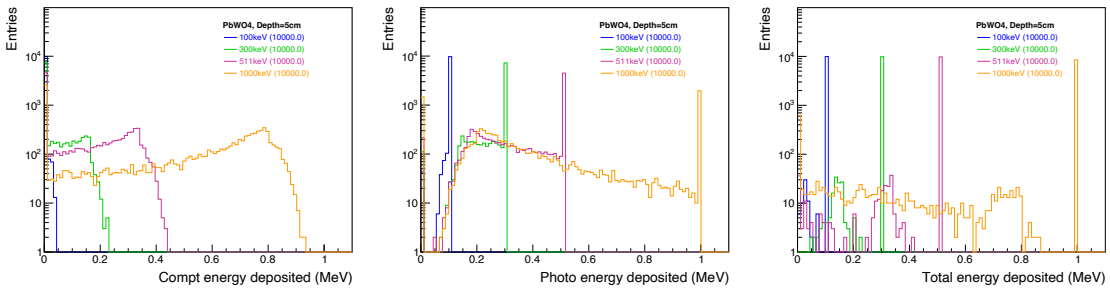

Figure 3.8: Comparing the energy deposited in 5 cm thick $PbWO_4$ by 100keV, 300keV, 511keV, 100keV photons: (a) via Compton scattering, (b) via photo-electric absorption, (c) total energy deposited

Fig. 3.9 compares the energy deposited by 511 keV photons in 5 cm thickness of the different materials. Since $PbWO_4$ has the highest Z among all them, it has the most event fraction with complete energy deposits. To see the energy deposited by different energies of incident photons in other materials also refer to Appendix Section A.1 & Appendix Section A.2.

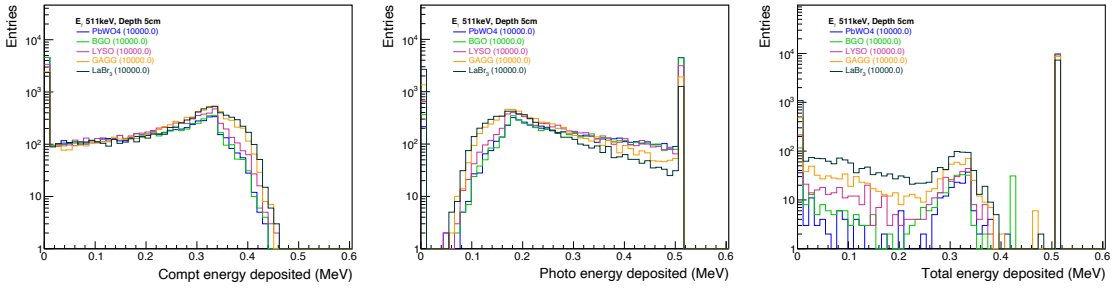

(a) (b) (c)

Figure 3.9: Comparing the energy deposited by 511 keV photons in 5cm thicknesses of $PbWO_4$, BGO, LYSO, GAGG, $LaBr_3$: (a) via Compton scattering, (b) via photo-electric absorption, (c) total energy deposited

3.4.2 User defined scintillation parameters for different materials

Scintillation parameters

The scintillation parameters used in the simulation are tabulated in the Section 3.4.2 for the five materials described in Section 3.4. Fig. 3.10 shows the emission spectrum for these materials. In simulation, we provide the discrete values of relative intensity for different

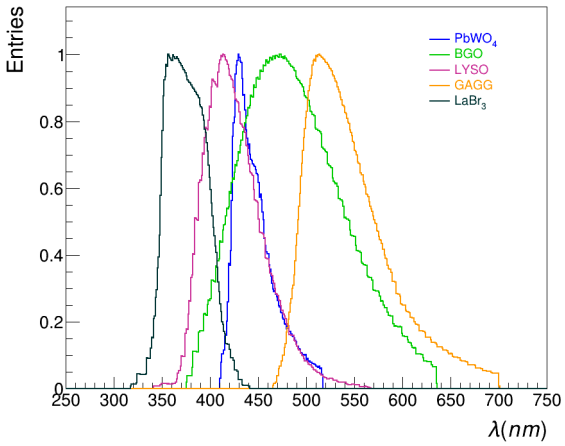

Figure 3.10: Emission spectra of different materials got from simulation

wavelengths. GEANT4 interpolates the value of relative intensity between any two wavelengths.

Parameter	**Material**				
	PbWO4	**BGO**	**LYSO**	**GAGG**	**LaBr3**
Density (g/cm^3)	8.28	7.13	7.1	6.63	5.29
SY (pho/MeV)	200	8200	30000	28244	61000
Rise time	10 ps	30 ps	70 ps	8 ns	5.7 ns
SY1	0.8	0.1	1	0.392	0.9
τ_1 **(ns)**	5	60	40	50.1	30
SY2	0.2	0.9	0	0.608	0.1
τ_2 **(ns)**	30	300	—	321.5	300
Peak emission λ**(nm)**	420 & 520	480	410	380 (weak) & 520	380
Birks Constant	0 (assuming)				

Table 3.1: Table summarizing the scintillation parameters for different scintillator materials

Birks constant introduces some non linearity in the scintillator response. We have specified the Birks constant to be 0 for all the materials for these preliminary studies (to avoid additional complexity).

We have not defined the absorption length and the boundary interaction because for our studies we are only interested in the number of scintillation photon produced for different values of incident photon energy in a given material.

3.5 Analyzing distributions of the number of optical photons

Instead of getting the energy deposits at the truth level, here we determine the value of energy deposited in the detector by analyzing the distribution of number of optical or scintillation photons produced in the detector. By analyzing the optical photon yields, we also determine the energy resolution and efficiencies of different detector materials and with different thicknesses.

The Fig. 3.11 shows the distribution of number of optical photons produced in 2.5 cm thickness of GAGG from the energy deposited by the incident photons of energy 511 keV. The events lying in the tail of the distribution (before the gaussian peak) corresponds to the events where incoming photon deposits some of its energy via Compton scattering and leaves the detector. The events under the gaussian like peak corresponds to the events where incoming photon completely deposits its energy in the material by photoelectric effect after undergoing some Compton scatterings. In the work presented here, we have determined the resolution and response of the detector, using the information got from the fitted gaussian and also have defined the efficiency to be the fraction of events coming under the gaussian. These are discussed in details in the following sections.

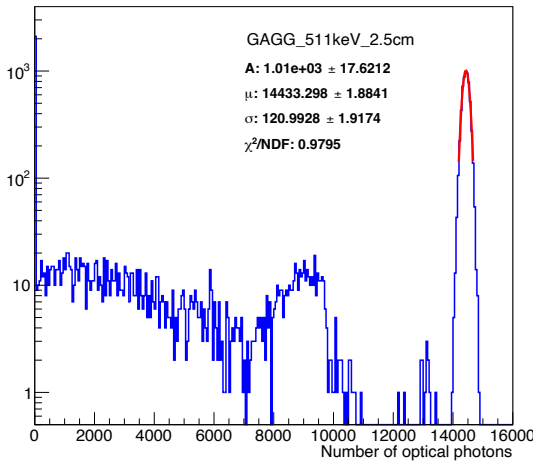

Figure 3.11: Full range distribution of number of optical photon produced in 2.5 cm thickness of GAGG

In GEANT4, we varied the energy of photon gun between 100 keV to 1000 keV and simulated 10000 events (shooting 10000 photons). We recorded the number of optical photons generated for each event. Fig. 3.12a compares the distribution of optical photon yields produced in 5 cm of $PbWO_4$ by the incident photons of different energies. These results are further used to establish the linearity of the detector as explained in the next section.

Fig. 3.12b compares the distribution of number of optical photons produced in 3 different thickness of $PbWO_4$ (2.5 cm, 5 cm and 10 cm) produced by energy 511 keV photons. There we observe that height of the peak decreases slightly with decreasing the material thickness, because in less thickness less number of incoming photons fully deposit their energy in the material. To compare the distribution with varying material thickness and incident photon energies in the materials see the plots in Appendix Section A.6.

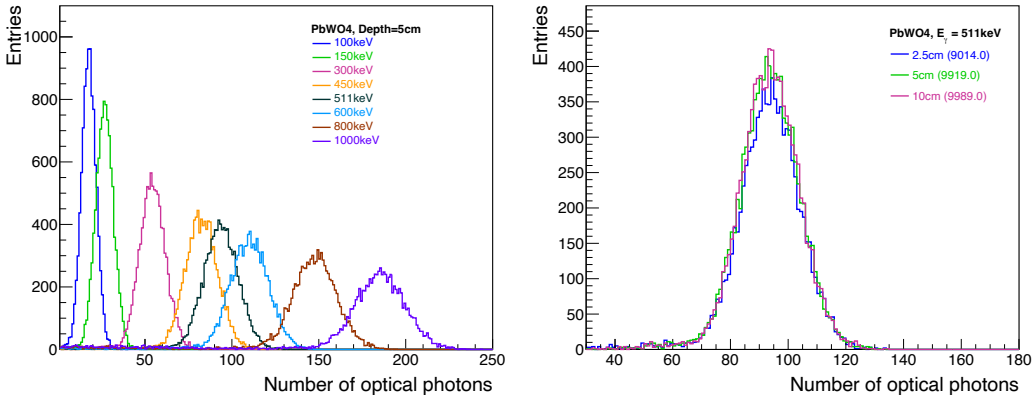

(a) (b)

Figure 3.12: ((a) Distribution of number of optical photons produced in 5 cm thick $PbWO_4$ at different incident photon energies: 100 keV, 150 keV, 300 keV, 450 keV, 511 keV, 600 keV, 800 keV, 1MeV. (b) Distribution of number of optical photons produced by 511 keV photons in 3 different thickness of $PbWO_4$: 2.5cm, 5cm, 10cm

3.5.1 Mean and standard deviation of scintillation photon yield

For the total energy deposit, we only have to consider the events in which photon is fully absorbed in the detector, that is those with total energy deposited under the photo peak. We iteratively fit the distribution of number of optical photons with a Gaussian function in the range from -2 std. dev. to $+2$std. dev. around the photo peak. Then we take the mean (μ) and standard deviation (σ) of the fitted Gaussian function as the average photon yield and its spread. Fig. 3.13 shows the iterative fits of some incident photon energies for 5 cm thick $PbWO_4$ material. For iterative fits of other photon energies in different thicknesses of the materials refer to Appendix Section A.5.

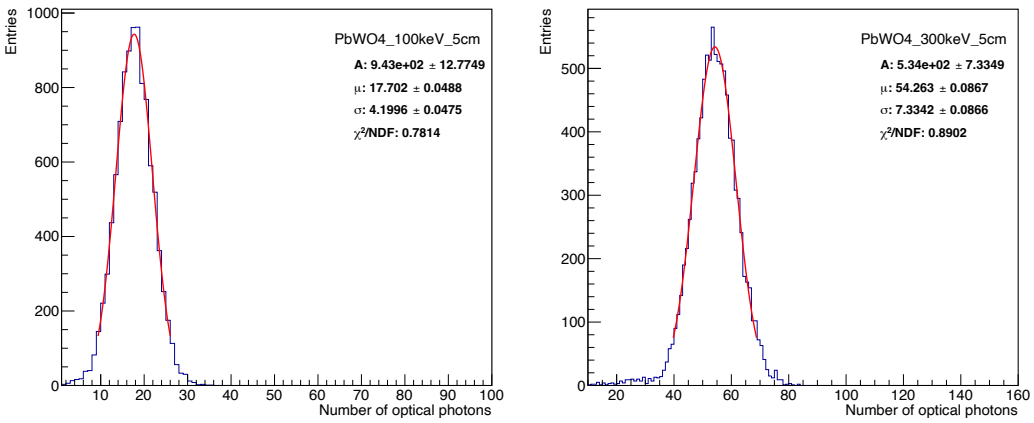

(a)

(b)

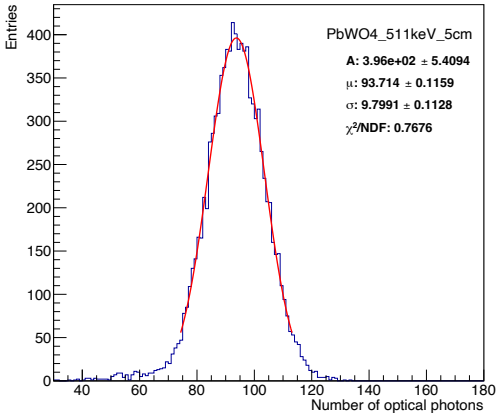

(c)

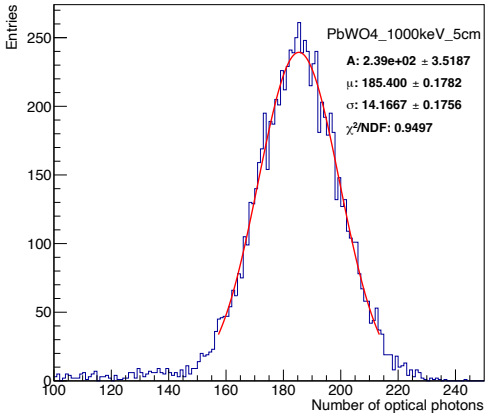

(d)

Figure 3.13: Iterative fitting of number of optical photons with a Gaussian function around the photo peak for E_γ: (a) 100 keV, (b) 300 keV, (c) 511 keV, (d) 1000 keV

Table 3.2 summarizes the fitted mean and standard deviation for 100 keV, 150 keV, 300 keV, 450 keV, 511 keV, 600 keV, 800 keV photons for 5 cm thickness of $PbWO_4$ material.

E_{inc} (keV)	mean number of optical photons produced (N_γ)	$\sigma_{N\gamma}$
511	91.714	9.73
100	15.357	4.78
150	24.38	5.26
300	52.396	7.04
450	80.36	9.19
600	108.32	10.73
800	145.74	12.64
1000	183.37	13.90

Table 3.2: Table for fitted mean and standard deviation at different Energies

3.5.2 Calibrating scintillation photon yield to measure the incident photon energy

We take the mean of scintillations produced at 511 keV (91.714) as a calibration point and get a measured value of energy for other value of incident energies. In simulation, we have calculated the measured value of energy $E_{Measured}$ using the relation:

$$\boxed{E_{Measured} = \frac{511 \text{ keV}}{91.714} \times N\gamma} \tag{7}$$

where $N\gamma$ is the mean of number of scintillation photons generated from incident photons of energy $E_{Incident}$. Fig. 3.14 shows the distribution of $E_{Measured}$ in 5 cm thickness of $PbWO_4$ and GAGG by 511 keV photons. There in the distribution of $E_{Measured}$, we observe that the width of gaussian peak is more in $PbWO_4$ as compared to GAGG, because scintillation yield of GAGG is much higher than that of $PbWO_4$ (see Section 3.4.2). To see the comparison of distribution of $E_{Measured}$ in different material thicknesses and for different incident photon energies, refer to Appendix Section A.4.

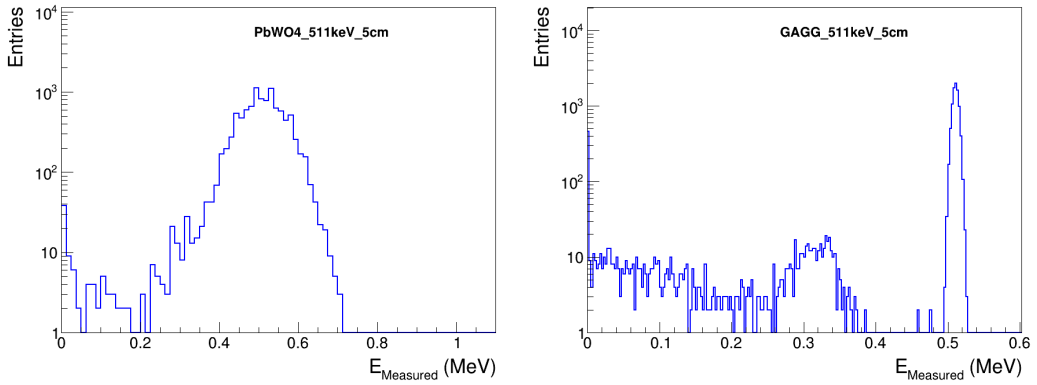

(a) (b)

Figure 3.14: Distribution of measured value of energy deposited in 5 cm thick material: (a) in $PbWO_4$, (b) in GAGG

3.5.3 Light output Response of the Scintillator

Light output of a scintillator describes how well it converts energy deposited into the optical photons. It is also desirable from the scintillators that the light output varies linearly with the incident energy so that the measured optical photon yield can be use to extract incident energy of the particles. As shown in Fig. 3.15a, we get a linear relationship between the mean number of optical photons produced and the incident photon energy. We would like to remind here that we have specified the Birk's constant [7] for the detector material to be zero. In reality Birk's constant is non zero and it may introduce some non-linearity in the detector response. Also, the y-intercept of the curve is negative which is not possible in the realistic situation. Fig. 3.15c shows the response of the detector, which shows that at higher values of incident photon energies $E_{Measured}$ gets closer to the actual value of energy of the incident photons. To see the variation of number of optical photons, $E_{Measured}$, detector response with the incident photons in the different thicknesses of the different materials, see Appendix Section A.7.

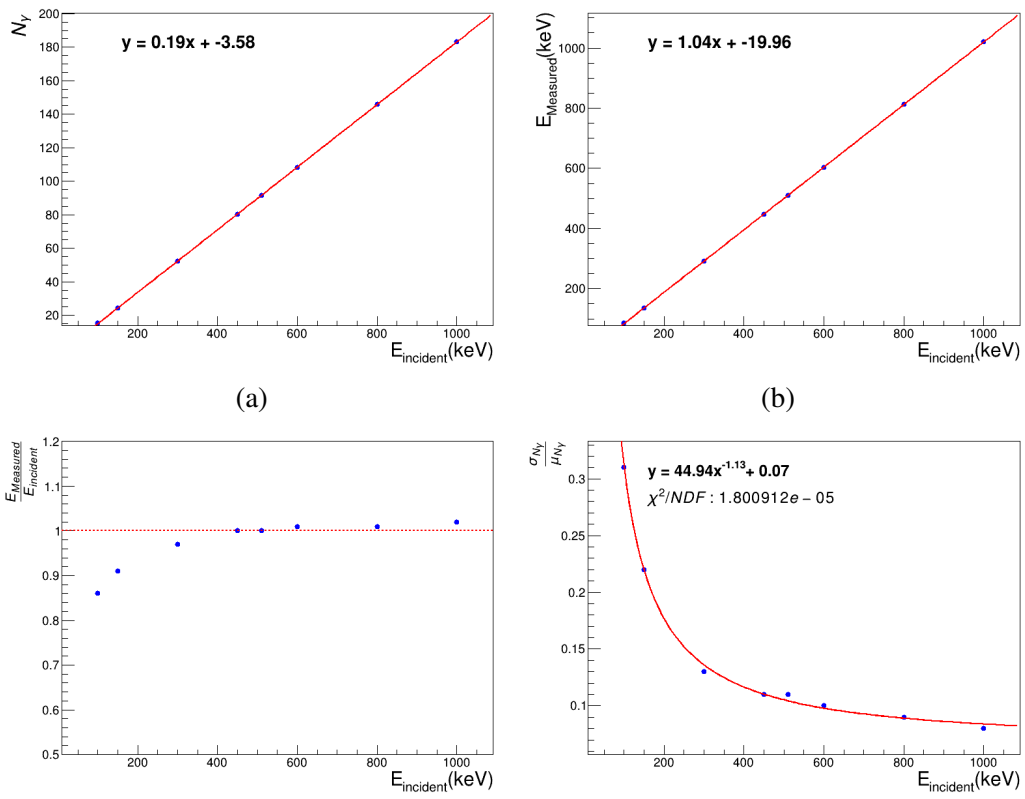

Figure 3.15: Results from the iterative fitting and calibration in 5 cm of $PbWO_4$: (a) mean value of number of optical photons produced as function of incident photon energies. (b) comparison between the measured and truth value with increasing incident photon energy. (c), (d) response and resolution as a function of incident photon energies

3.5.4 Determining energy resolution of the detector from the number of optical photon distribution

As mentioned in the previous Section 3.5.3, The number of optical photons produced is proportional to energy deposited in the material, therefore we can infer the energy resolution of the detector from the distribution of number of optical photons. We define the resolution of a material to be the ratio of mean of the fitted Gaussian function to the standard deviation of the same. Hence the expression of energy resolution is given as

$$\text{Resolution} = \frac{\sigma_{N\gamma}}{\mu_{N\gamma}} \tag{8}$$

Fig. 3.15d, shows the variation in resolution of 5 cm $PbWO_4$ with increasing the inci-

dent photon energy. The resolution improves with increasing incident energy. Because as the incident photon energy increases, more number of optical photons get produced, which results in the decrement of the relative fluctuations around the mean, as expected from Poisson statistics. Fig. 3.16a shows the effect of material thickness in the energy resolution of $PbWO_4$. The energy resolution does not change significantly with changing the material thickness. Because changing the material thickness does not affect the mean and variance (σ^2) of the distribution of number of optical photons for the cases in which incident photons are fully absorbed. To see the effect of material thickness in energy resolution for other materials also, please refer to Appendix Section A.8.

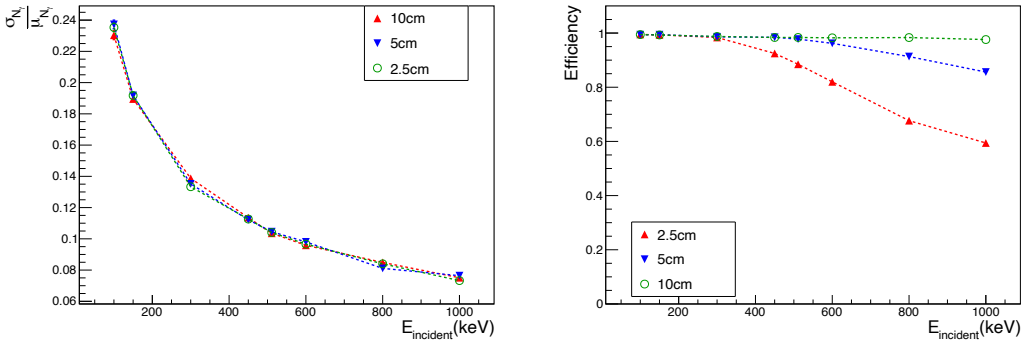

(a) (b)

Figure 3.16: Comparing the energy resolution (left plot) and efficiency (right plot) of $PbWO_4$ in three different thicknesses: 2.5 cm, 5 cm and 10 cm.

3.5.5 Determining the efficiency of the detector

In this thesis, we define the detector efficiency as the fraction of events in which photons are fully absorbed in the material. From the distribution of scintillator photon yield, this is defined as the ratio of integral of the distribution from -3σ to 3σ around the mean to the integral of the whole distribution.

We can see in Fig. 3.16b, efficiency of the material decreases, with increasing the incident photon energy. Because photon with higher energy are less likely to deposit their full energy in a given thickness of the material. Also it is visible from the same figure that this decrease in efficiency is more rapid as we decrease the material thickness. To see the variation in efficiency in other materials also, please refer to Appendix Section A.8.

3.6 Energy resolution and efficiency in different materials and in different transverse sizes

3.6.1 Comparison of energy resolution and efficiency in different materials

Fig. 3.17 shows the comparison of energy resolution and efficiency in different materials. As we can see in the figure, energy resolution is worst for $PbWO_4$ out of the materials we have chosen. Because scintillation yield of the $PbWO_4$ material is very less compared to the other materials (see Section 3.4.2). But the efficiency of $PbWO_4$ is best among the materials, because of its higher material density (see Section 3.4.2) incident photons deposits it full energy in the material. Therefore, $PbWO_4$ can be chosen as a detector material for detecting the very high energy particles. To see the explicit values of energy resolution and efficiencies in the different thicknesses of different materials, please refer to the tables in Appendix Section A.9.

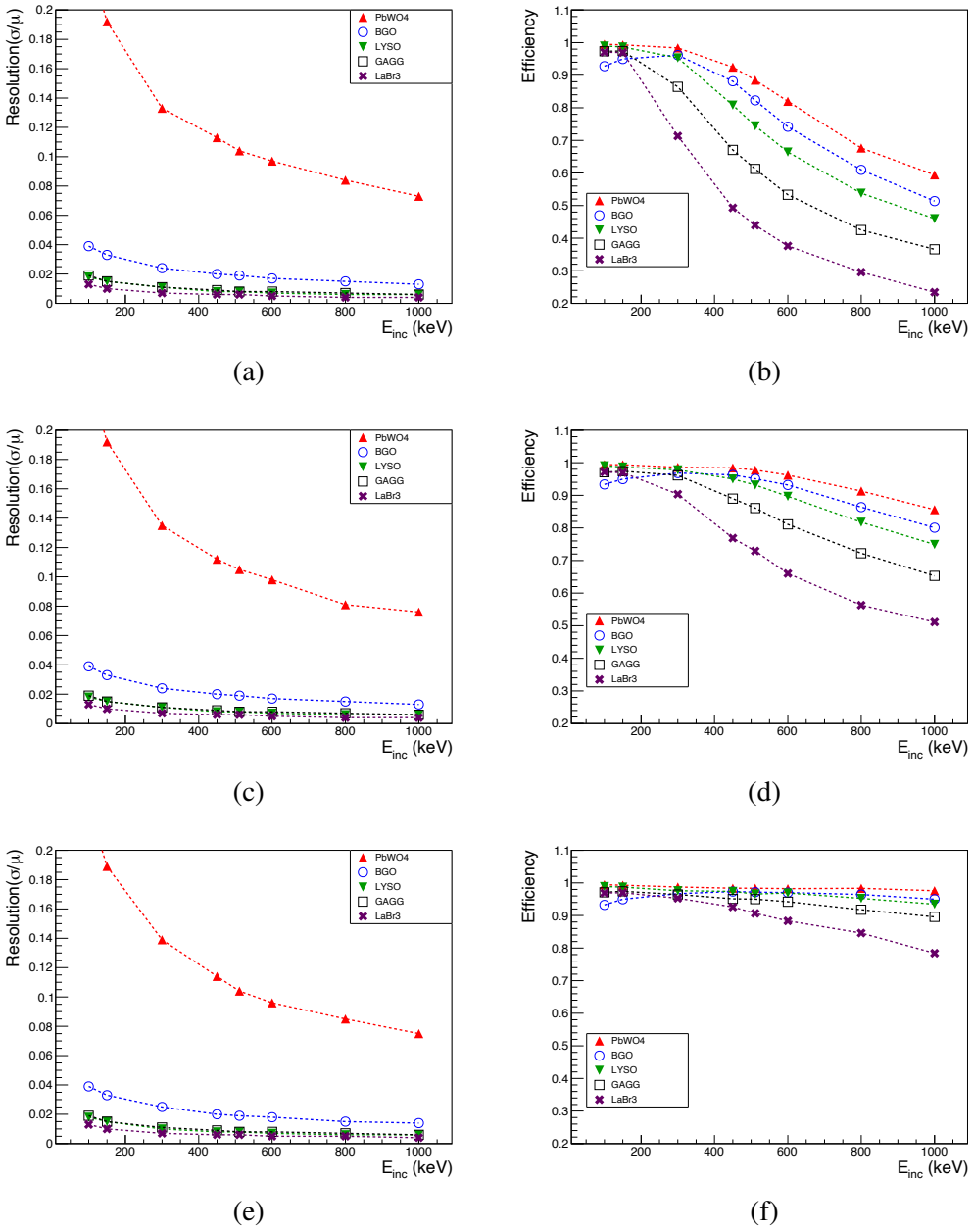

Figure 3.17: Comparisons of the energy resolution (left column) and efficiency (right column) of different materials ($PbWO_4$, BGO, LYSO, GAGG, $LaBr_3$). Comparison is shown for 3 different material thicknesses: 2.5 cm (upper row), 5 cm (middle row), 10 cm (bottom row)

3.6.2 Effect of the transverse size of the material in energy resolution and efficiency

To study the effect of transverse size of the material on the energy resolution and the efficiency, we compare results for tiles of two different transverse sizes: (a) $2.5\ cm \times 2.5\ cm$ and $20\ cm \times 20\ cm$. In Fig. 3.18, we have shown the results for $LaBr_3$ where the effect is most visible. There we observe that resolution is almost unchanged (as expected from the definition) while the efficiency of the material decreases, decreasing the transverse size of the material. To see the effect in different material for different thicknesses, refer to Appendix Section A.10.

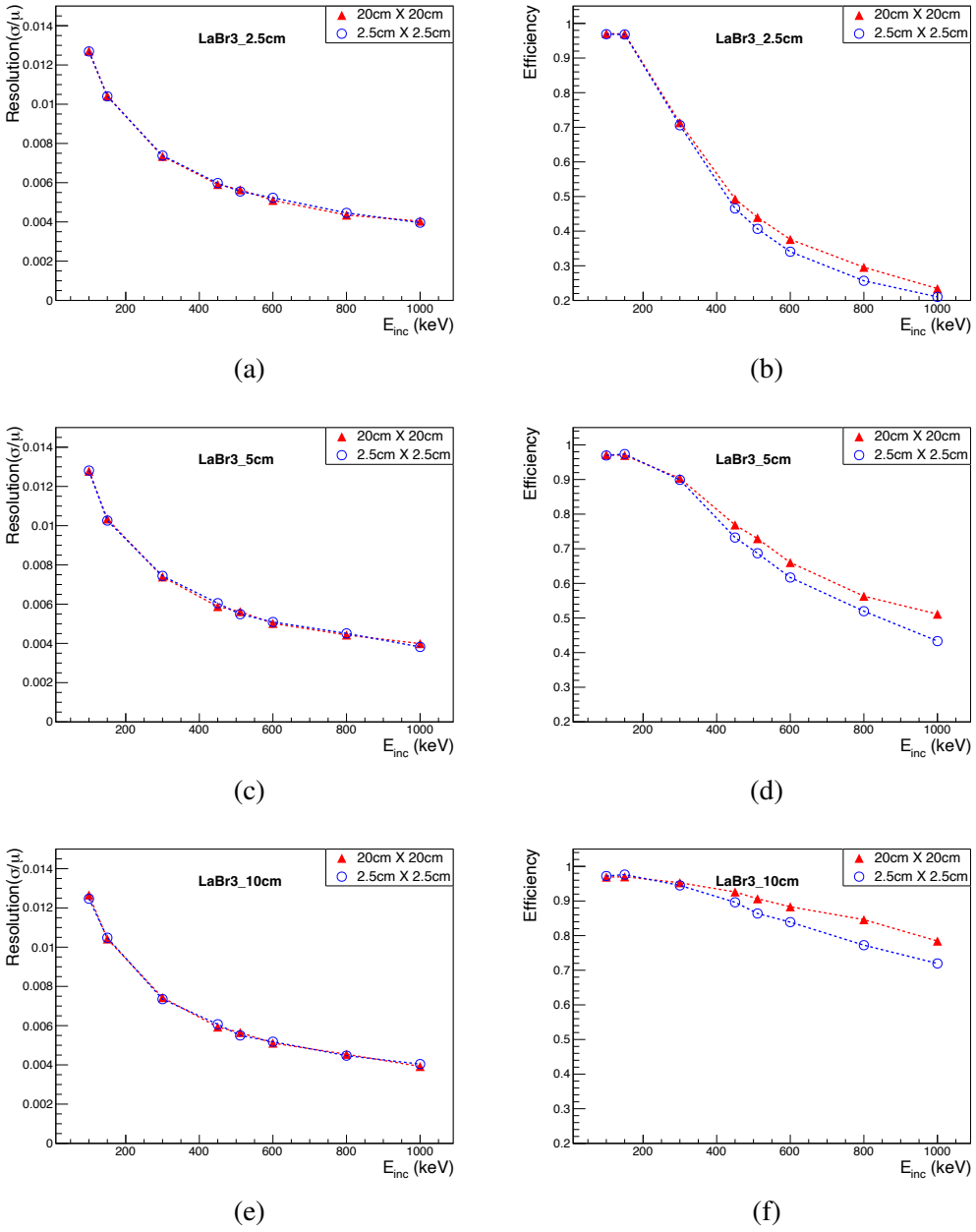

Figure 3.18: Comparing the energy resolution (left column) and efficiency (right column) of $LaBr_3$ in two different transverse sizes of the material ($2.5\ cm \times 2.5\ cm$ and $20\ cm \times 20\ cm$). Comparison is shown for 3 different material thicknesses: 2.5 cm (upper row), 5 cm (middle row), 10 cm (bottom row)

Summary

In this chapter, we presented studies of the two major processes via which a sub MeV range deposits its energy in the material: (1) Compton scattering, (2) photoelectric absorption. We also saw how the probability of these processes and the total energy deposited by a photon in the material depend on the different factors. Following this, we presented our studies on experimental measurements of the energy deposited by photons in material by analyzing the distribution of number of scintillation photons produced in a material. We used these distributions to make a comparative study of energy resolution and efficiency of photons of different incident energies and in the detectors of different material as well as sizes.

Chapter 4

Studying photon polarization in GEANT4 simulation

4.1 Photon polarization

Polarization is a fundamental physics property associated with photons and other particles with a nonzero spin. In the electromagnetic wave description of light, the electric and magnetic field vectors oscillate perpendicular to the direction of propagation. The polarization specifies the orientation of the oscillating electric field vector in space. In its particle description i.e. photon as a quanta of the EM field, polarization refers to the orientation of its intrinsic angular momentum or spin. The most general expression of a homogeneous plane wave propagating in the direction of **k** can be written as:

$$\mathbf{E}(\mathbf{x}, t) = (\hat{\epsilon}_1 E_1 + \hat{\epsilon}_2 E_2) e^{i\mathbf{k}\cdot\mathbf{x} - i\omega t} \tag{1}$$

where $\hat{\epsilon}_1$ and $\hat{\epsilon}_2$ represents the two orthogonal directions (for example x and y axis). The amplitudes of the orthogonal components, E_1 & E_2, of the electric field are complex numbers and can accommodate the phase difference between them.

Types of polarization

Depending on the magnitude and the phase difference between E_1 and E_2 of a planar EM wave, we can classify the polarized light into three types:

1. **Linear polarization:** The E_1 and E_2 with the same phase represents a linearly polarized wave. The resultant electric field of light is confined to a single direction in a

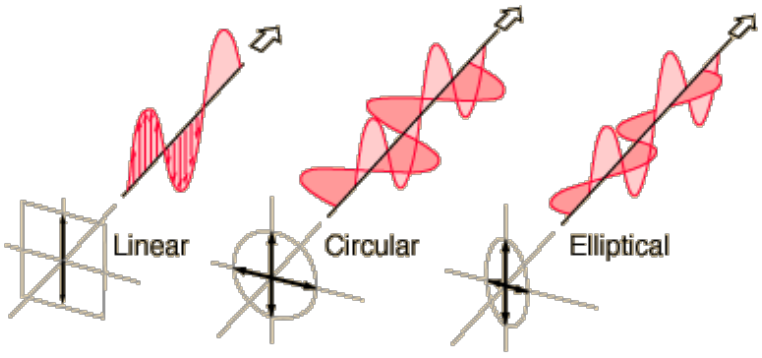

Figure 4.1: Illustration of linear (left), circular (middle) and elliptical (right) polarizations of EM waves [8]

plane perpendicular to the direction of propagation of wave (See Fig. 4.1 (left)).

2. **Circular polarization:** If the magnitudes of E_1 and E_2 are equal, but there is 90° phase difference between them then the resultant electric field rotates in a circle in a plane perpendicular the of propagation and, depending on the rotation direction, is called left- or right-hand circularly polarized light (see Fig. 4.1 (middle))

3. **Elliptical polarization:** This is the most general description of a polarized light. When neither the magnitudes of E_1 and E_2 are equal nor their phase difference is 90°. In this case, direction of the resultant electric field of light inscribes an ellipse with time on a plane perpendicular to the propagation direction of light. (see Fig. 4.1 (right))

4.2 Stokes vector as a representation of polarization

In 1852, G. G. Stokes introduced a new way to represent the polarization of light. He introduced four quantities called as 'Stokes Parameters', which were the functions of observables of an EM wave. Unpolarized, partial or totally polarized states of light can be described in terms of these quantities termed as 'Stokes vectors'. This representation is widely used in modern days to give a mathematical description of polarization of light. Apart from light, this representation of polarization is also applicable to describe the polarization of **particles** [39].

Stokes vector consists 4 Stokes parameters $\mathcal{S}_0$, $\mathcal{S}_1$, $\mathcal{S}_2$ and $\mathcal{S}_3$. There $\mathcal{S}_0$ represents the irradiance of the light, $\mathcal{S}_1$ and $\mathcal{S}_2$ represents the linear polarization of light. For the light polarized along horizontal axis in the plane $\mathcal{S}_1 > 0$ and for the light polarized along vertical axis $\mathcal{S}_1 < 0$. Light can also have a polarization which is oriented in a direction, giving no preference to any of the orthogonal axes in the plane ($\mathcal{S}_1 = 0$). There $\mathcal{S}_2$ represents the polarization state oriented in a direction, which makes $\pm 45^\circ$ angle with the horizontal axis ($\mathcal{S}_2 > 0$ for $+45^\circ$ and vice versa). $\mathcal{S}_3$ represents the circular polarization of light. For right handedness of circularly polarized light $\mathcal{S}_3 > 0$ and for left handedness $\mathcal{S}_3 < 0$ [40].

In general, the Stokes vector ($\mathcal{S}_0$, $\mathcal{S}_1$, $\mathcal{S}_2$ and $\mathcal{S}_3$) is written considering the irradiance of light to be unity. For example, natural light (unpolarized light) is expressed as (1, 0, 0, 0) and horizontal polarized light as (1, 1, 0, 0). Similarly, left circular polarized light as (1, 0, 0, -1). A few examples of representing the other polarization states as Stokes vector are presented in Table 4.1.

The GEANT4 handles both linear and circular polarizations of particles using the Stokes vectors [41] managed by 'G4StokesVector' class. However, instead of four, it uses three component Stokes vector. It considers the irradiance of the light to be 1, therefore it does not include irradiance component in the Stokes vector [41]. A user can provide the polarization of the primary particles (**direction of oscillation of electric field**) using the 'SetPolarization()' method of 'G4ParticleGun' class object.

Light polarization	**Stokes vector**
Linearly polarized along horizontal axis	(1, 1, 0, 0)
Linearly polarized along vertical axis	(1, -1, 0, 0)
Linearly polarized at $+45^\circ$ to horizontal axis	(1, 0, 1, 0)
Linearly polarized at -45° to horizontal axis	(1, 0, -1, 0)
Right handed circularly polarized	(1, 0, 0, 1)
Left handed circularly polarized	(1, 0, 0, -1)

Table 4.1: Stokes vector representation of different polarization states of light

4.3 Compton Scattering as a tool for polarization measurement

Polarization of a visible range photons can be measured experimentally using some optical methods involving the polarizers, birefringent crystals [40] etc. However, the measurement of polarization of high energy (keV range) photons can not be done by such optical methods. Because for higher energies of incident photon, refractive index of material reaches close to 1, therefore optical phenomenons like refraction, reflection etc. become insignificant in such circumstances[42]. Consequently a different approach is needed to measure the polarizations of high energy photons.

Compton scattering of photons provides a tool for experimentally exploring their polarization aspects. The Klein-Nishina formula for Compton cross section [43] is given as:

$$\frac{d}{d\Omega}\left[\sigma(E,\theta,\eta)\right] = \frac{r_0^2}{2}.\left(\frac{E'}{E}\right)^2.\left(\frac{E}{E'}+\frac{E'}{E}-2\sin^2\theta.\cos^2\eta\right) \tag{2}$$

As visible from Eq. (2), Compton scattering cross section is maximum for $\eta = 90°$, which means that Compton scattering occurs most likely in a plane which is perpendicular to the polarization vector of the photon (see Fig. 4.2a). In other words, the plane made by the directions of incident and scattered photons is perpendicular to that made by the direction of incident photon and its polarization vector. Also, as we can see in Fig. 4.2b, this effect is more visible for a specific range of θ (around 82° for 511 keV photons [9]). Using these observations, we can statistically estimate the direction of photons initial linear polarization ϵ by taking a cross-product of photon momentum vectors before and after the Compton scattering.

$$\hat{\epsilon} = \hat{k} \times \hat{k'} \tag{3}$$

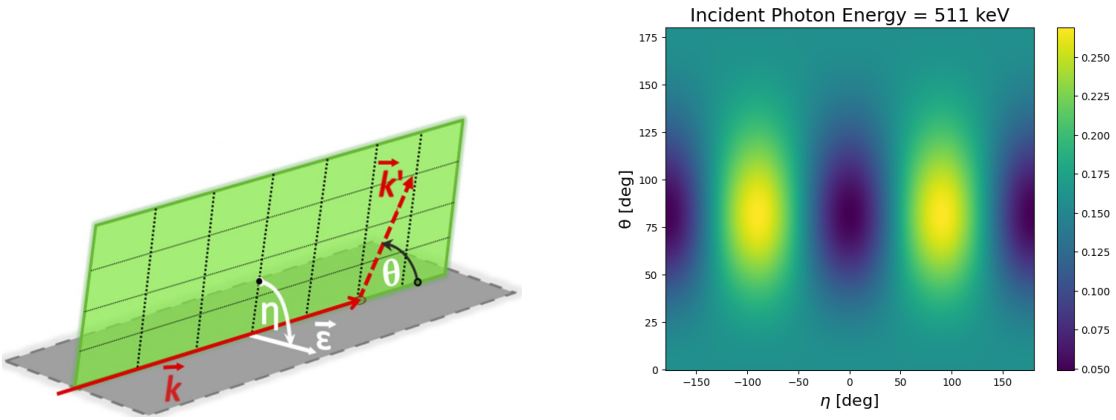

(a) (b)

Figure 4.2: (a) Definition of θ and η in Compton scattering [9]. 2D plot showing the variation in η at different θs for scattering of a 511 keV photon (image generated from a python script taking the help from [10])

In the following sections, we make a case study using the detector geometry similar to that of ongoing J-PET Experiment [21] as a reference.

4.4 J-PET detector as a tool to precisely study the positronium decay

The J-PET detector [21], Jagiellonian Positron Emission Tomograph is developed in Cracow (Poland). The J-PET detector is a novel PET device based on plastic scintillators which is designed for both the fundamental physics research with precision studies of positronium decays as well as the medical research with total body scannings.

Some key features

In J-PET detector to create positronium atoms, there is a radioactive source (^{22}Na isotope) of activity 1 MBq which emits positrons via β decay. The source is placed inside a porous polymer XAD-4 [44] which is present inside an annihilation chamber placed at the center of the detector. The positrons from the source first gets slowed down in the surrounding medium and forms a positronium atom in the pores of the medium as it interacts with the electrons of the medium [21]. Depending on its spin, the positronium subsequently decays to final states constaining two (para-positronium) or three photons (ortho-positronium) as

explained in Chapter 1.

The detector tiles in J-PET are made from Polyvinyl Toluene based EJ-230 plastic scintillator [45] tiles with dimensions $7 \times 19 \times 500\ mm^3$ placed in three concentric layers having radius 42.5 cm, 46.75 cm and 57.5 cm [21](see Fig. 4.3a) and in a newly added modular layer [46] (see the schematic diagram in Fig. 4.3c). The scintillator tiles are coupled with R9800 photomultiplier tubes (PMT) [47] at both the ends along the cylinder axis. It allows one to reconstruct the photon hit position along the scintillator tile based on the time difference between the pulses coming from the two PMTs at both the ends of a tile. In the plastic scintillators, photons below 10 MeV energy interact predominantly via the Compton effect, as is the case for photons of interest in this thesis. Time and position of the photon hits and the energy deposited in the tile is extensively used for analyzing events to infer the information about polarization.

Time and position resolutions of the J-PET detector are approximately 380 ps and 4.6 cm (in FWHM), respectively. This position resolution corresponds to 2.4 degree resolution (in FWHM) in scattering angle measurement. The readout in J-PET is equipped with the dedicated field programmable gate array platform (FPGA) and trigger-less data acquisition system, due to which the detector is capable to avoid the pileup events coming from the higher rates of the positronium production which is necessary to have enough statistics for analyzing the data.

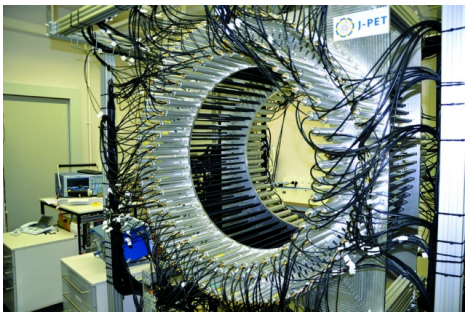

(a)

(b)

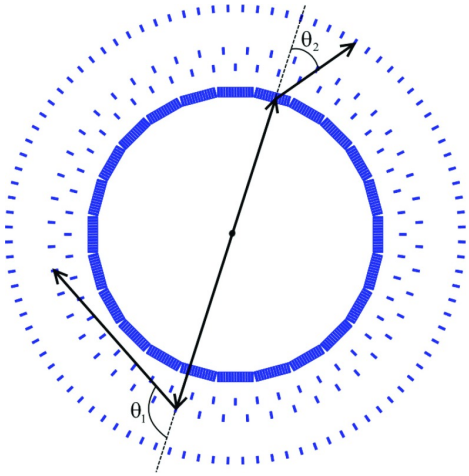

(c)

Figure 4.3: (a) J-PET detector with three layers of scintillators [11], (b) annihilation chamber at the center [11] (c) schematic of transverse view of JPET [12]

4.5 Creating a setup to study the photon polarization in simulation

4.5.1 Simulation setup

In our simulation, we created a detector geometry which is similar to the actual J-PET setup except that we use a different material in the outermost layer to get enough hits for analyzing the events. Following are some key components of our detector geometry:

1. **World volume:** In our setup, we have defined a **cube** shaped world volume of dimension $1.5\ m \times 1.5\ m \times 1.5\ m$. We have put vacuum inside the world volume using **'G4_Galactic'** material, which is available in GEANT4's internal material database

[48] through 'NIST' library [49]. We chose vacuum instead of air to avoid the Compton scattering of the incoming photons from the air molecules.

2. **Detector tiles:** We created an arrangement of plastic scintillator tiles as shown in Fig. 4.4. To create that geometry, first we create a solid volume of box shape. Then we rotate it at a suitable angle and place it in one of the four circular layers and repeat it form the other circular layers of the detector.

   (a) 1^{st} **layer:** The first (innermost layer) has a radius of 362 mm. It contains 312 strips of plastic scintillators of dimensions $6\ mm \times 24\ mm \times 500\ mm$.

   (b) 2^{nd} **and** 3^{rd} **layer:** The second and third layers have radius 425 mm and 467 mm respectively. Both the layers contain 48 strips of plastic scintillators of dimension $7mm \times 19\ mm \times 500\ mm$.

   (c) 4^{th} **layer:** The fourth (outermost) layer has a radius of 575 mm. It contains 96 strips of BGO (Bismuth germanate) scintillator of dimension $7\ mm \times 19\ mm \times 500\ mm$. In actual J-PET setup there are plastic scintillators in the outermost layer instead of BGO.

   Note: Here we acknowledge the help from ChatGPT (OpenAI) [10] for generating a code to create a basic geometry of the J-PET detector, which we fine tuned further.

3. **Physics list:** We have used 'G4EmLivermorePolarizedPhysics' module of GEANT4 physics list [36]. This module can handle the electromagnetic interaction of the particles at low energies along with the polarization of the particles.

   Note: In our current simulation, we are not invoking the scintillation photons within the detector tile. We have used the truth information to get the relevant information of particles from the detector tiles as our focus is to study the polarization measurement conceptually.

4. **Photon source:** In our simulation, we have used a photon gun as a photon source, which shoots photons of known energies. In the actual J-PET setup, photons originate from the positronium decay or annihilation.

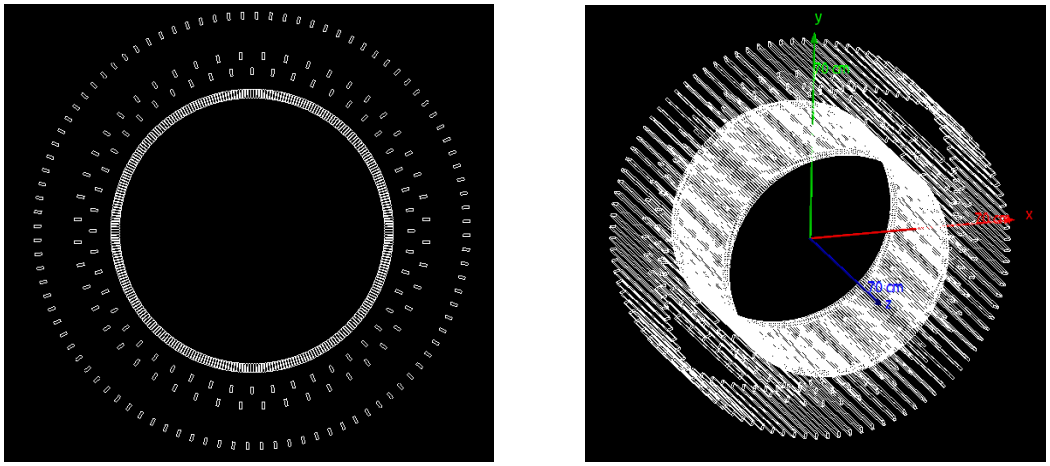

(a) (b)

Figure 4.4: (a) Detector geometry in x-y plane in simulation, (b) Detector geometry with coordinate axes shown

4.5.2 Extracting information of photon interactions with the detectors

In the simulation, we are extracting the data from the detectors in the form of a 'hit' (a packet of information) generated by the sensitive detectors. We created a custom class for sensitive detectors (inherited from 'G4VSensitiveDetector' class) to define the conditions to process and store the hits. We created a custom class for a hit also (inherited from 'G4VHit' class) to define the methods to store the relevant information in a hit.

Information stored in a hit

In our simulation, we have defined every scintillator tile to be a sensitive detector so that they can generate and process the hits. Following are some key information we store in a hit:

- Position of the interaction point
- Time of the interaction (t = 0, when gun shoots a photon)
- Physics process via which the interaction takes place
- Detector ID of the tile where interaction happens
- Gun ID of the particles.

- Compton scattering angle (θ).
- Angle between the scattering plane and the polarization plane (η)
- Photon momentum direction at post step point.

Conditions to store a hit:

In a detector, there happens a lot of interactions before the particle is completely absorbed in the material or leaves the detector such as multiple scattering, ionization processes etc. For our study only few of these interactions are relevant and we store only those as a hit. In our simulation, we defined the following conditions on an interaction to be qualify as a hit:

1. In an event, we are storing the information of the interaction of primary photon (originating directly from gun) only.
2. The process by which interaction takes place, should be any one of the following:
   (a) Compton scattering
   (b) Rayleigh scattering
   (c) Photoelectric absorption
3. Except for Rayleigh scattering, energy deposited in a step and the step-length should be greater than zero.

4.6 Studying the events with single photon

By studying the single photon events, we want to verify some of the results predicted by the Klein-Nishina Compton cross section as mentioned in Eq. (2)

4.6.1 Gun parameters

1. **Gun position:** We have put the photon gun at the center of the cylinder (formed by the scintillator tiles) at (0,0,0).
2. **Energy of the photons:** We want to mimic the energy of a photon coming from the e^+e^- annihilation or the para positronium decay. Therefore, we fix the energy of photons at 511 keV for all events.

3. **Direction of the photons:** Randomized uniformly in x-y plane and across the detector tile length (z direction, see Fig. 4.4b for coordinate system in the geometry). To randomize the momentum direction, first we define a unit vector along y axis and rotate this vector about x-axis, by an angle, which is randomized in the range -0.0644 radians to +0.0644 radians. This way momentum direction remains within the z acceptance of the tiles. Then we again rotate this vector about z-axis by an angle, which is randomized uniformly in range -2π radians to $+2\pi$ radians to cover the whole x-y plane. This way final momentum direction is randomized in 3D.

   As we see in Fig. 4.6a, plotting the x vs y coordinate of the hits, the detector geometry in transverse (x-y) plane gets reconstructed. The sharp cut visible in the distribution of z position (Fig. 4.6b) at $\pm 250\ mm$ is due to restricting the incoming photons within the length of the scintillator tiles.

4. **Polarization directions of the photons:** Polarization direction of a photon is always perpendicular to the propagation direction of the photon. Therefore, we define the polarization direction of the photon as a unit vector which is randomized in a plane perpendicular to the photon momentum direction. (see the distributions in Fig. 4.6c and Fig. 4.6d)

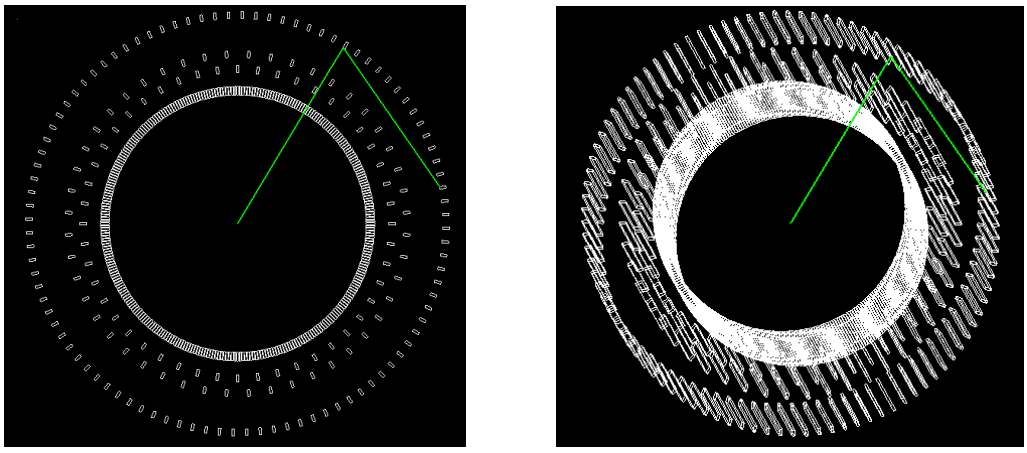

(a) (b)

Figure 4.5: Event display of a event with single photon shoot from center, where photon undergoes Compton scattering followed by a photoelectric absorption: (a) in transverse (x-y) plane, (b) in 3D.

4.6.2 Calculating the number of hits (nHits) in an event:

- We count any hit which arises from Compton scattering or photoelectric absorption of the primary photon in the material. We do not count the hit which arises from the Rayleigh scattering as energy deposited via this process is zero. It does not produce any detectable signal in a real experimental setup.

- If a photon undergoes multiple interactions within a single detector tile before it is fully absorbed or scattered out of detector, we count all those interactions as separate hits. However, such distinction between the hits in a single tile will not be possible in a realistic setup.

- For analysis, we take only those events where the first hit arises from Compton scattering. We primarily analyze that first Compton hit only in an event as we are interested in studying the Compton scattering of a photon which comes directly from the source.

Fig. 4.6e shows the distribution of no. of hits (nHits) in the event for 100000 events. There number of events decreases exponentially as we ask for more number of hits. Fig. 4.6f shows the registration time of the first Compton hit. The four peaks there correspond to hits in the four different layers in the detector.

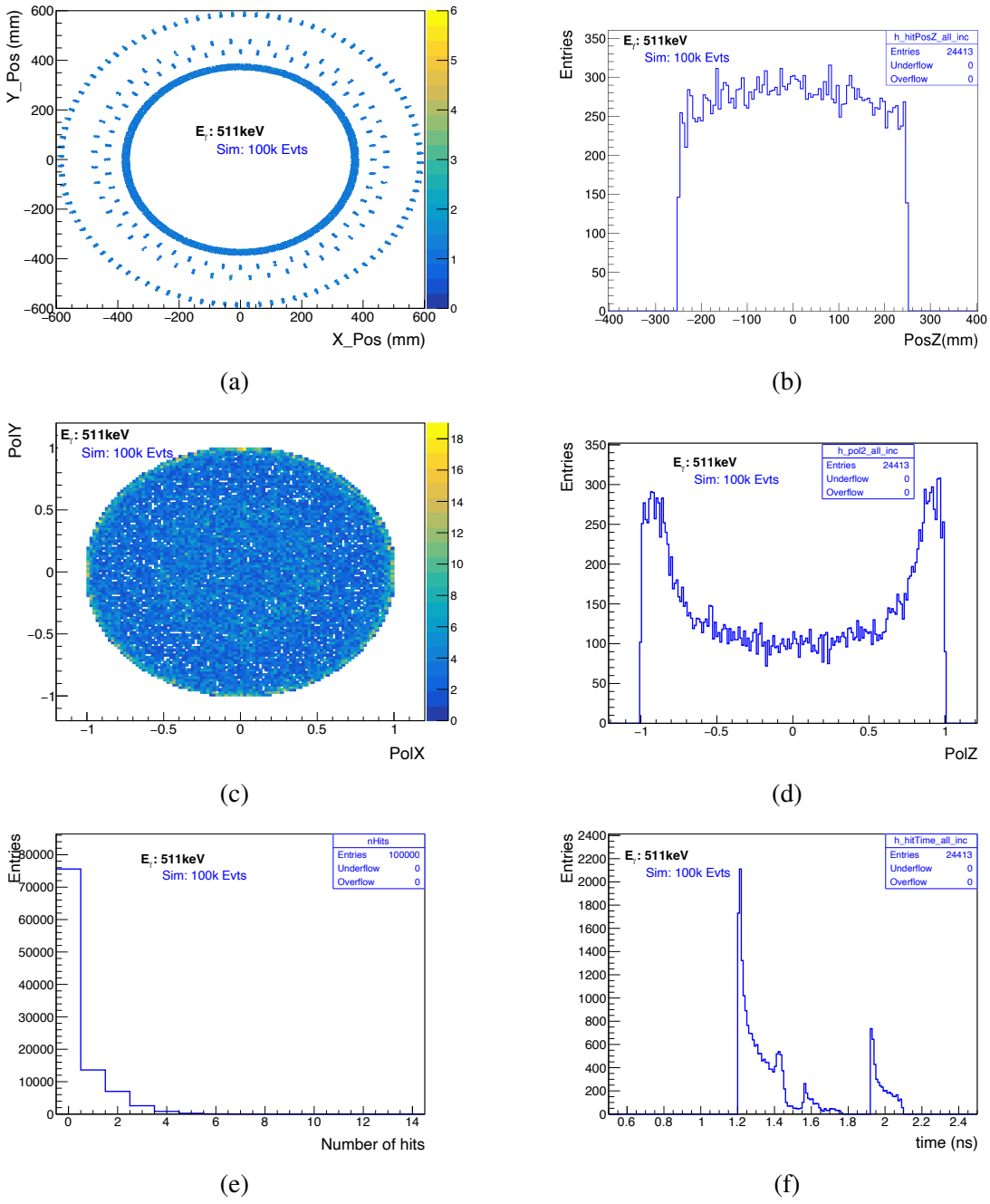

Figure 4.6: Distribution of some information of the $1st$ Compton hit in the event: (a) 2D plot of x and y coordinate of the hit, (b) distribution of z coordinate of the hit, (c) 2D distribution of x and y component of the photon polarization direction, (d) distribution of z component of the polarization direction, (e) distribution of number of hits produced in an event, (f) distribution of registration time of hit,

4.6.3 Calculation of Compton scattering angle

There are two ways to calculate the Compton scattering angle (θ):

1. **Using the momenta directions (truth information):** In simulation the Compton scattering angle θ can be calculated by taking the scaler product between the photon momentum directions at **'pre-step point'** (momentum direction before scattering) and the **'post-step point'** (momentum direction after scattering) as:

$$cos\theta = \hat{p}_{pre} \cdot \hat{p}_{post} \tag{4}$$

2. **Using the hit positions (closer to reality):** For this method, we require at least two hits in an event (for single photon case). First we sort the hits of an event in the ascending order of their registration time. Then, using the position of the hits we reconstruct the incoming and scattered photon momenta directions ($\hat{k}$ and $\hat{k'}$). Then we calculate the scattering angle θ by taking the dot product of those two reconstructed photon momentum directions.

$$\cos\theta = \frac{\vec{x}_{in} \cdot \vec{x}_{scat}}{|\vec{x}_{in}|\ |\vec{x}_{scat}|} \tag{5}$$

where

$$\vec{x}_{in} = \vec{x}_{hit1} - \vec{x}_{gun}$$

$$\vec{x}_{scat} = \vec{x}_{hit2} - \vec{x}_{hit1}$$

Fig. 4.7a shows the distribution of scattering angle θ. The distribution has a maxima around 40 degrees, which is consistent with the expected value for the Compton scattering of 511 keV photons.

4.6.4 Calculation of η:

The angle between the scattering plane and the polarization plane, denoted as η, cannot be determined in a realistic way event by event but has to be inferred statistically from a sample of events of positronium decays. For our studies, we have calculated the η using the truth level information from the steps. Now, η can also be interpreted as the azimuthal angle between the incoming photon polarization direction ($\hat{\epsilon}$) and the scattered photon momentum vector ($\hat{k'}$) with reference to the direction of the incoming photon momentum($\hat{k}$)

direction. In GEANT4 simulation, such thing can be done using the 'azimAngle()' method of **CLHEP::Hep3Vector** class. As shown in Fig. 4.7b, the distribution of η has maxima at $\pm 90^{\circ}$ as described in Section 4.3. In Fig. 4.7c, we have shown the unnormalized 2D distribution of θ vs η which is consistent as expected from the Klein-Nishina Compton cross section formula. Also Fig. 4.7d shows that a Compton scattered photon carries more energy if it is scattered in a lower scattering angle, which is consistent with the expectation from the relation of scattered photon energy with the scattering angle [43].

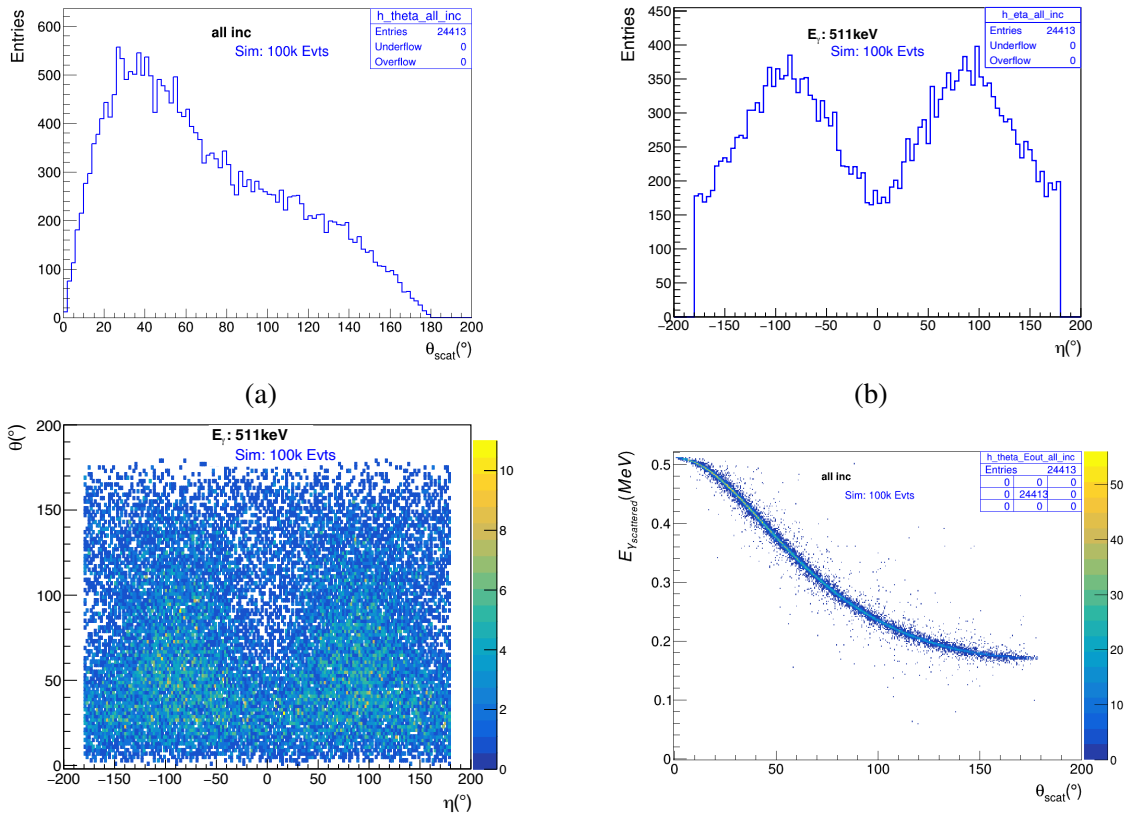

Figure 4.7: 1D distribution of Compton scattering angle (top left plot) and η (top right plot). 2D plots for comparing θ vs η (bottom left plot) and scattered photon energy vs θ (bottom right plot)

4.7 Studying the events with two photons in the simulation

We make use of the observation from the studies with single photon events that polarization direction of an incoming photon of given energy is more preferably perpendicular to the

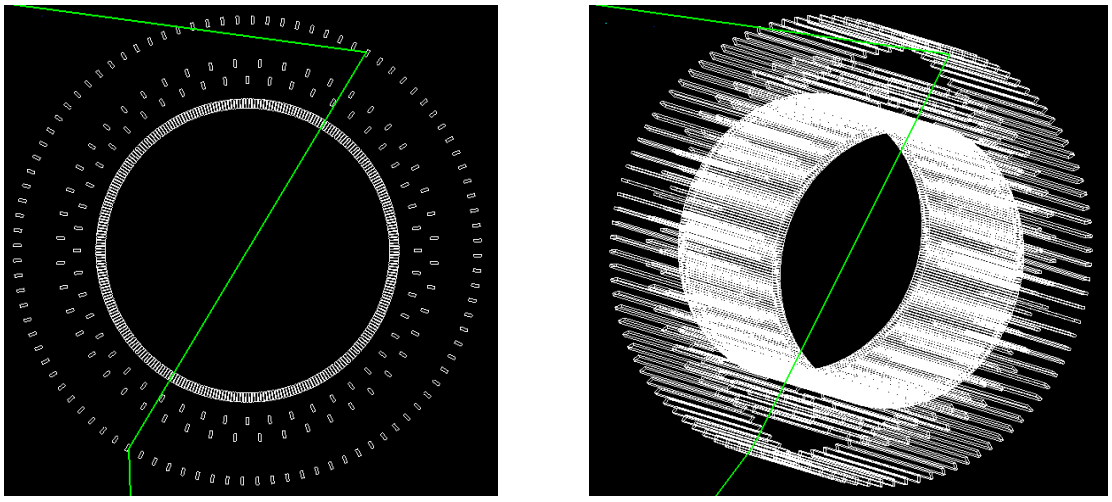

(a) (b)

Figure 4.8: Display of an event with two back to back 511 keV photons, where both the photons leaves the detector after the first Compton scattering: (a) in transverse (x-y) plane, (b) in 3D

Compton scattering plane for a certain range of θ. We exploit this observation for the case of the two photons resulting from annihilation or para-positronium decay and are maximally entangled, to estimate the relative angle between the polarization vector of two photons.

We do not explicitly simulate the positronium for our studies. Instead, we mimic the annihilation photons by simulating back to back two photons having energy 511 keV. We also mimic the maximal entanglement of photons by manually setting their polarizations orthogonal to each other in each event [50].

Changes in the photon gun parameters: In the simulation we add one more photon gun at the center which shoots the photons with the same 511 keV energy but in the opposite direction to the first photon momentum direction (see Fig. 4.8). In this scenario, an event starts with shooting the two photons one after the other from the guns (simultaneously) and the event ends with complete tracing of all the particles involved (both primary and secondary) through the detector volume.

Same as before, the polarization of first photon is randomized in a plane perpendicular to the momentum direction, but now we set the polarization of the second photon in a direction perpendicular to the polarization direction of the 1^{st} photon to mimic the maximal entanglement between the photons.

4.7.1 Methods and event selection

Identifying hits from incoming annihilation or decay photons and photons scattered in the detector: Using truth information in simulation, we identify the hits which originated from the interaction of the photon coming directly from the gun and refer them as **'annihilation photon hit'** (consistent with the terminology of e^+e^- annihilation). We identify the annihilation photon hits by putting a condition on a hit that it should have been originated from Compton scattering of the primary photon and the kinetic energy of that photon before the scattering should be equal to 511 keV.

In a similar manner, we identify the hits from the scattered photon by putting a condition that the hit should have been originated from either Compton scattering or photoelectric absorption of the scattered primary photon, and the kinetic energy before interaction should be less than 511 keV.

Counting the number of hits in an event:

We count only those hits which are originated from Compton scattering or the photoelectric absorption of the incoming photons. A photon can undergo multiple interactions before getting absorbed or leaving a detector tile. In such scenario, out of the multiple interactions within a single tile, we count only the 1st interaction there as a hit and use it's information such as position, time, etc for analysis. As mentioned earlier also such distinction between the multiple hits within a single detector tile won't be possible.

Selecting the 4 Hit events

We select only those events where exactly 4 hits are present, so that the Compton scattering angle of both the annihilation photons could be calculated in a realistic way. In our study, we select events having 4 hits by putting the following conditions:

- The event should be containing two annihilation photon hits.
- Other 2 hits should be originated from the interaction of scattered photons corresponding to different annihilation photons.
- All four hits should be in four different tiles.

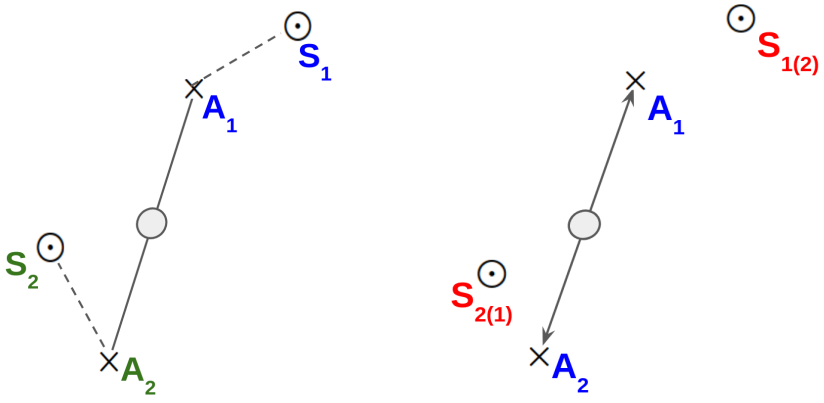

(a) (b)

Figure 4.9: An schematic of 4 hits in an event: (a) at truth level, (b) in reality (before connecting)

4.7.2 Analyzing the time difference between any two hits:

In simulation, we can know that a scattered hit correspond to which of the two annihilation photon hits (see Fig. 4.9a). In the figure, A_1 and A_2 are the hits from the annihilation photons and S_1 and S_2 are their corresponding scattered photon hits. To get an idea about time separation between any two hits in an event, we see the distributions of time difference between all combinations of two hits in the event (total ${}^4C_2$ combinations). There we expect that both the annihilation photon hits should be time separated from their scattered photon hits in a similar manner which is visible in Fig. 4.10. Similarly, we expect that the annihilation photon hit should be time separated from scattered photon hit corresponding to the other annihilation photon hit (for example time separation between S_1 and A_2), which is visible in Fig. 4.11.

In Fig. 4.12 we observe that the time difference between two scattered photon hits has more spread than that of two annihilation photon hits. Because given A_1 on a layer, A_2 can be in any of the four layers but only in the direction opposite to A_1. While given S_1 on a layer there is no such restriction on S_2. The peaks in the distribution of time difference between A_1 and A_2 at non zero values correspond to combinatorial ways of A_1 and A_2 being in the different detector layers in the geometry.

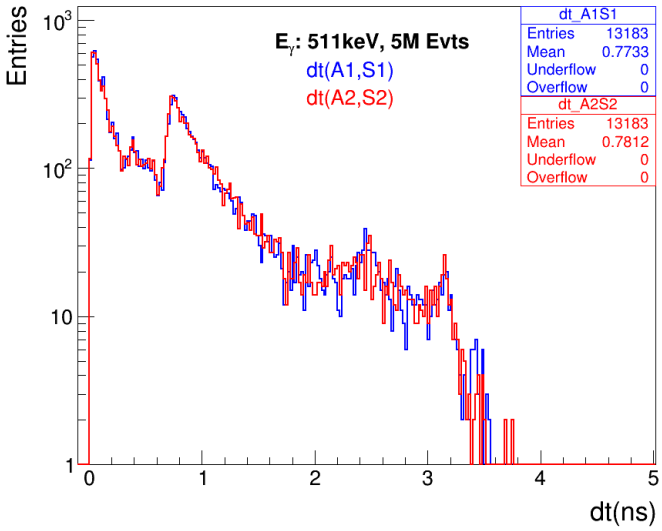

Figure 4.10: distribution of time difference between an annihilation photon hit and its scattered photon hit

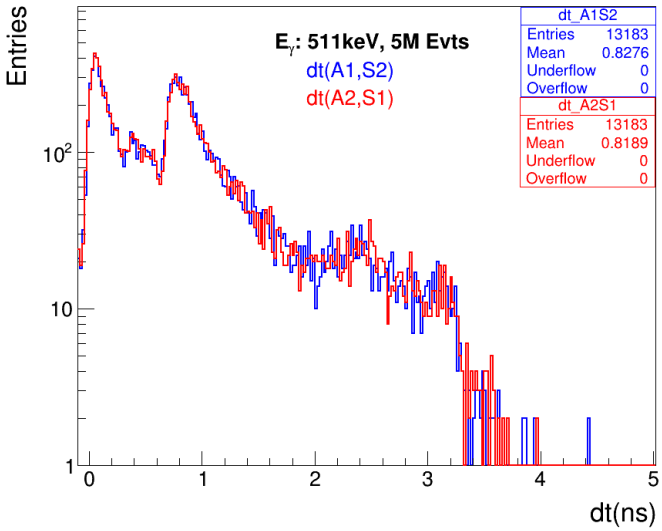

Figure 4.11: Time difference between an annihilation photon hit and scattered photon hit of other photon

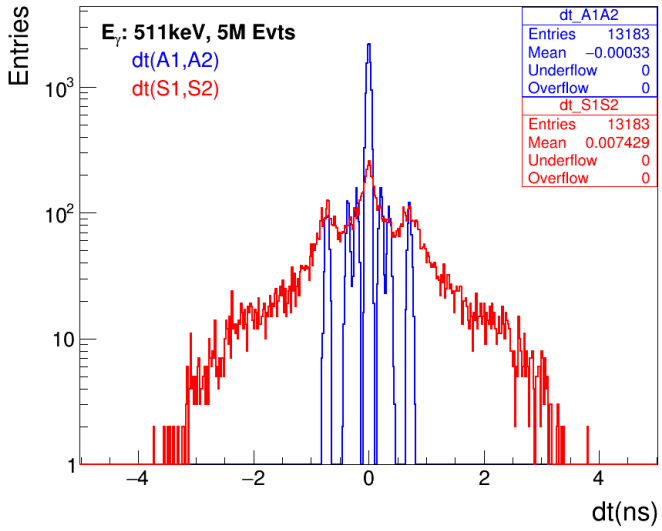

Figure 4.12: Time difference between two annihilation photon hits and two scattered photon hits

4.7.3 Connecting scattered photon hits to their parent annihilation photon hits

We, in reality, do not know a scattered photon hit corresponds to which annihilation photon (see Fig. 4.9b). To get that information, we have used the method as described in a paper from J-PET [9] to connect a scattered photon hit to its corresponding annhilation photon hit to reconstruct the compton scattering angle. First we make the following two hypotheses:

(i) S_1 came from scattering of the first annihilation photon A_1 and S_2 from the second annihilation photon A_2.

(ii) S_1 came from scattering of the second annihilation photon A_2 and S_2 from the first annihilation photon A_1.

To test a hypothesis that j^{th} scattered photon is a result of scattering from the i^{th} annihilation photon, we define a "Scatter Test" value:

$$ST_{i,j} = \Delta t_{i,j} - r_{i,j}/c \tag{6}$$

where $\Delta t_{i,j}$ is the difference between the registration time of the scattered and annihilation photon hits ($t_j^{Scatter} - t_i^{Annihilation}$) and $r_{i,j}$ is the distance between the hit positions of

the annihilation photon (r_i) and scattered photon (r_j). The $ST_{i,j}$ essentially signifies for the time of flight for the light to travel from i^{th} the annihilation photon hit to the j^{th} scattered photon hit.

In simulation, we have the exact time and position of hits (truth information) whether the j^{th} photon is a scatter of the i^{th} photon, therefore $ST_{i,j}$ must be equal to zero other wise non zero (see Fig. 4.13a, there points away from the horizontal and vertical and horizontal lines corresponds to the events where Rayleigh scattering happened before the Compton scattering of the photon). But for actual experimental measurements, the time and the position resolution comes into the picture. Therefore, instead of clear horizontal and vertical lines in the $ST_{i,j}$ distribution, a spread is observed there (see Fig. 4.13b) [9].

To check j^{th} scattered photon is connected to which annihilation photon, we compare $ST_{1,j}$ with $ST_{2,j}$. If the $ST_{1,j} < ST_{2,j}$, then it implies that j^{th} scatter photon is scattered from the 1^{st} annihilation photon A_1. Otherwise it is scattered from 2^{nd} annihilation photon A_2 with $ST_{1,j} > ST_{2,j}$.

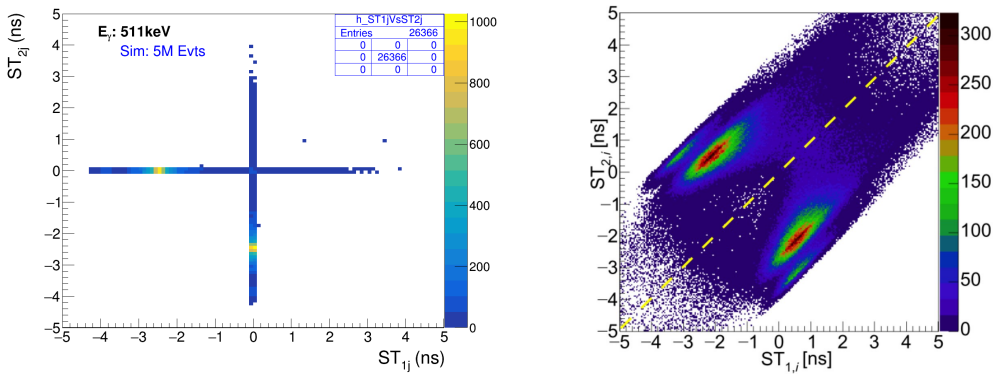

(a) (b)

Figure 4.13: Distribution of ST_{ij} before connecting the hits: (a) in our simulation (idealistic picture), (b) in actual J-PET setup [9]

4.7.4 Estimating the angle between the polarization direction of two photons

The Bose-symmetry and the parity conservation imply that the resulting two photons from the decay of para-positronium are maximally entangled and the photon polarizations are orthogonal to each other [50].

As we have seen in Section 4.3 that polarization direction ϵ of a photon is preferably

perpendicular to the Compton scattering plane (this effect is more visible for a specific range of scattering angle θ and is close to 82° for 511 keV photons). So, the angle between the polarization directions of the two photons can be estimated by angle between their scattering planes (ϕ).(see Fig 4.14).

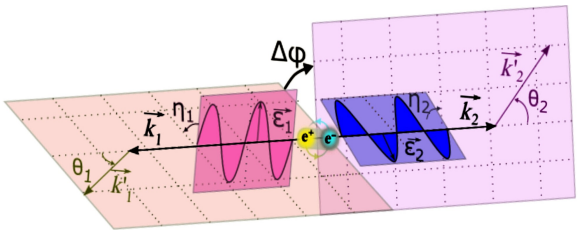

Figure 4.14: Illustration of θ and η in back to back 2γ case [9]

As shown in the Fig. 4.15a, for 511 keV annihilation photons, the dependence of Compton cross section on η is strong near $\theta = 82°$ and have very weak for $(\theta = 0°)$ and $(\theta = 180°)$. The dashed pink line shown in the same figure indicates the optimal range of θ for using Compton scattering as a polarimeter. For $\theta = 82° \pm 30°$, the effect that scattering plane is perpendicular to the incident photon polarization is more visible there [9].

To use the Compton scattering as a polarimeter, both the photons need to interact via Compton scattering. The following expression describes the Compton scattering differential cross section in terms of their scattering angle (θ_1, θ_2) and the angle between their scattering planes ($\Delta\phi$)

$$\frac{d^2\sigma(\theta_1, \theta_2, \Delta\phi)}{d\Omega_1 d\Omega_2} = [A(\theta_1, \theta_2) - B(\theta_1, \theta_2)\cos(2\Delta\phi)] \tag{7}$$

where A and B describe the dependence of the differential cross section on the Compton scattering angles θ_1 and θ_2. At given scattering angles (θ_1 and θ_2), cross section for Compton scattering of both the photons is maximum for $\Delta\phi = 90°$ and minimum for $\Delta\phi = 0°$ or $\Delta\phi = 180°$.

As shown in Fig. 4.15c and Fig. 4.15d, We have verified this in simulation for cases with number of hits $>= 2$ condition for an event so that we can have more statistics to see the effects. However, with this condition on number of hits, calculating θ and $\Delta\phi$ from the position of the hits will not be possible (atleast 4 hits will be required for that). Therefore, we have calculated them using the truth information accessed from the 'step points' in the simulation. Fig. 4.16 shows a comparison of the distribution of $\Delta\phi$ in high and low visibility region.

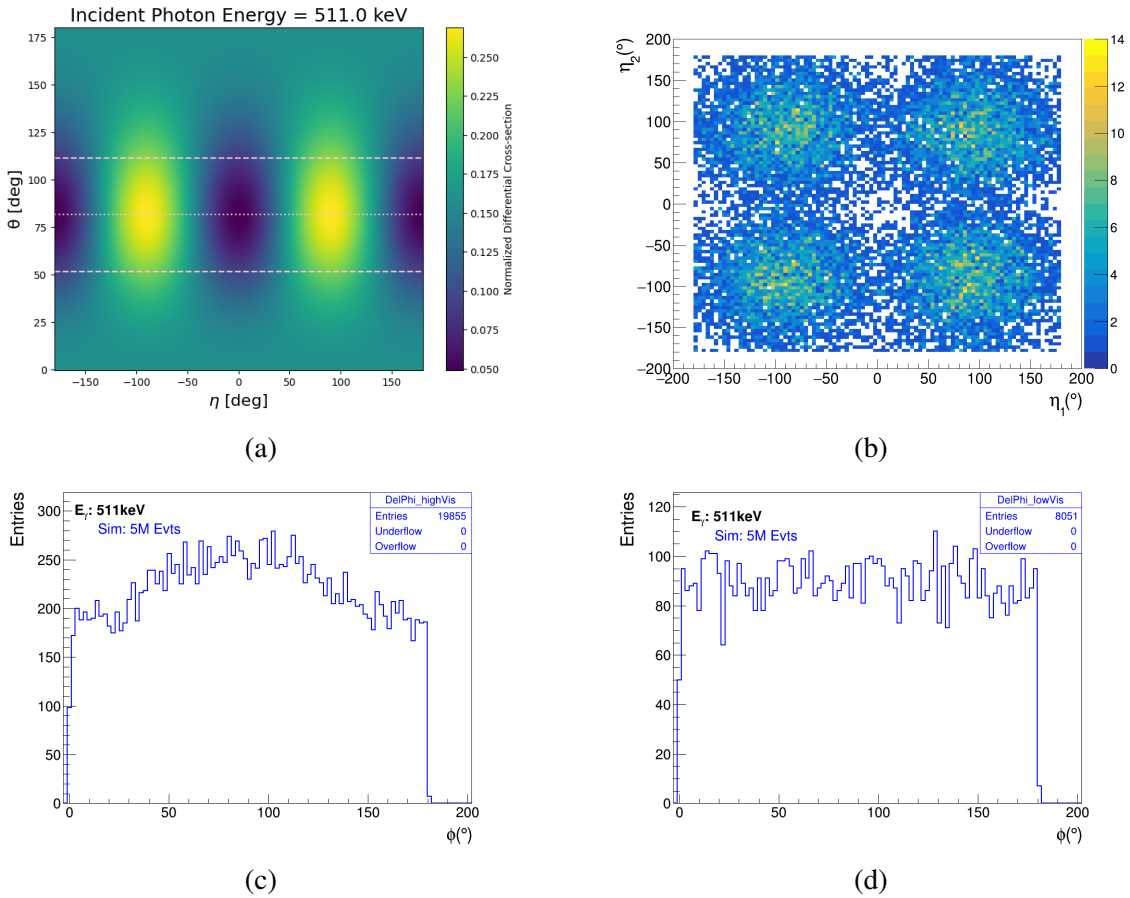

Figure 4.15: (a): Variation in η with θ (optimal range of θ taken from J-PET paper [9]), (b) 2D plot comparing the η of two photons, (c) distribution of $\Delta\phi$ in high visibility range of θ, (d) distribution of $\Delta\phi$ in low visibility range of θ

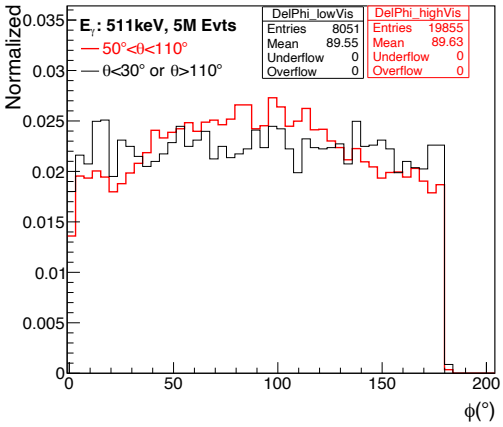

Figure 4.16: Comparing the $\Delta\phi$ distribution (after rebinning) in the high and low visibility range of θ

Summary

In this chapter we have explored the polarization aspect of Compton scattering to measure the polarization of incoming photons. The whole approach is based on the fact that Compton scattering happens preferably in a plane perpendicular to the polarization direction of the incoming photon. InGEANT4 simulation, we have done our studies in a detector geometry which similar to J-PET detector. We explored the techniques to reconstruct the scattering angle using an algorithm followed by J-PET and demonstrated the feasibility of methodologies.

Chapter 5

Summary & outlook

In this project, we have explored the different processes through which a sub-MeV range photon deposits its energy in a material. We studied energy resolution and efficiency of different scintillator materials by analyzing number of scintillation photons produced by energy deposited by incident particles. We studied various aspects of detector configurations on energy resolution and efficiency, namely the material type and thickness, scintillation yield, incident photon energies, etc. Studies presented there can be helpful to optimize the detector material choice and the detector geometry for studying the photons from the decay of positronium in an experiment.

We explored the polarization aspect of the Compton scattering using it as a tool to study the photon polarization experimentally. We simulated a J-PET like geometry and reproduced some of the results from theory and the J-PET experimental results. These studies on photon polarization could be helpful to suppress the background coming from the other processes while studying the photons from the positronium decay. It can also be helpful for photon entanglement studies in an experimental setup.

Future prospects

The polarization correlation between the photons can be measured experimentally via Compton scattering, in which each photon undergoes scattering by angles $\theta_{1,2}$ and having angle between polarization and scattering plane to be $\eta_{1,2}$. As we have seen earlier in Section 4.3 that for 511 keV photons Compton scattering can be used as a polarimeter for $\theta_1 = \theta_2 \sim 82^\circ$.

An attempt in direction was proposed in a study titled “Study of multi-pixel scintillator

detector configurations for measuring polarized gamma radiation" [13]. There they simulated a single-layer position-sensitive detector, which consisted of two detector modules, with 64 scintillating crystals in each module. These modules were arranged in 8 × 8 matrix of square shaped tiles and a photon source placed in between the two modules (see Fig. 5.1a). They did their studies with two different configuration of the detectors: one consisting LYSO (dimension: 3×3×20 mm^3) and other with GAGG (dimension: 2×2×20 mm^3) as a scintillator materials.

In this study, they measured of the polarization correlations of annihilation photons by scintillator pixels read out on only one side by silicon photomultiplier. There they posed a challenge to reconstruct the Compton scattering angle in a single-sided pixilated readout detector. In simulation they have shown that Compton scattering of 511 keV gammas resulted in an ambiguous detector response (see Fig. 5.1b) for $\theta > 60°$ because matrices of the detector could not provide the position information along the detector length. Here one can use the concept device of **"Color Calorimetry"** instead of homogeneous material along the length of a pixel to get the depth of the interaction which we have mentioned in the following section. This way enhancement in the measurement can be done by taking the readout from single face only without increasing the hardware complexities much.

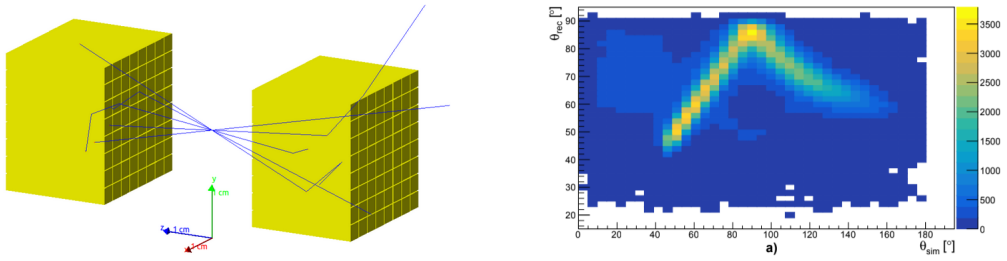

(a) (b)

Figure 5.1: (a) Simulation setup with GAGG detector configuration and the gamma source [13], (b) reconstructed vs. simulated θ in a GAGG module for all event topologies [13]

Color Calorimetry

In particle physics experiments, understanding the longitudinal evolution of particle showers plays crucial role to accurately identify and characterize the incident particles on the detector and helps to study their interactions with matter as well. However in homogeneous calorimeters, it is difficult to get the longitudinal segmentation along the detector length. Color calorimetry is an innovative approach which provides a way to enhance the

precision and capabilities of the traditional homogeneous calorimeters. The idea here is to use a detector module capable of discriminating different emission wavelength emitted from different scintillators placed in the path of incident particle to reconstruct the shower progression (See Fig. 5.2a). The proof of this concept device was verified in a test beam experiment at CERN. [14], where various layers of inorganic scintillating materials having different emission wavelengths were stacked together (see 5.2b). There scintillators were arranged in a decreasing order of their emission wavelength which were read out by the PMT at the end of the module.

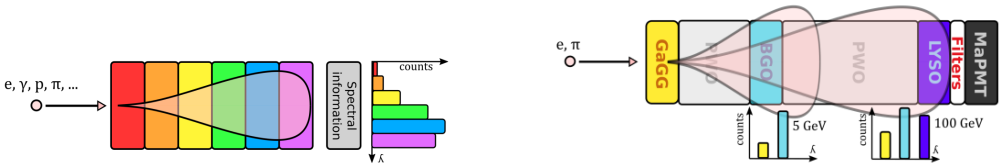

(a) (b)

Figure 5.2: (a) An image illustrating the concept of color calorimetry [14], (b) color calorimeter module schematic [14]

We have verified the proof of the concept device of color calorimetry in our simulation for sub-MeV range photons. We created a stack of GAGG and LYSO scintillators in the decreasing order their emission wavelength (shown in Fig. 5.3) and shoot the 511 keV photons. There we analyzed the emission spectra of the scintillation photons which reach to the rear surface of the detector and saw how does it depend on the z position of the scintillation. To get the longitudinal information from readout at the end, the higher wavelength scintillation photons should have been originated from GAGG (having lower Z coordinate) and vice versa for lower wavelength optical photons from LYSO. As shown in the 2D plot (Fig. 5.4), in the simulation we got the observation consistent with the expectation. Having a working simulation setup with us we look forward to use this concept of colour calorimetry to get photon interaction position along the length of a scintillator in the above mentioned experiment the multipixelated detector setup. With this additional information about the depth of the interaction might help to better reconstruct Compton scattering angle and improved discrimination against background events.

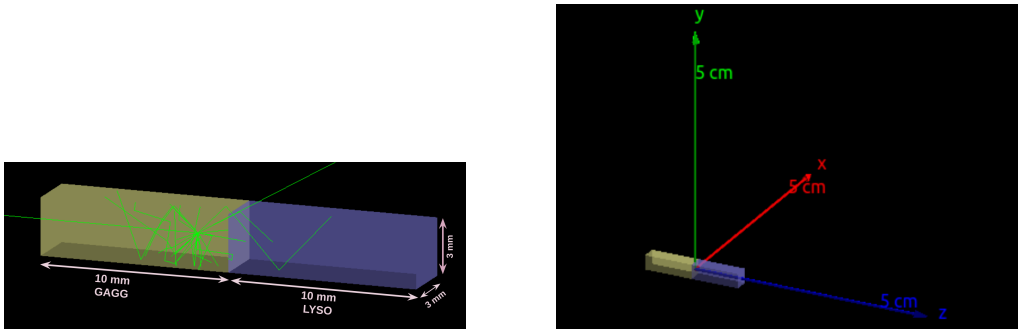

(a) (b)

Figure 5.3: (a) Detector geometry of stack of GAGG and LYSO scintillator, (b) co-ordinate axes in the simulation

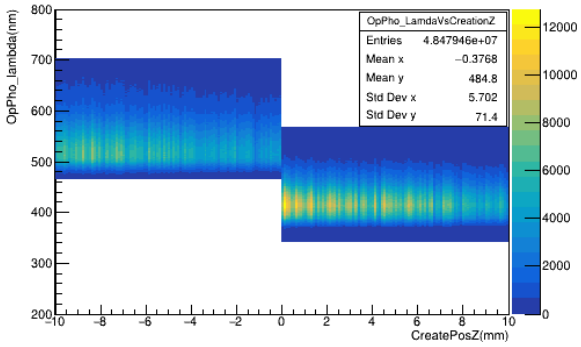

Figure 5.4: Distribution of wavelength of optical photon vs z co-ordinate of point of origin

Appendix A

Plots for $20\ cm \times 20\ cm$ transverse size of the material

A.1 Effect of material thickness in energy deposit

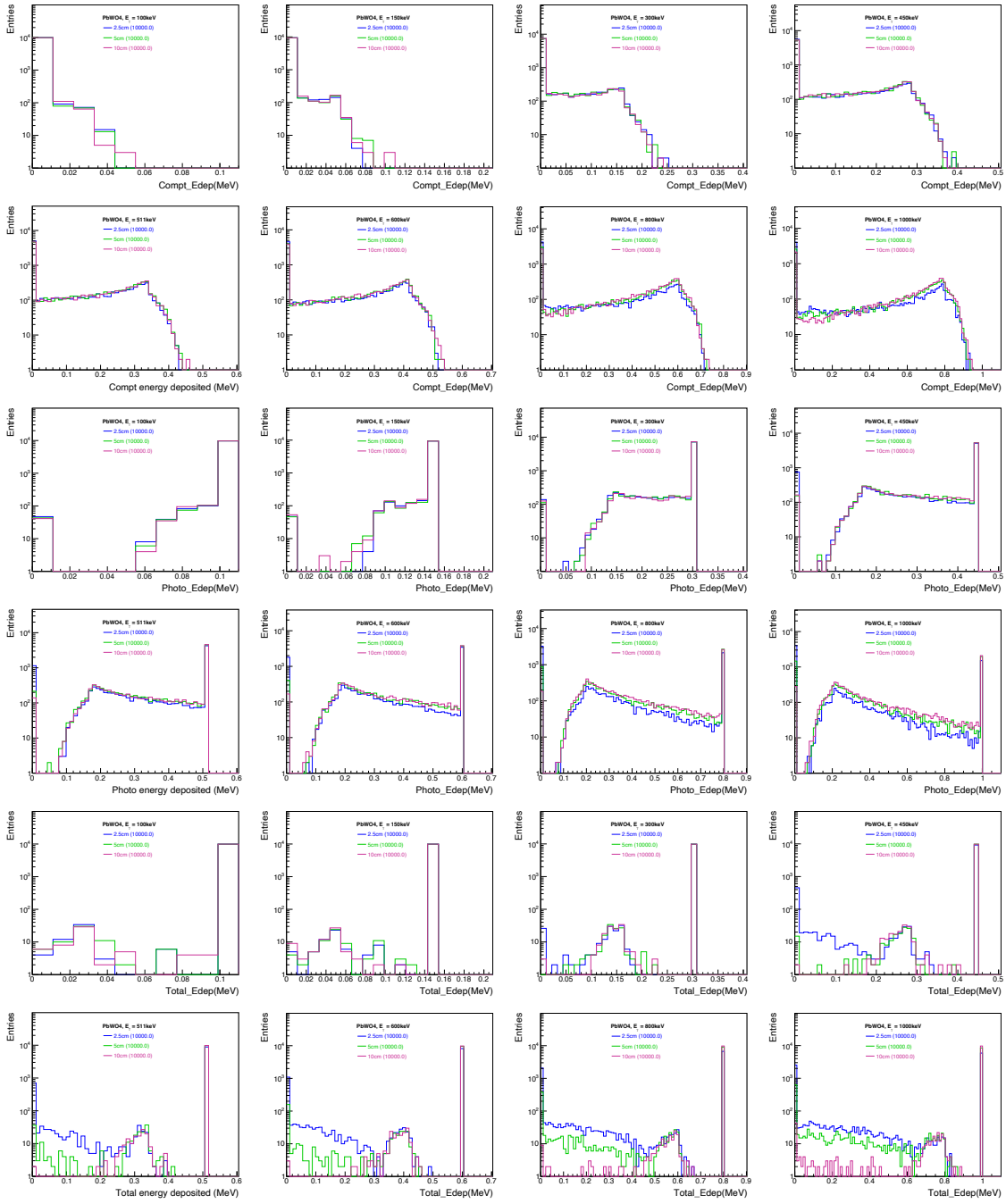

Figure A.1: Effect of material thickness in energy deposited in $PbWO_4$ via different processes (upper two rows Compton, middle two rows photoelectric, bottom two rows total energy deposited) for different incident photon energies.

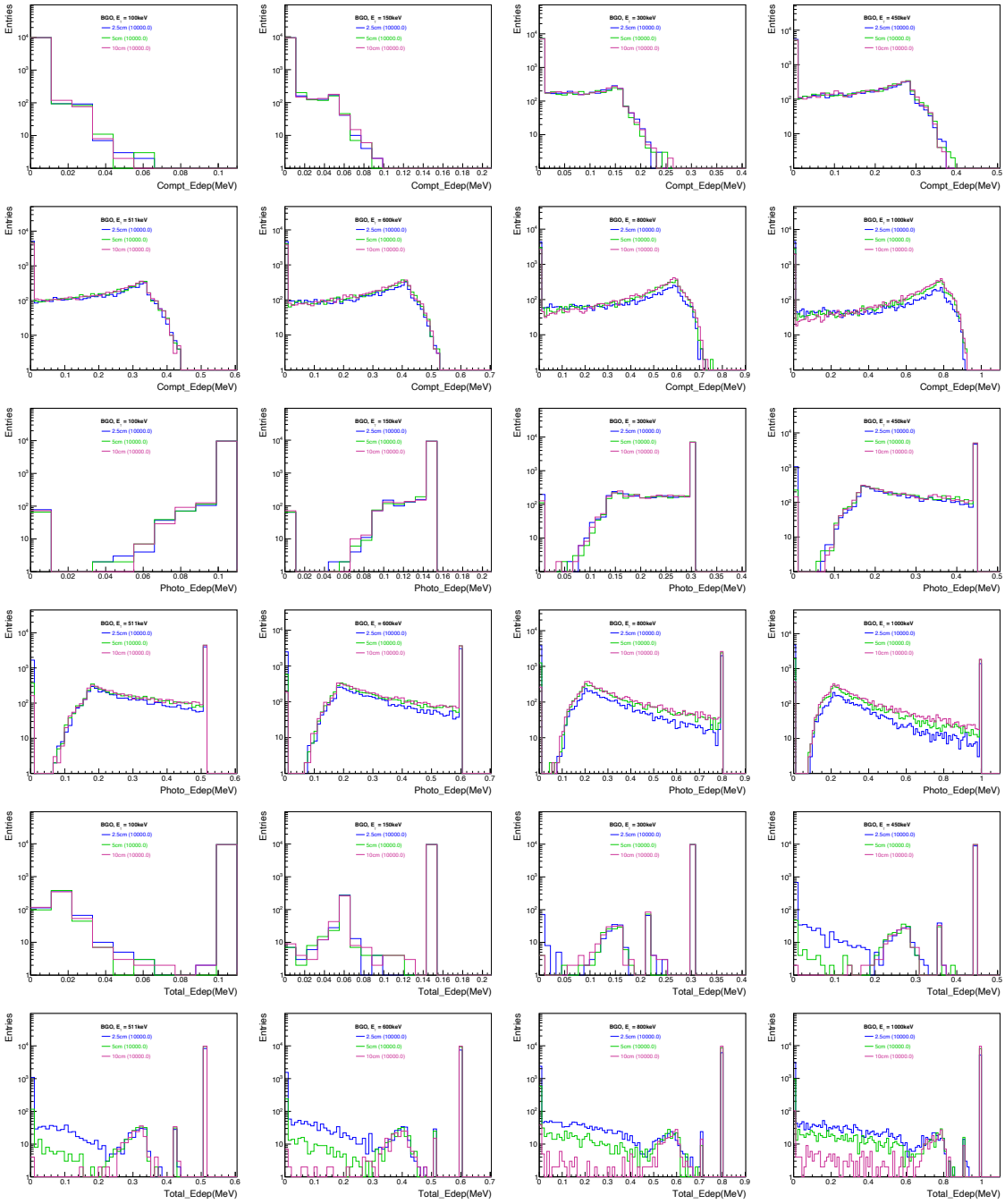

Figure A.2: Effect of material thickness in energy deposited in BGO via different processes (upper two rows Compton, middle two rows photoelectric, bottom two rows total energy deposited) for different incident photon energies.

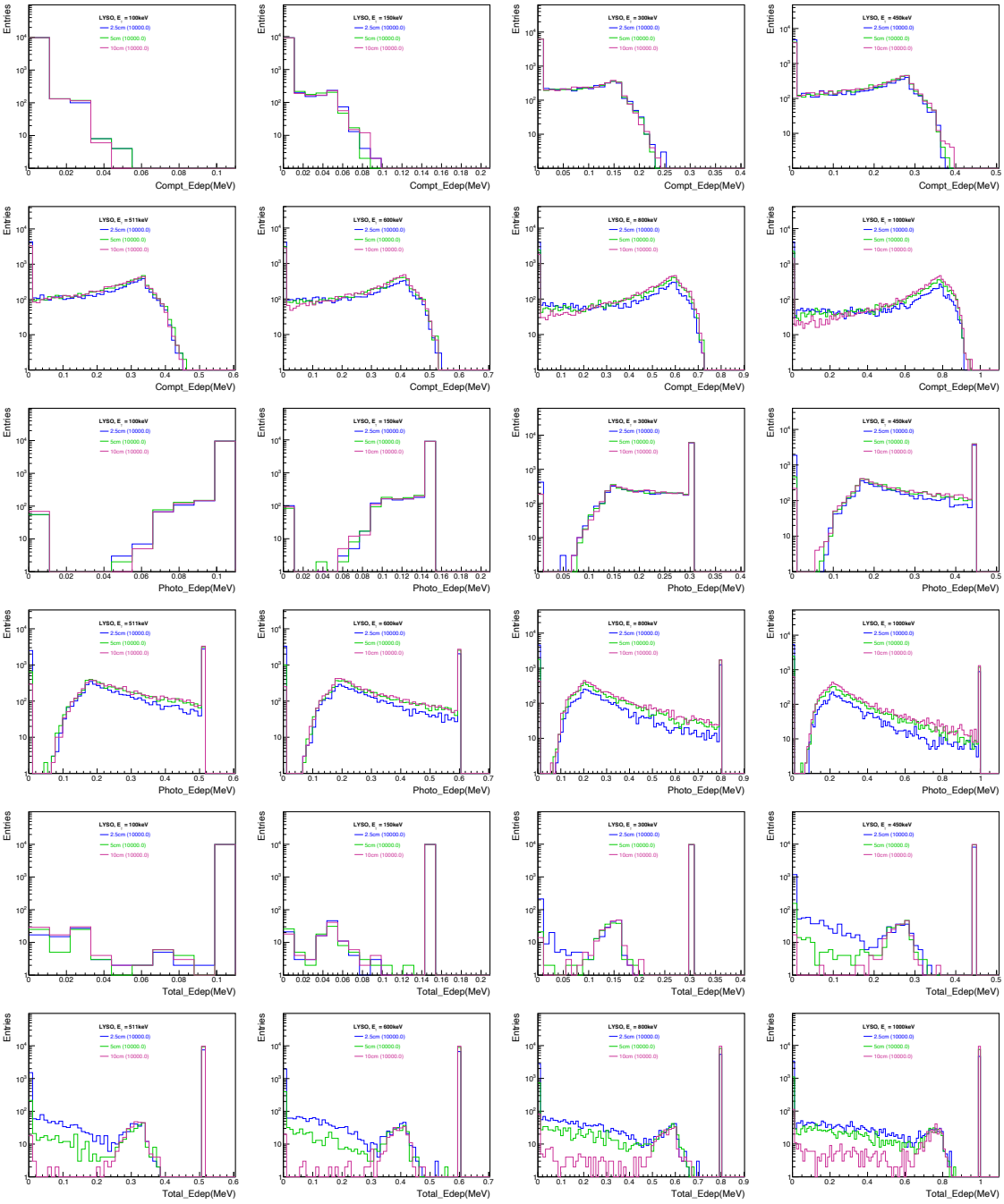

Figure A.3: Effect of material thickness in energy deposited in LYSO via different processes (upper two rows Compton, middle two rows photoelectric, bottom two rows total energy deposited) for different incident photon energies.

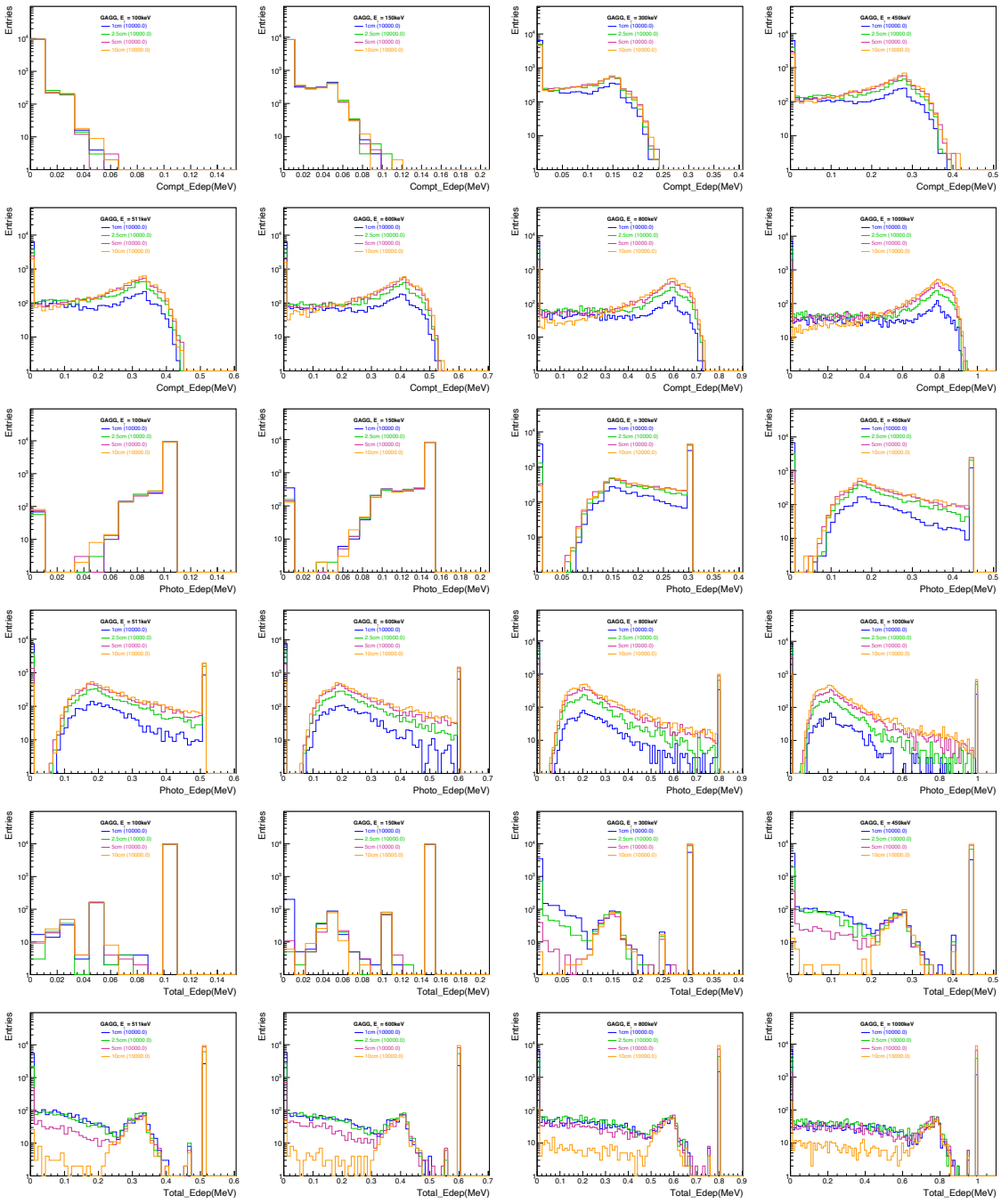

Figure A.4: Effect of material thickness in energy deposited in GAGG via different processes (upper two rows Compton, middle two rows photoelectric, bottom two rows total energy deposited) for different incident photon energies.

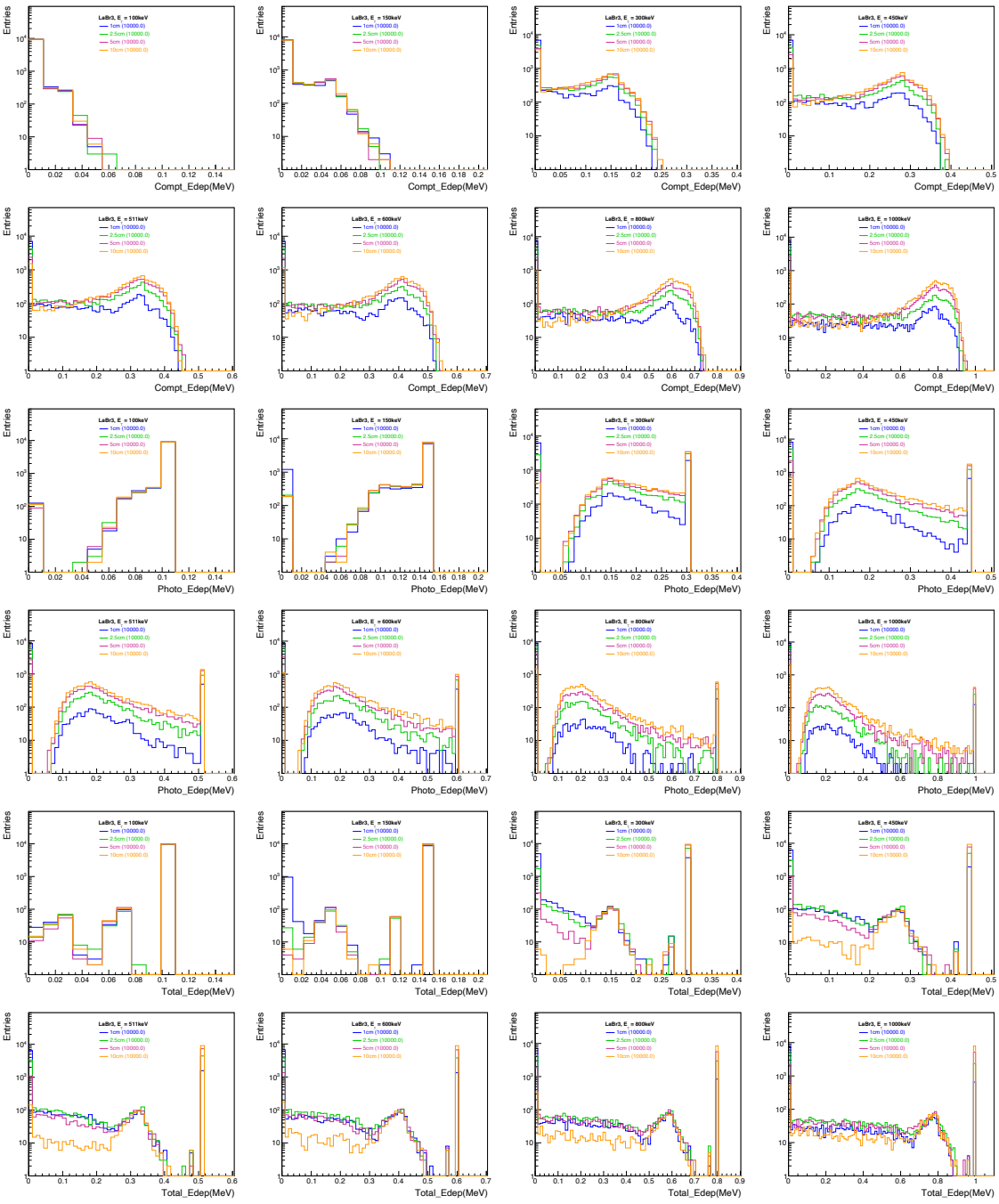

Figure A.5: Effect of material thickness in energy deposited in $LaBr_3$ via different processes (upper two rows Compton, middle two rows photoelectric, bottom two rows total energy deposited) for different incident photon energies.

A.2 Effect of incident photon energies in energy deposits

A.2.1 $PbWO_4$

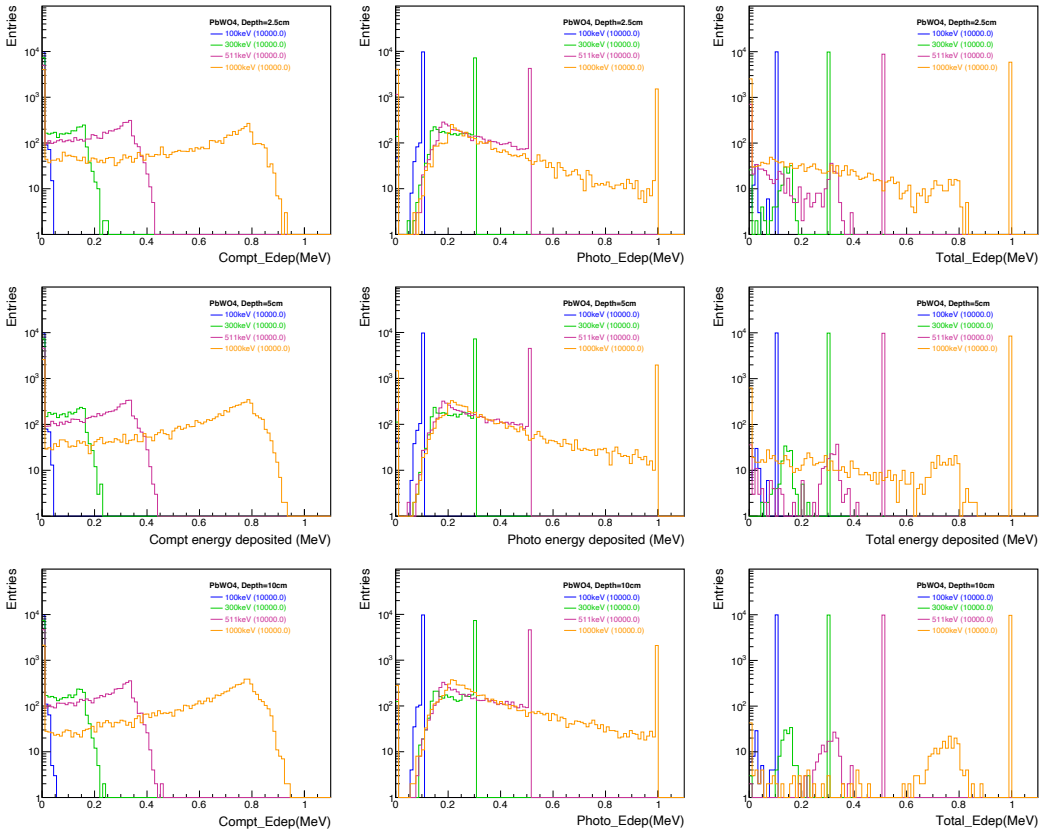

Figure A.6: Effect of incident photon energy in energy deposited via different processes (**left column:** Compton, **middle:** photoelectric, **right:** total energy deposited) in 3 different thicknesses of $PbWO_4$ (**upper row:** 2.5 cm, **middle row:** 5 cm, **bottom row:** 10 cm)

A.2.2 BGO

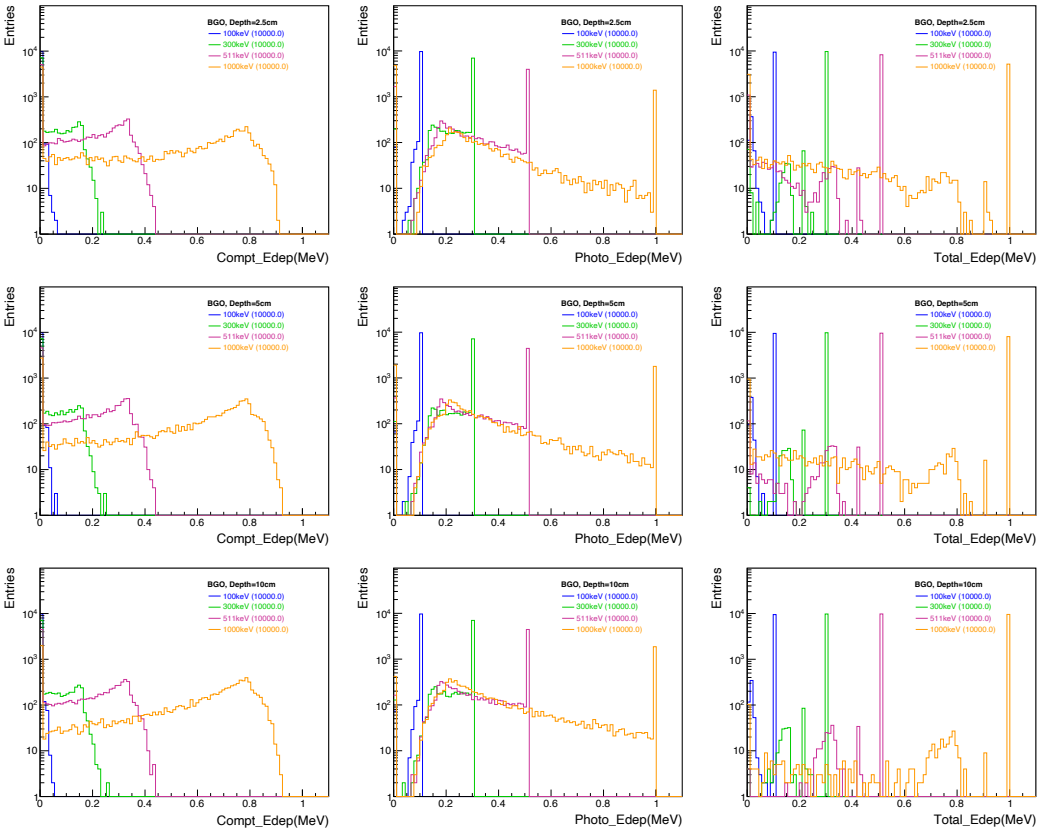

Figure A.7: Effect of incident photon energy in energy deposited via different processes (**left column:** Compton, **middle:** photoelectric, **right:** total energy deposited) in 3 different thicknesses of BGO (**upper row:** 2.5 cm, **middle row:** 5 cm, **bottom row:** 10 cm)

A.2.3 LYSO

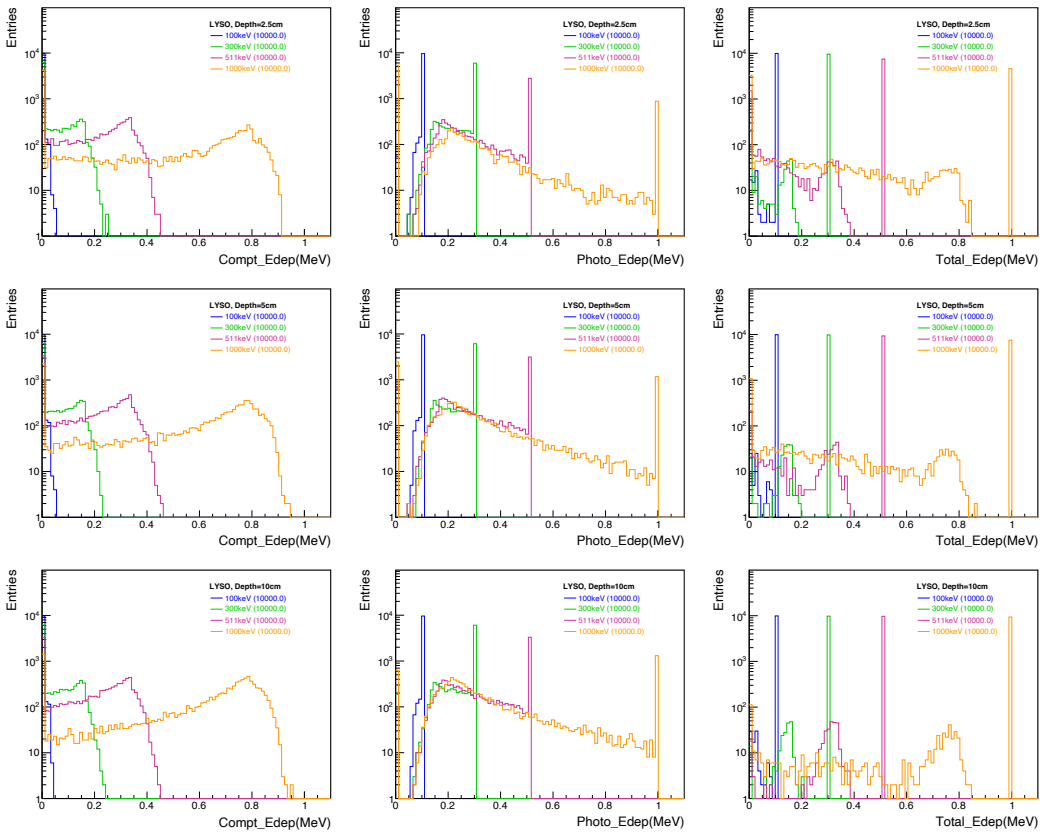

Figure A.8: Effect of incident photon energy in energy deposited via different processes (**left column:** Compton, **middle:** photoelectric, **right:** total energy deposited) in 3 different thicknesses of LYSO (**upper row:** 2.5 cm, **middle row:** 5 cm, **bottom row:** 10 cm)

A.2.4 GAGG

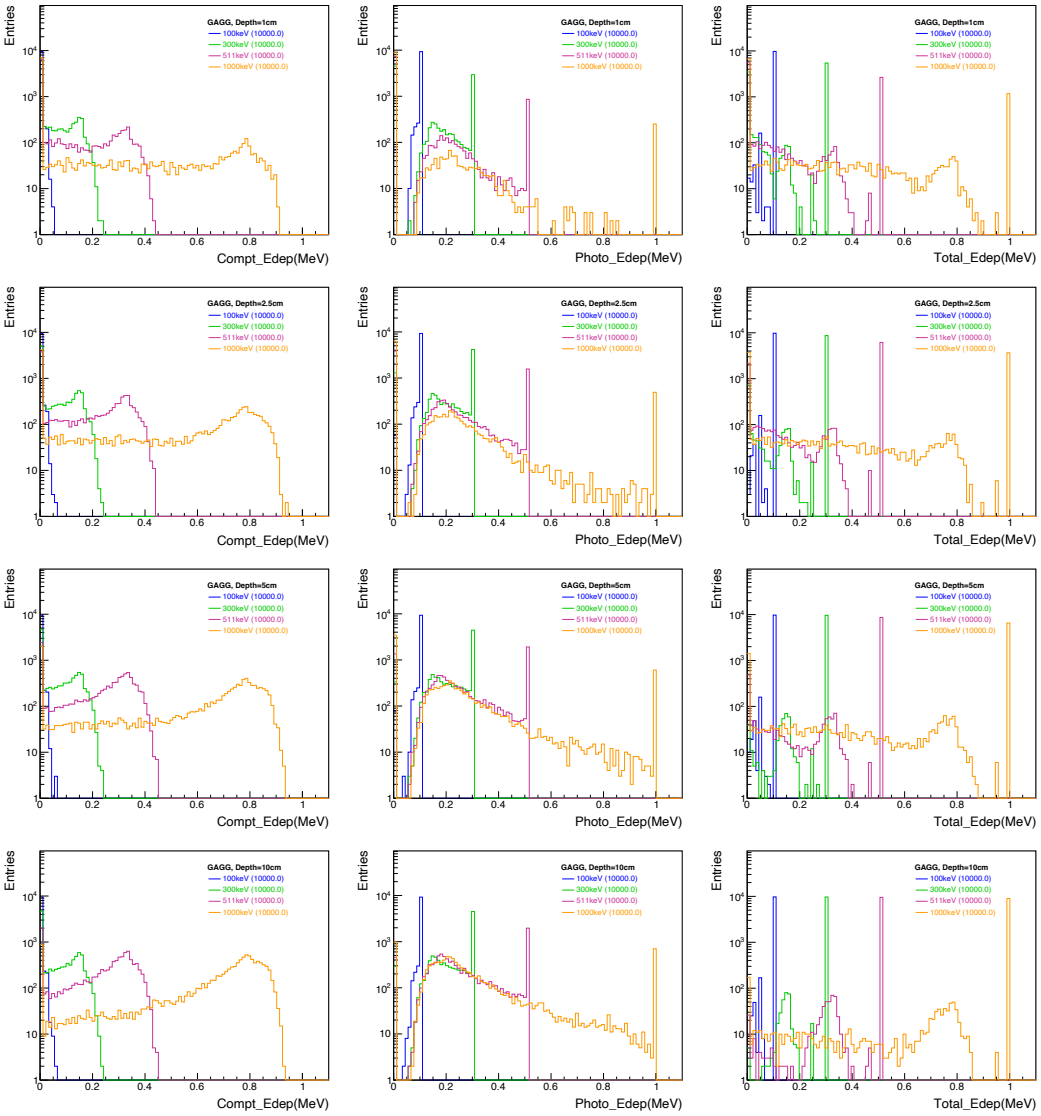

Figure A.9: Effect of incident photon energy in energy deposited via different processes (**left column:** Compton, **middle:** photoelectric, **right:** total energy deposited) in 4 different thicknesses of GAGG (1^{st} **row:** 1 cm, 2^{nd} **row:** 2.5 cm, 3^{rd} **row:** 5 cm, 4^{th} **row:** 10cm)

A.2.5 LaBr3

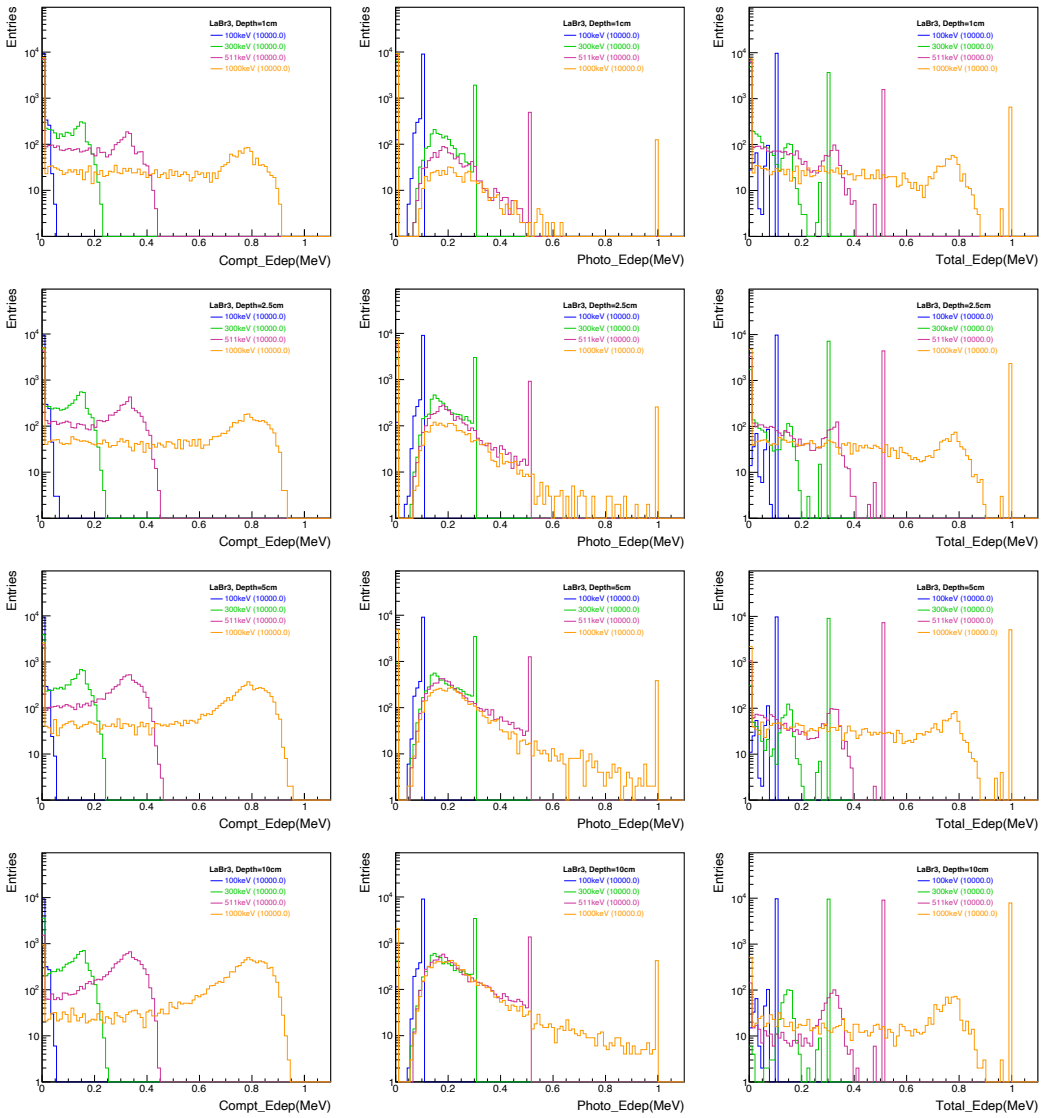

Figure A.10: Effect of incident photon energy in energy deposited via different processes (**left column:** Compton, **middle:** photoelectric, **right:** total energy deposited) in 4 different thicknesses of LaBr3 (1^{st} **row:** 1 cm, 2^{nd} **row:** 2.5 cm, 3^{rd} **row:** 5 cm, 4^{th} **row:** 10cm)

A.3 Energy deposited in different materials

A.3.1 At 2.5 cm thickness of materials

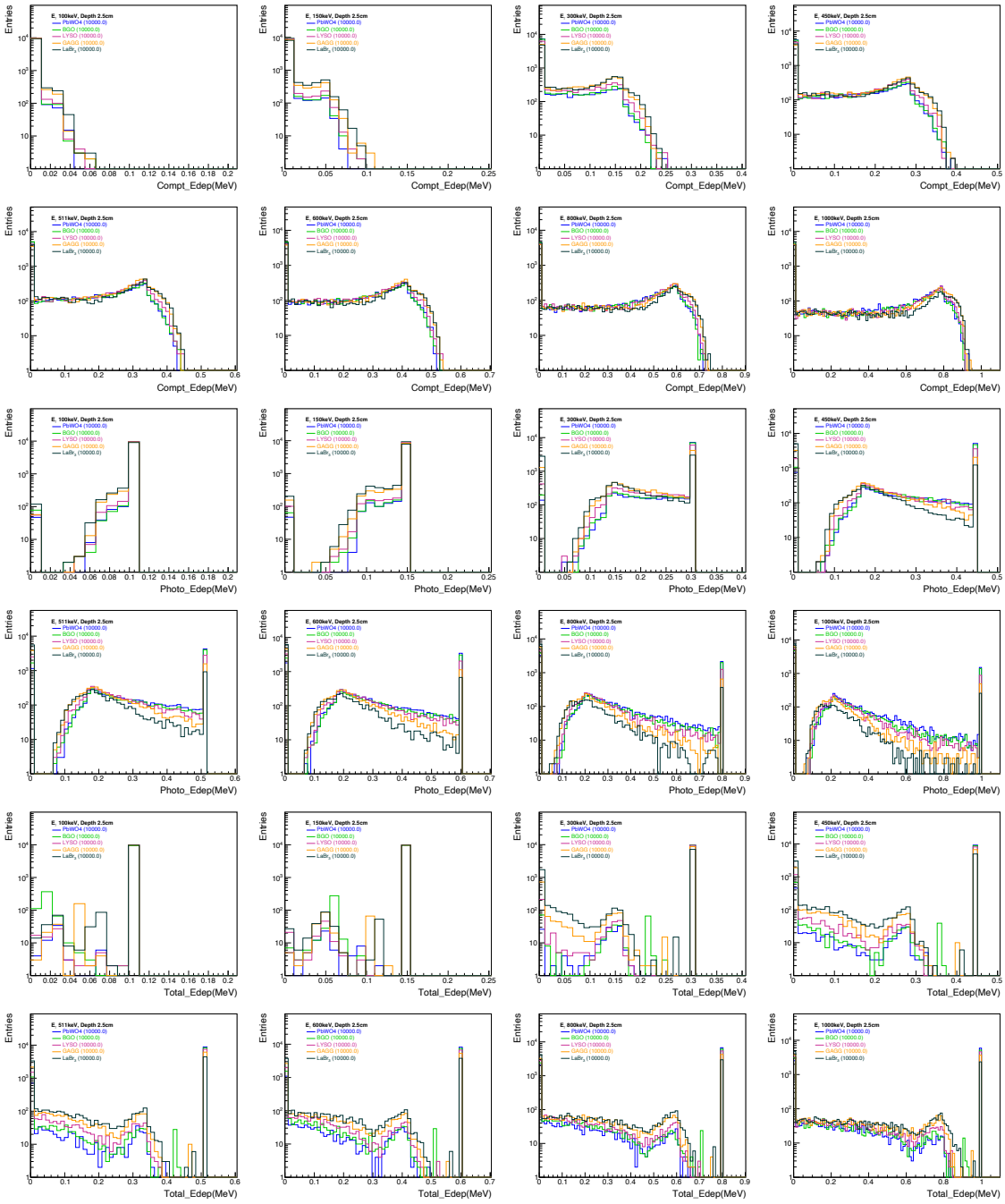

Figure A.11: Comparison of energy deposited in 2.5 cm thickness of different materials via different processes (upper two rows Compton, middle two rows photoelectric, bottom two rows total energy deposited) for different incident photon energies.

A.3.2 At 5 cm thickness of materials

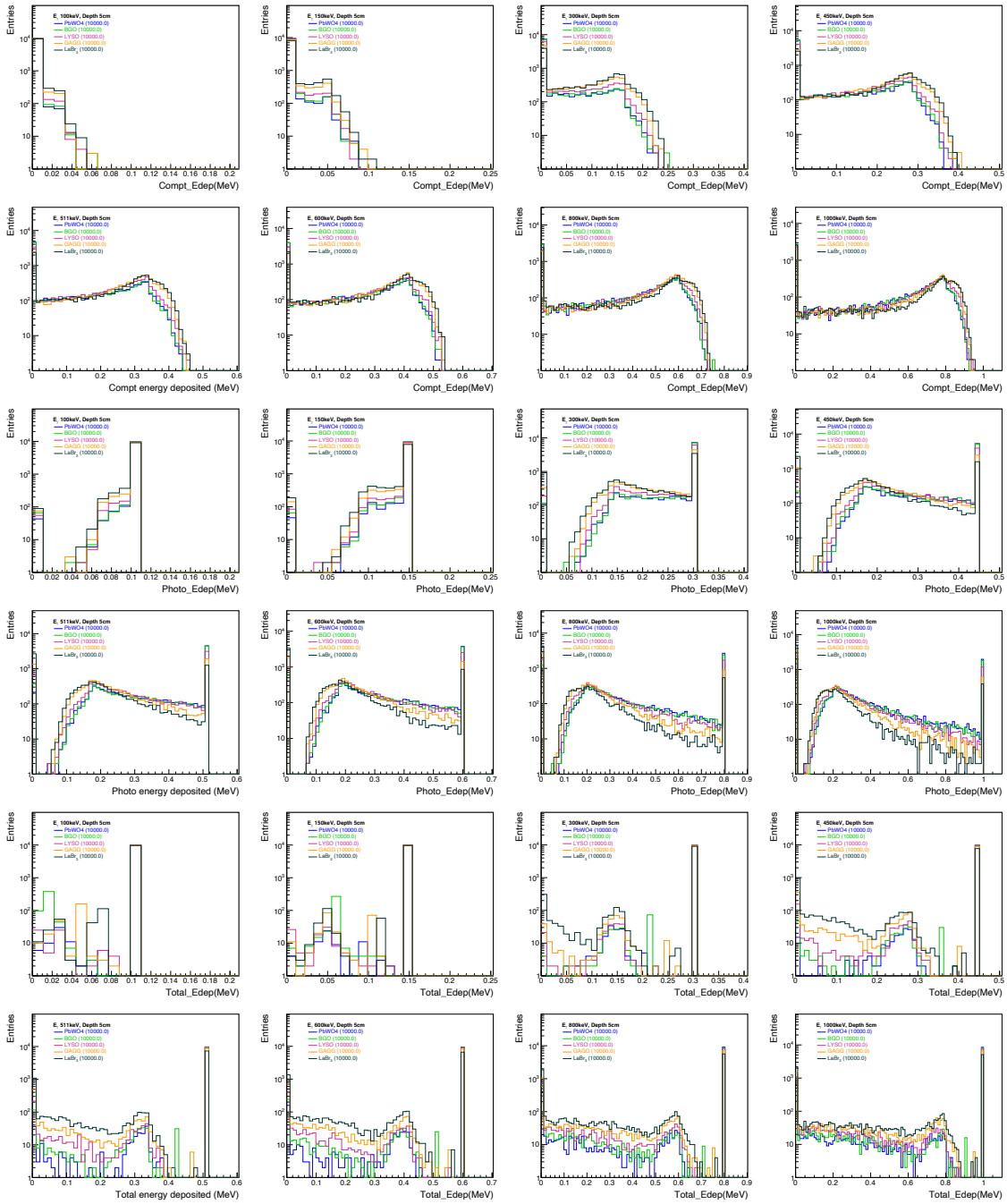

Figure A.12: Comparison of energy deposited in 5 cm thickness of different materials via different processes (upper two rows Compton, middle two rows photoelectric, bottom two rows total energy deposited) for different incident photon energies.

A.3.3 At 10 cm thickness of materials

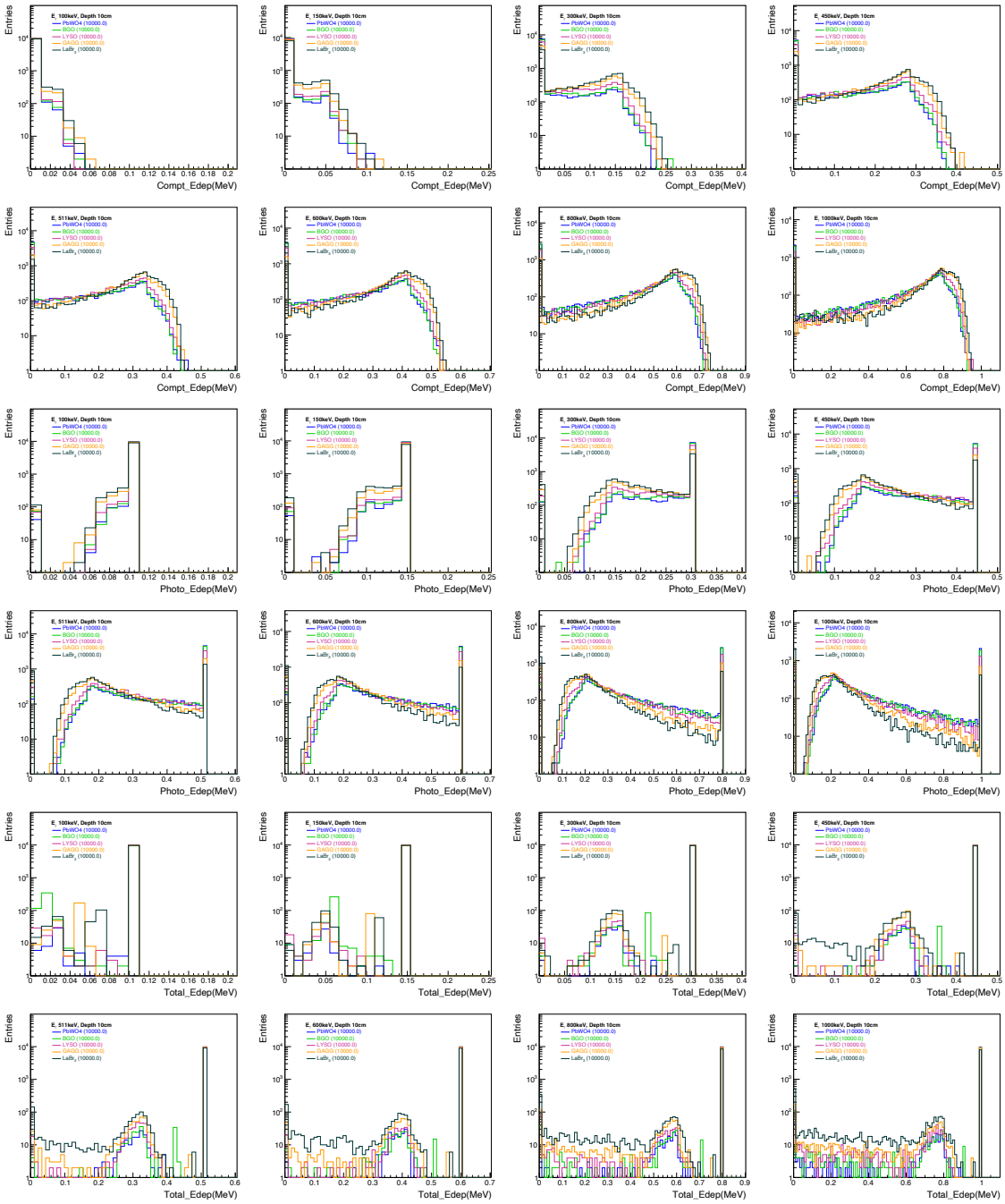

Figure A.13: Comparison of energy deposited in 10 cm thickness of different materials via different processes (upper two rows Compton, middle two rows photoelectric, bottom two rows total energy deposited) for different incident photon energies.

A.4 Effect of different parameters in the measured value of energy deposited ($E_{Measured}$)

A.4.1 Effect of material thickness

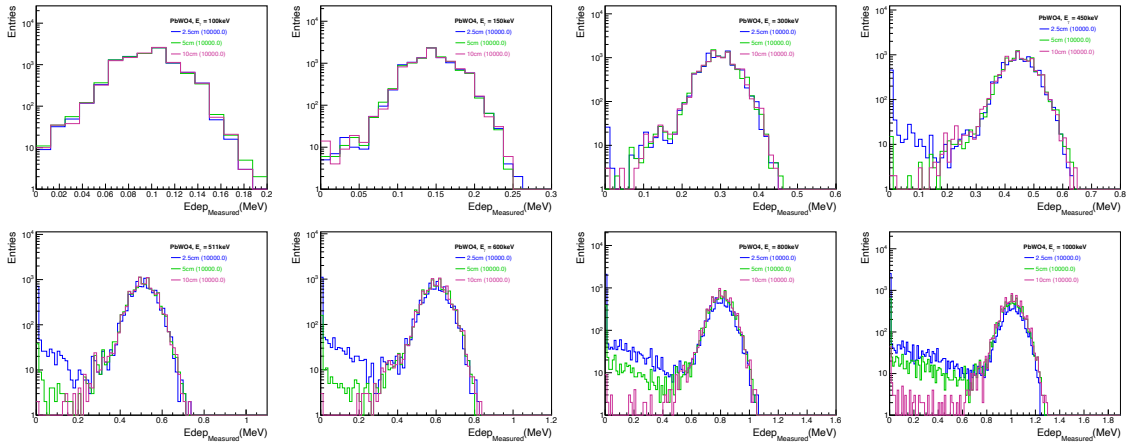

Figure A.14: Effect of material thickness in the measured value of energy deposited in $PbWO_4$

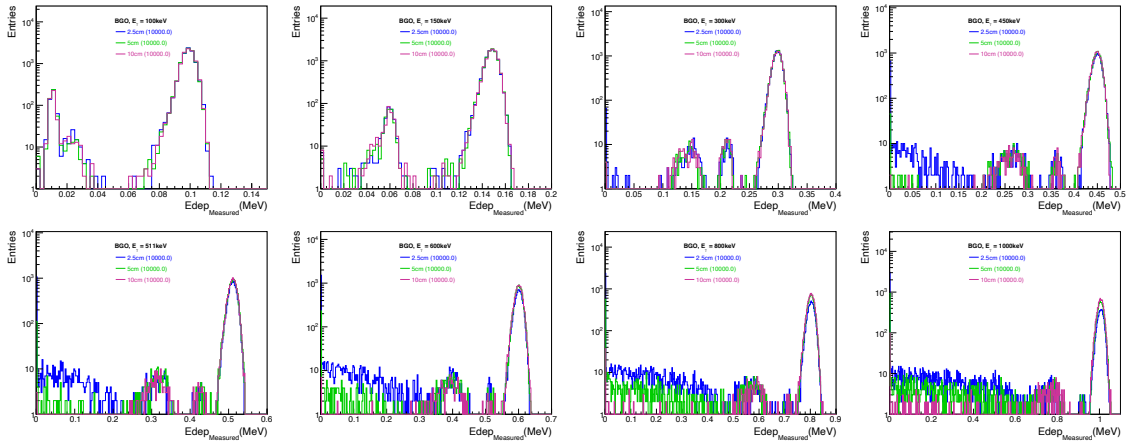

Figure A.15: Effect of material thickness in the measured value of energy deposited in BGO

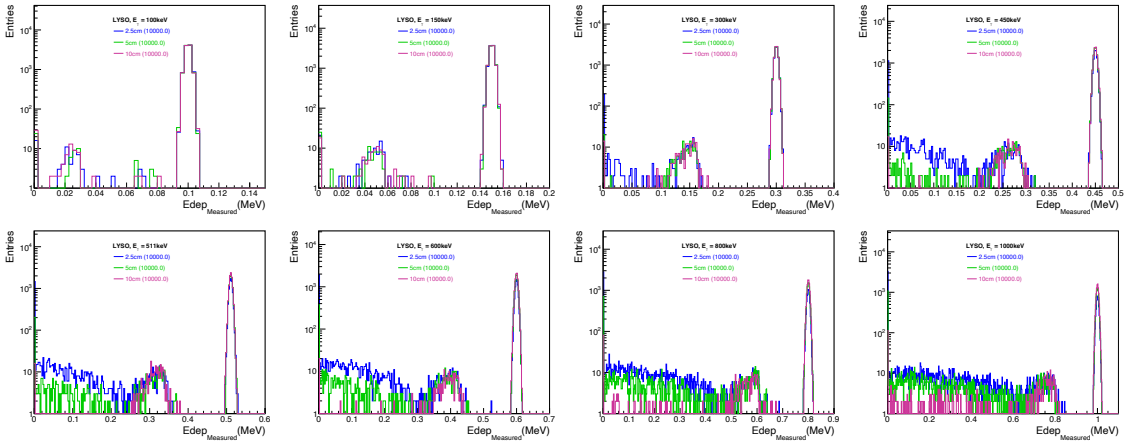

Figure A.16: Effect of material thickness in the measured value of energy deposited in LYSO

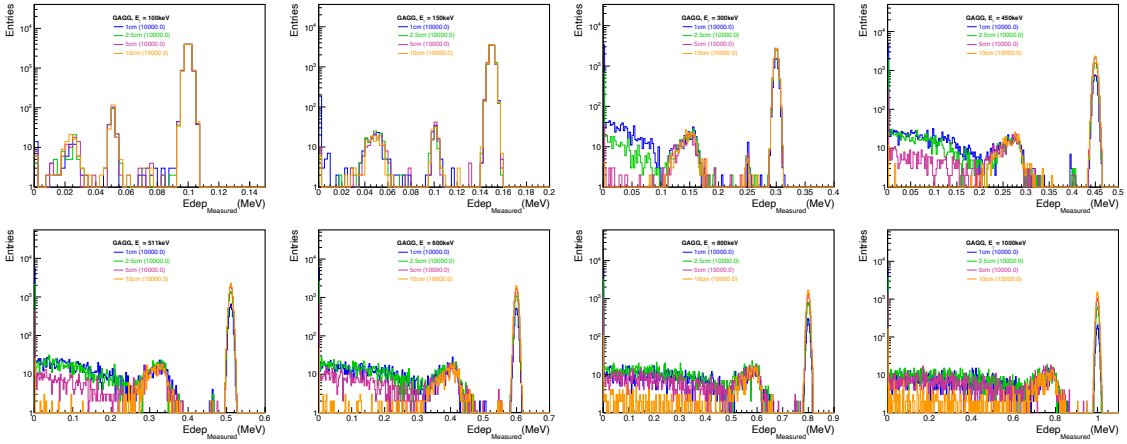

Figure A.17: Effect of material thickness in the measured value of energy deposited in GAGG

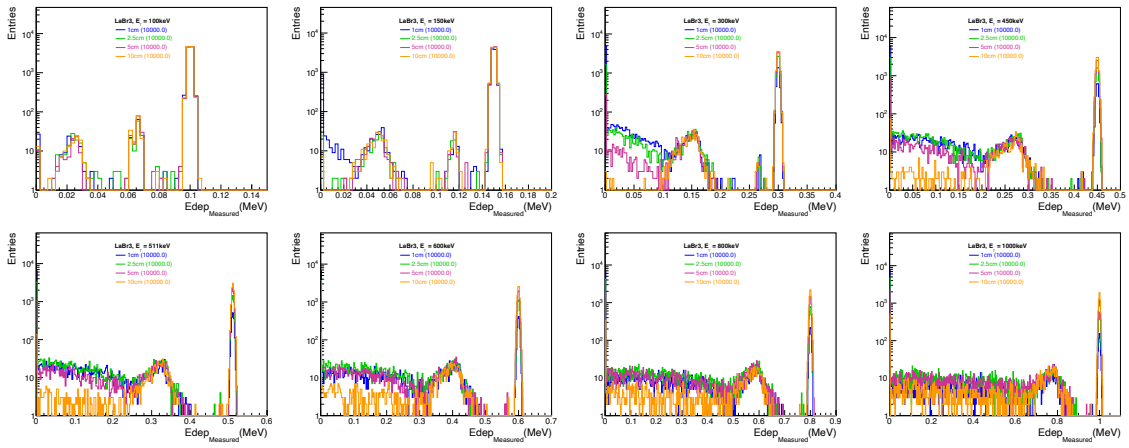

Figure A.18: Effect of material thickness in the measured value of energy deposited in $LaBr_3$

A.4.2 Effect of incident photon energies

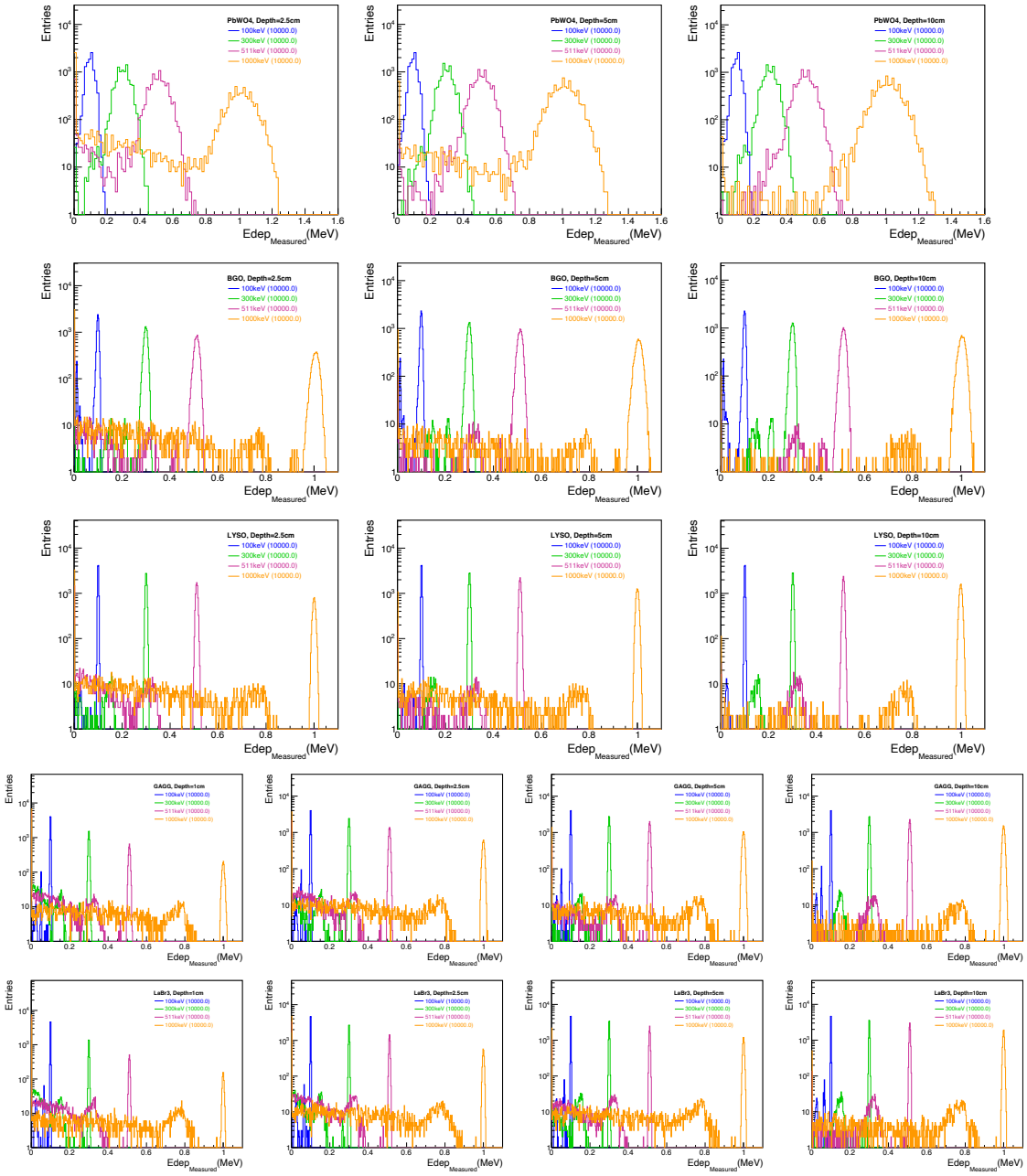

Figure A.19: Effect of energy of the incident photons on the measured value of the total energy deposited in different materials. **upper three rows:** $PbWO_4$, BGO, LYSO respectively with increasing thickness in a row from left to right (2.5 cm, 5 cm, 10 cm). **bottom two rows:** GAGG and $LaBr_3$ respectively with increasing thickness in a row from left to right (1cm, 2.5 cm, 5 cm, 10 cm).

A.5 Iterative fit plots of all the materials at different thickness for different incident photon Energies

Iterative fit plots of $PbWO_4$

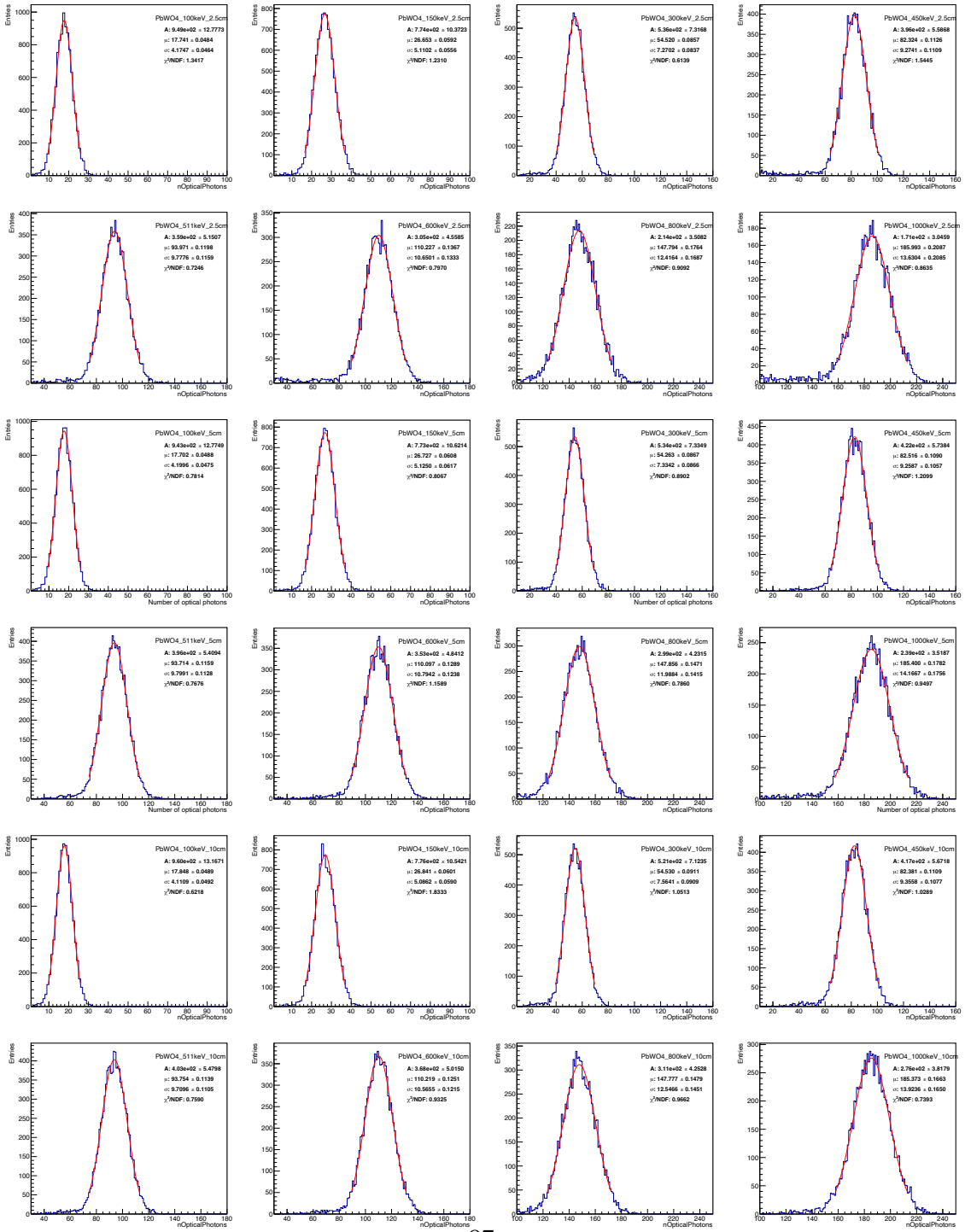

Figure A.20: Iterative fits of number of optical photon distribution in $PbWO_4$ for different thicknesses (upper two rows: 2.5 cm, middle two rows: 5 cm, bottom two rows: 10cm) for incident photon energies of 100 keV, 150 keV, 300 keV, 450 keV, 511 keV, 600 keV, 800 keV, 1000 keV (put in increasing order in a row.)

Iterative fit plots of BGO

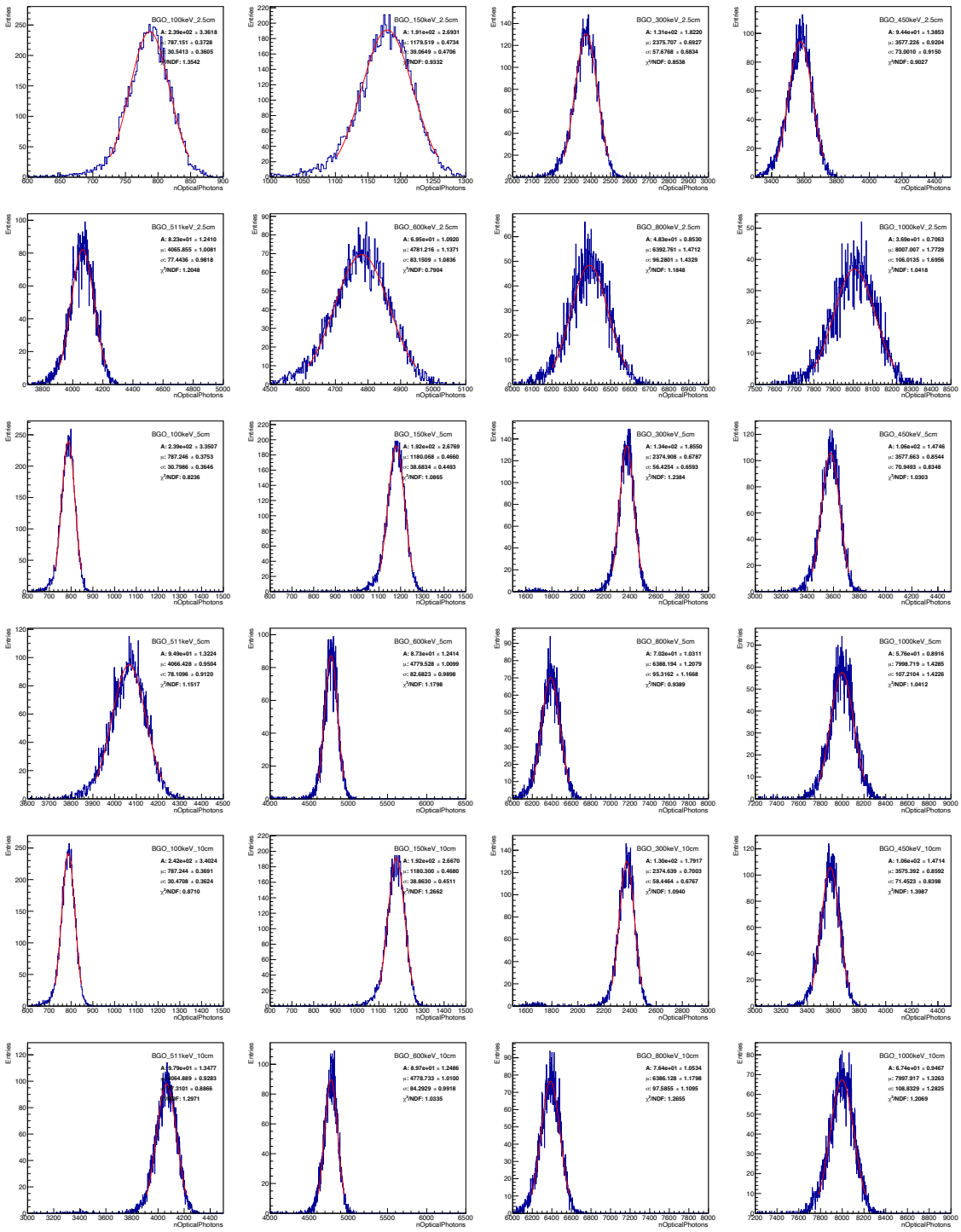

Figure A.21: Iterative fits of number of optical photon distribution in BGO for different thicknesses (Upper two rows: 2.5 cm, middle two rows: 5 cm, bottom two rows: 10cm) for incident photon energies of 100 keV, 150 keV, 300 keV, 450 keV, 511 keV, 600 keV, 800 keV, 1000 keV (put in increasing order in a row.)

Iterative fit plots of LYSO

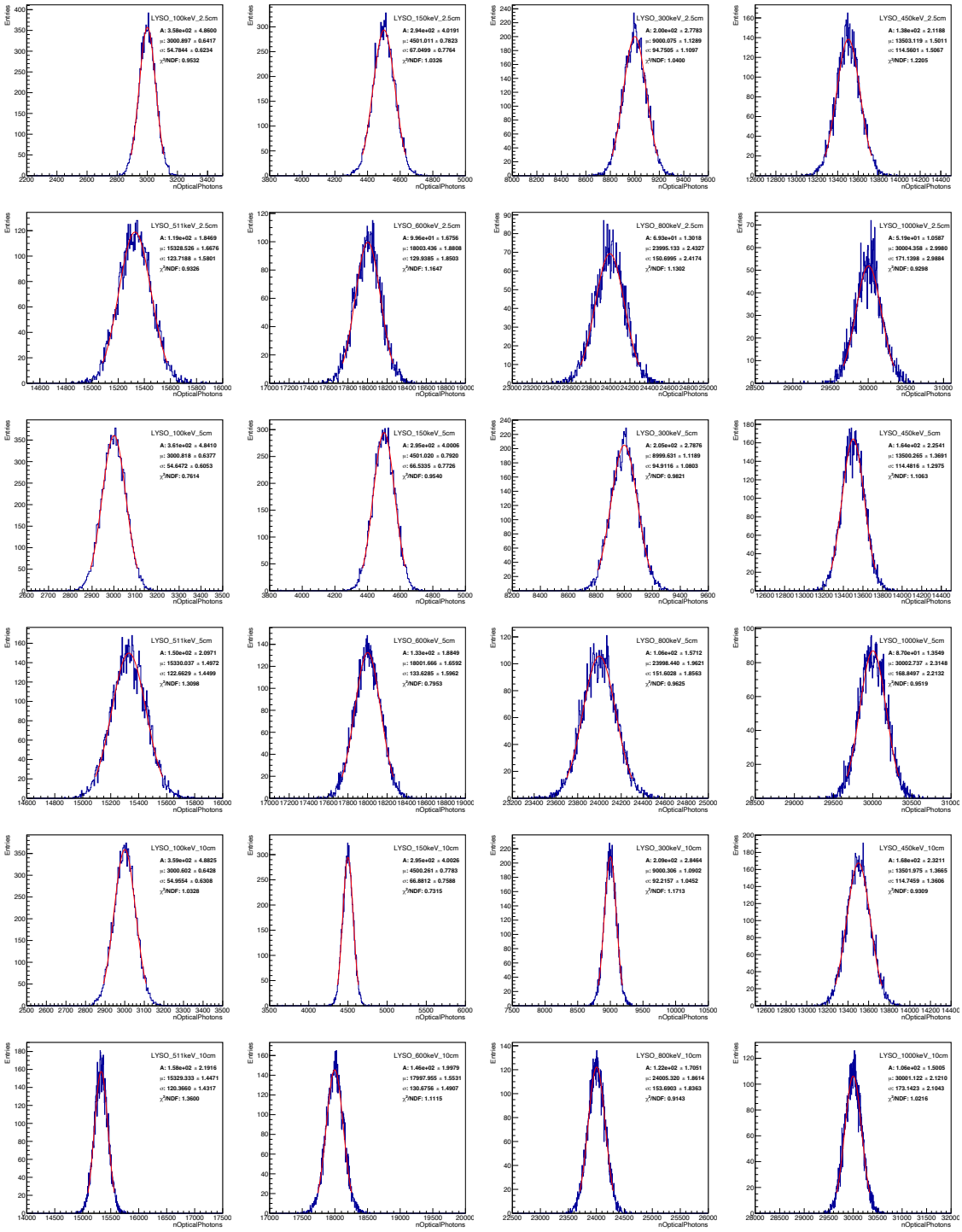

Figure A.22: Iterative fits of number of optical photon distribution in LYSO for different thicknesses (Upper two rows: 2.5 cm, middle two rows: 5 cm, bottom two rows: 10cm) for incident photon energies of 100 keV, 150 keV, 300 keV, 450 keV, 511 keV, 600 keV, 800 keV, 1000 keV (put in increasing order in a row.)

Iterative fit plots of GAGG

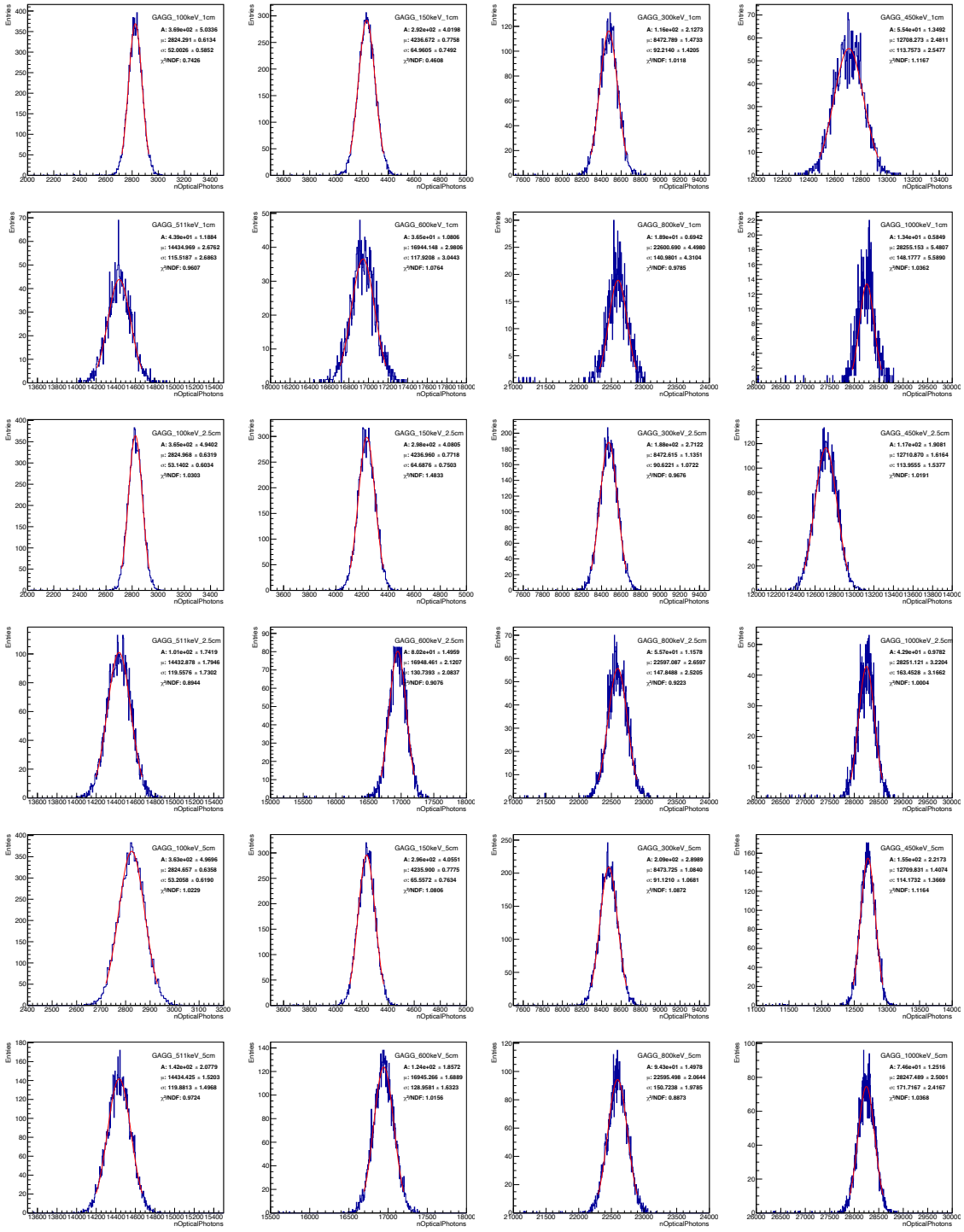

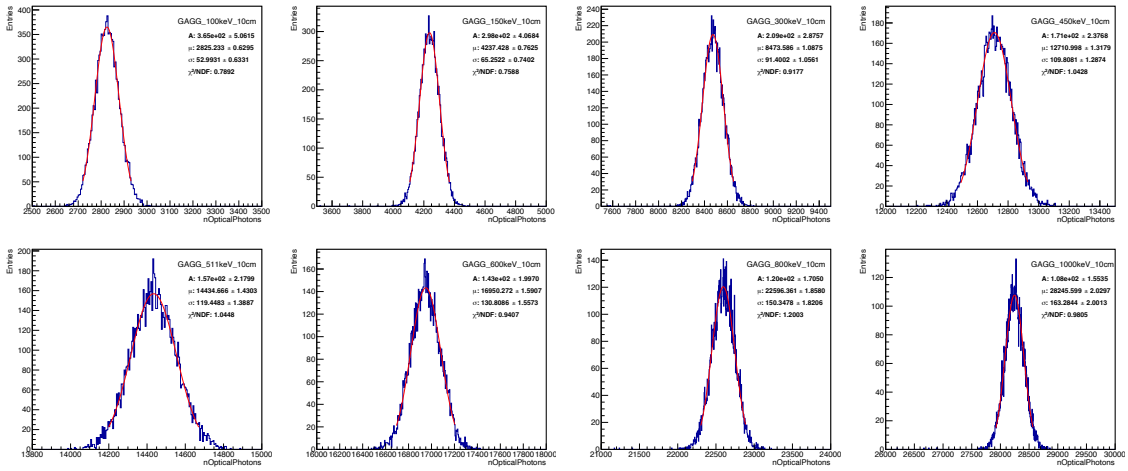

Figure A.24: Iterative fits of number of optical photon distribution in GAGG for different thicknesses (**first two rows:** 1 cm, 3^{rd} **and** 4^{th} **rows:** 2.5 cm, 5^{th} **and** 6^{th} **rows:** 5 cm, **last two rows:** 10cm) for incident photon energies of 100 keV, 150 keV, 300 keV, 450 keV, 511 keV, 600 keV, 800 keV, 1000 keV (put in increasing order in a row.)

Iterative fit plots of $LaBr_3$

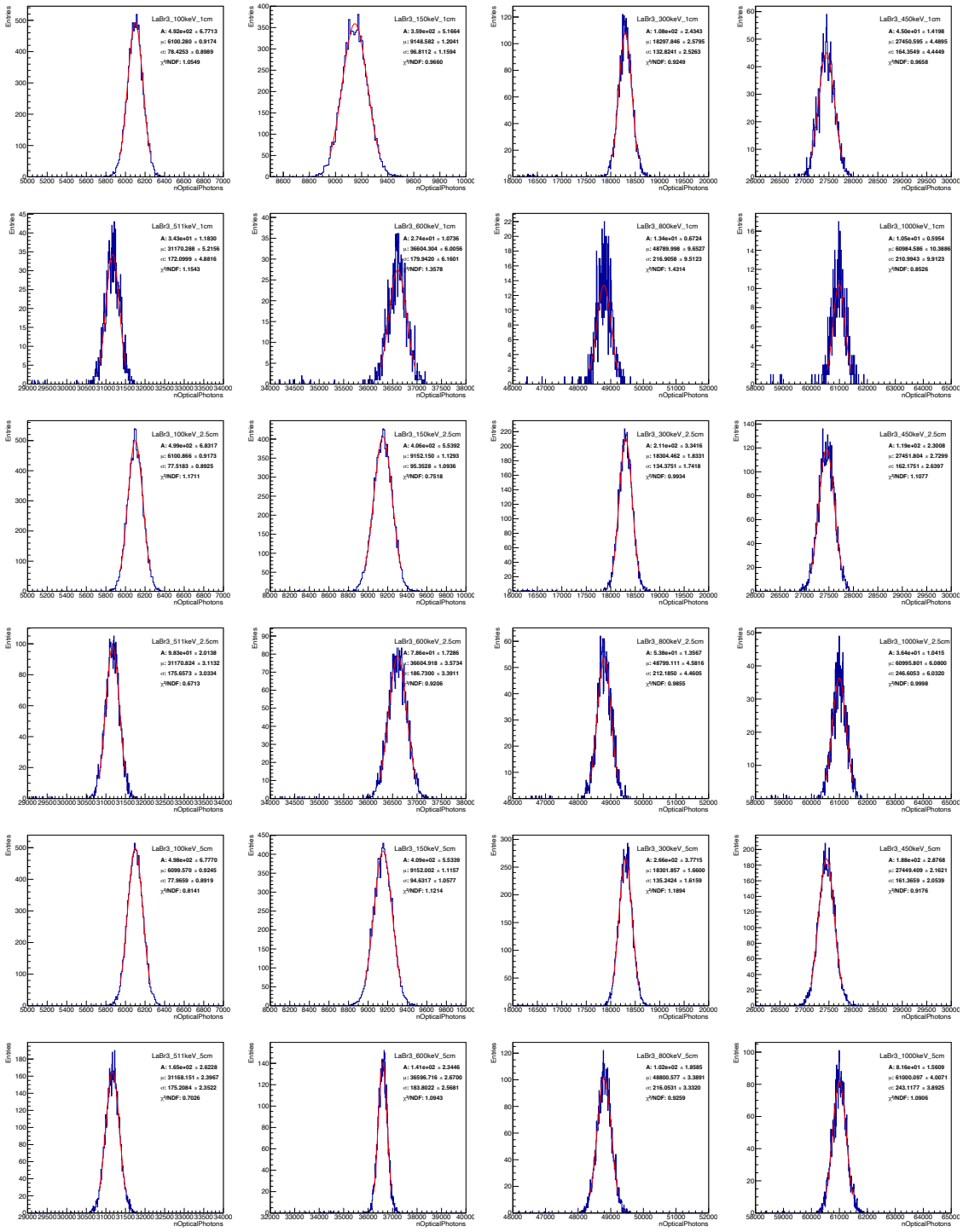

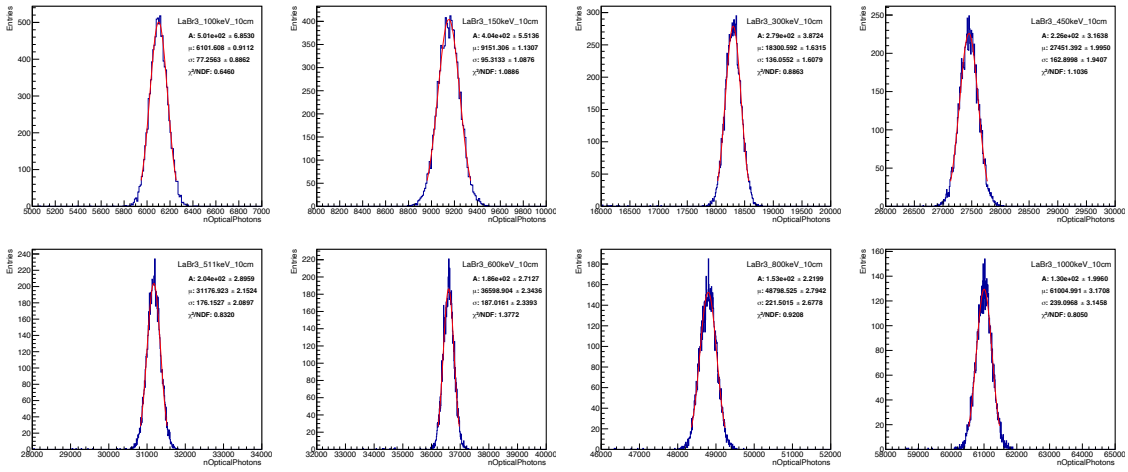

Figure A.26: Iterative fits of number of optical photon distribution in $LaBr_3$ for different thicknesses (**first two rows:** 1 cm, 3^{rd} **and** 4^{th} **rows:** 2.5 cm, 5^{th} **and** 6^{th} **rows:** 5 cm, **last two rows:** 10cm) for incident photon energies of 100 keV, 150 keV, 300 keV, 450 keV, 511 keV, 600 keV, 800 keV, 1000 keV (put in increasing order in a row.)

A.6 Effect of different factors on distribution of number of optical photons (nOpticalPhotons)

Effect of material thickness

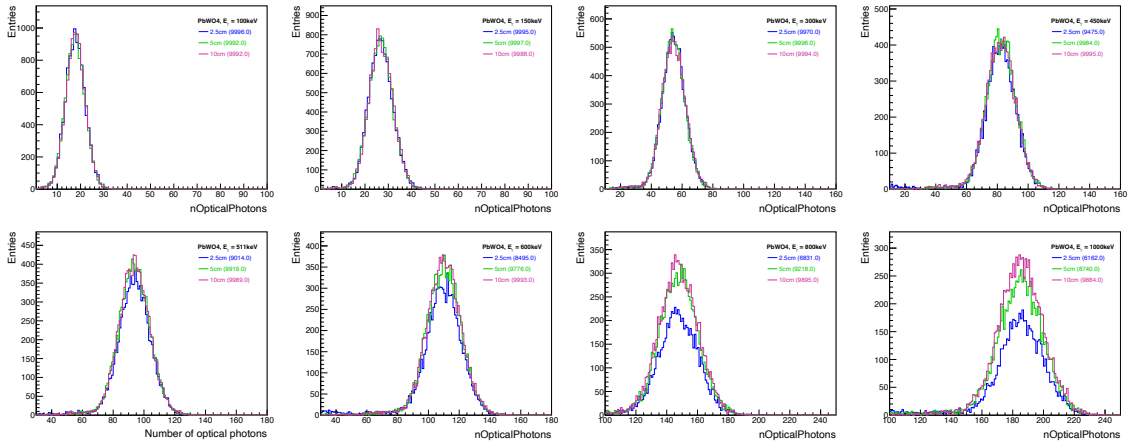

Figure A.27: Distribution of number of optical photons produced in $PbWO_4$ at different incident photons energies: 100 keV, 150 keV, 300 keV, 450 keV, 511 keV, 600 keV, 800 keV, 1000 keV (put in the ascending order in a row)

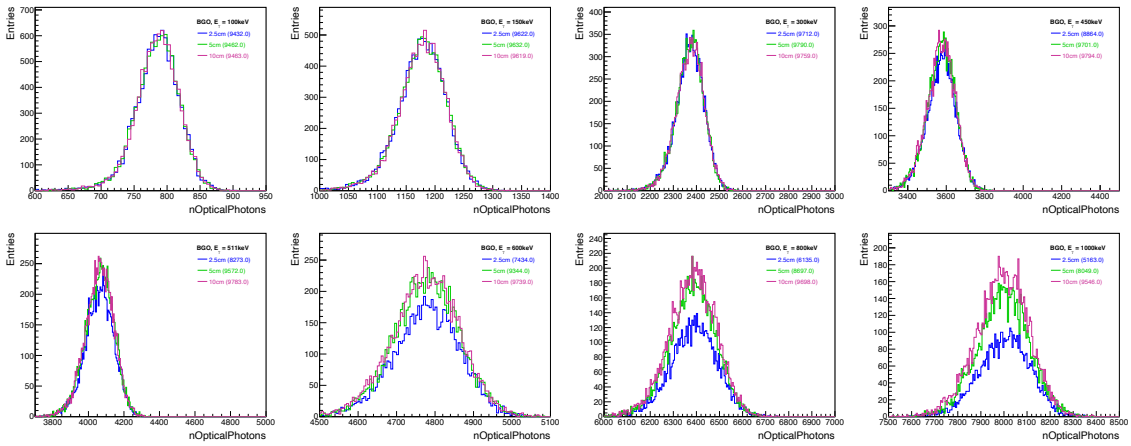

Figure A.28: Distribution of number of optical photons produced in BGO at different incident photons energies: 100 keV, 150 keV, 300 keV, 450 keV, 511 keV, 600 keV, 800 keV, 1000 keV (put in the ascending order in a row)

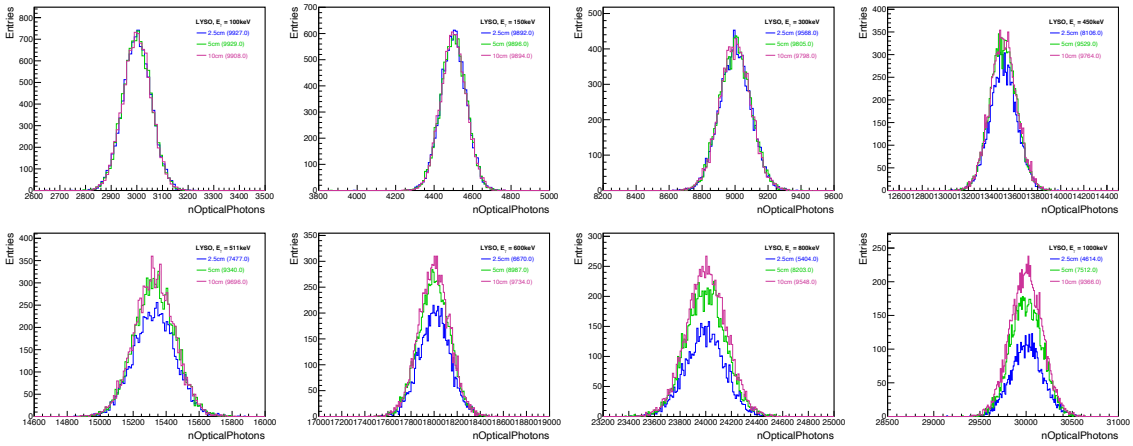

Figure A.29: Distribution of number of optical photons produced in LYSO at different incident photons energies: 100 keV, 150 keV, 300 keV, 450 keV, 511 keV, 600 keV, 800 keV, 1000 keV (put in the ascending order in a row)

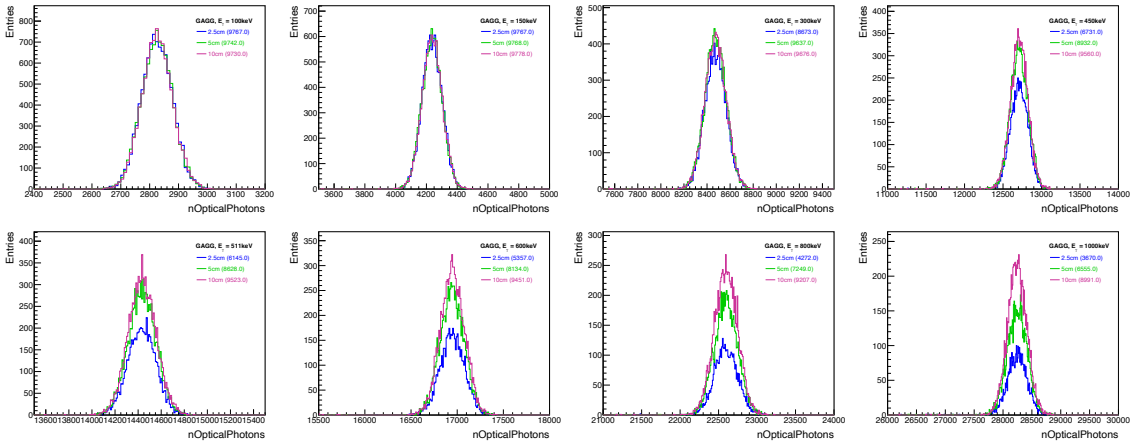

Figure A.30: Distribution of number of optical photons produced in GAGG at different incident photons energies: 100 keV, 150 keV, 300 keV, 450 keV, 511 keV, 600 keV, 800 keV, 1000 keV (put in the ascending order in a row)

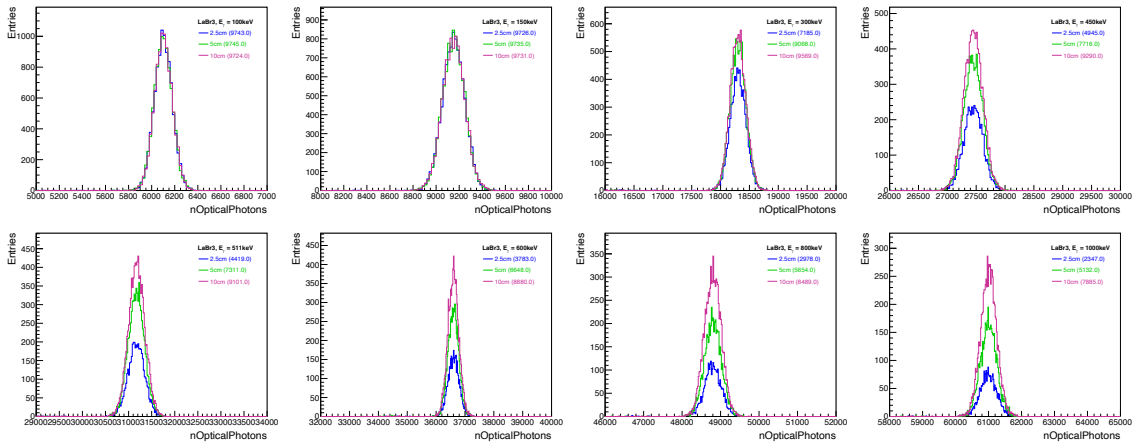

Figure A.31: Distribution of number of optical photons produced in $LaBr_3$ at different incident photons energies: 100 keV, 150 keV, 300 keV, 450 keV, 511 keV, 600 keV, 800 keV, 1000 keV (put in the ascending order in a row)

Effect of incident photon energy

$PbWO_4$

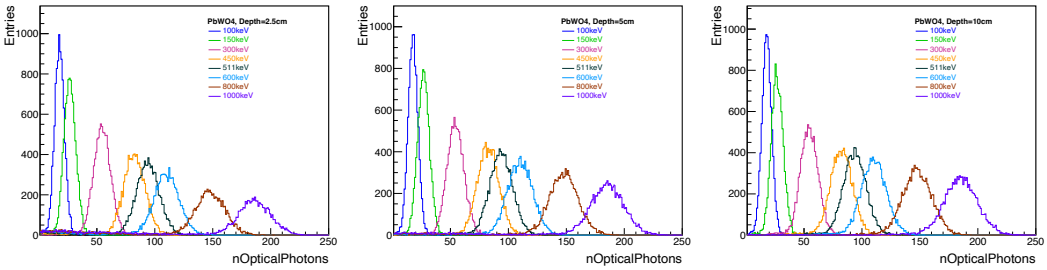

BGO

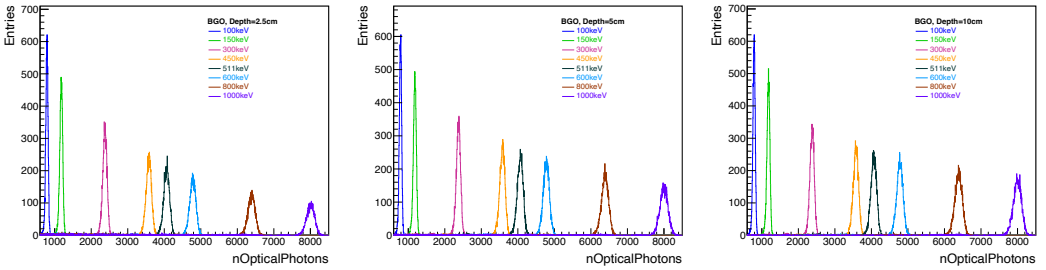

LYSO

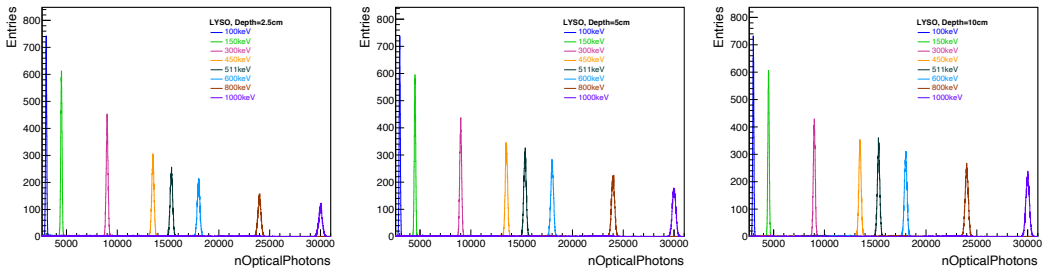

GAGG

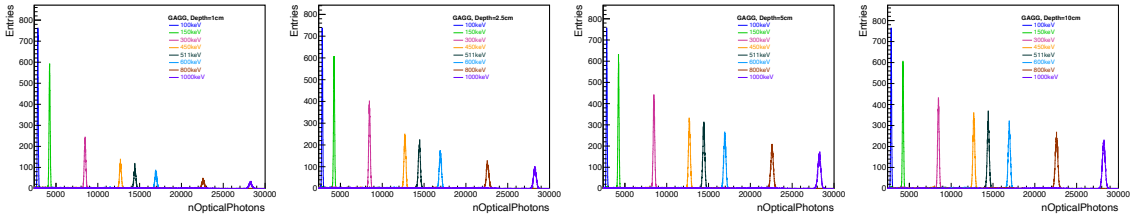

$LaBr_3$

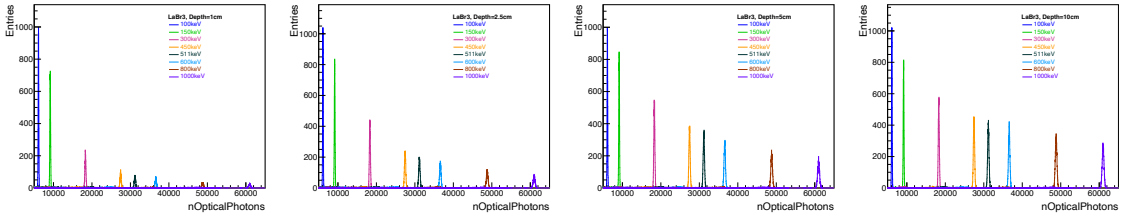

Figure A.36: Figure showing the effect of incident photon energy on the distribution of number of optical photons

A.7 $E_{Measured}$, detector response, resolution, efficiencies for different thicknesses of different materials

Plots for BGO

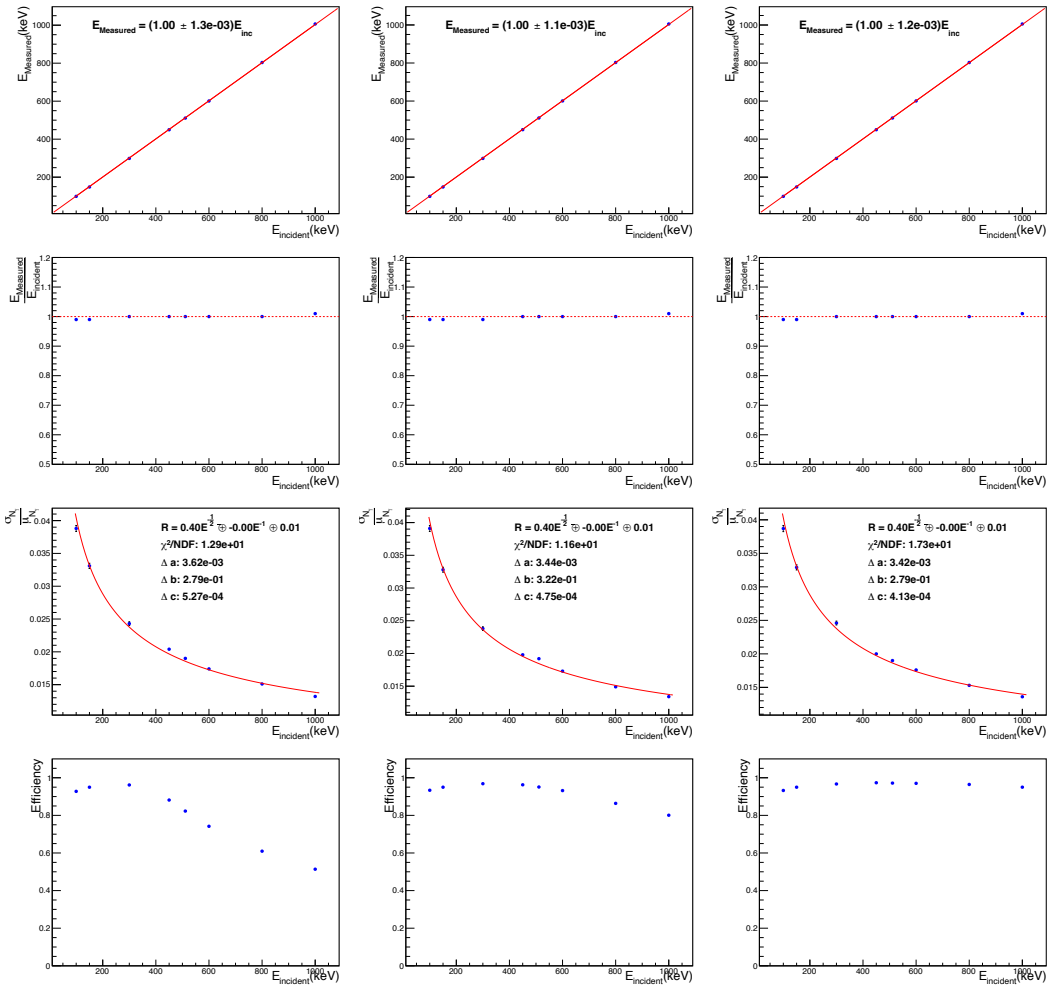

Figure A.37: Results from fitting for different thicknesses of BGO (2.5cm, 5cm, 10cm thickness respectively in a row)

Plots for LYSO

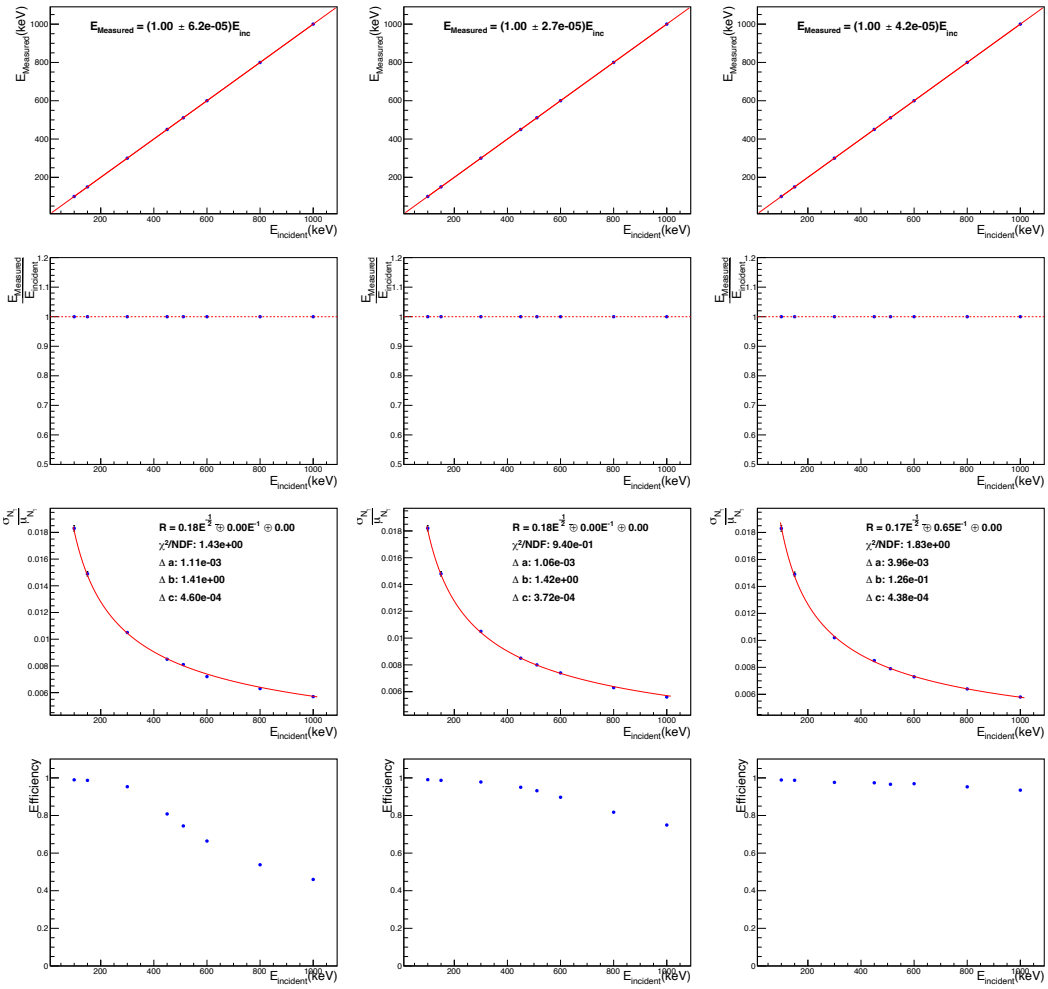

Figure A.38: Results from fitting for different thicknesses of LYSO (2.5cm, 5cm, 10cm thickness respectively in a row)

Plots for GAGG

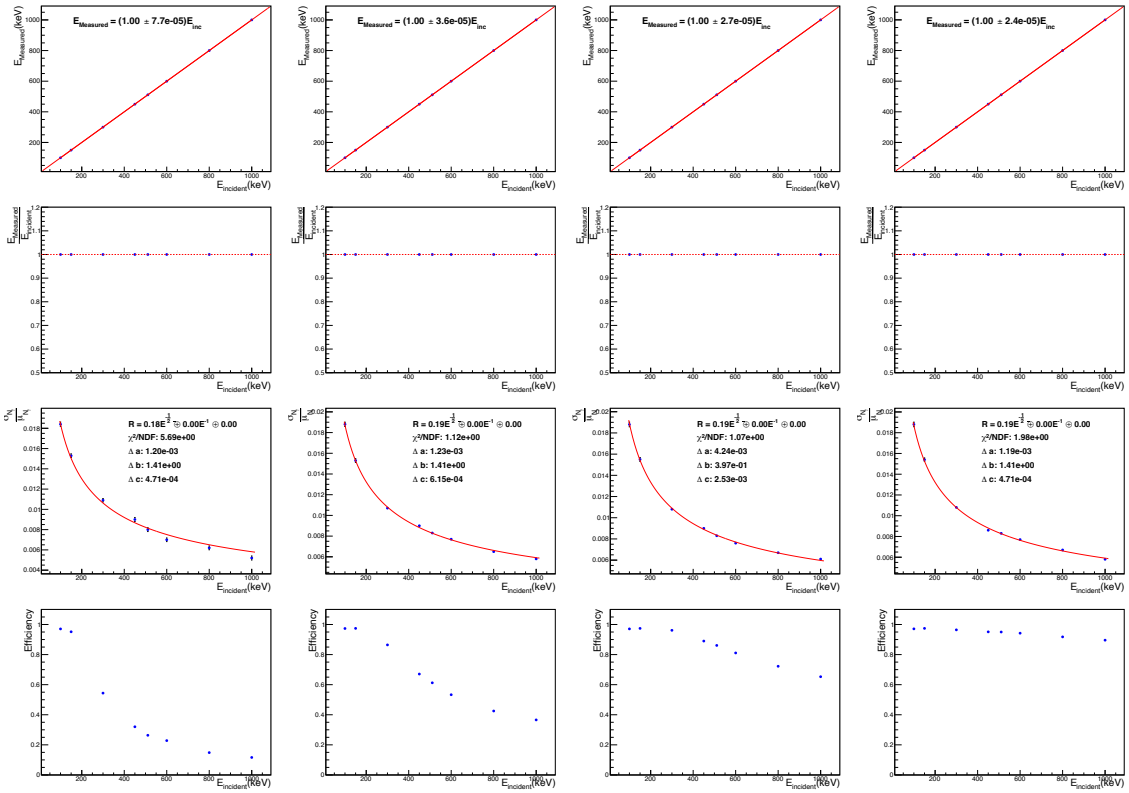

Figure A.39: Results from fitting for different thicknesses of GAGG (1cm, 2.5cm, 5cm, 10cm thickness respectively in a row)

Plots for $LaBr_3$

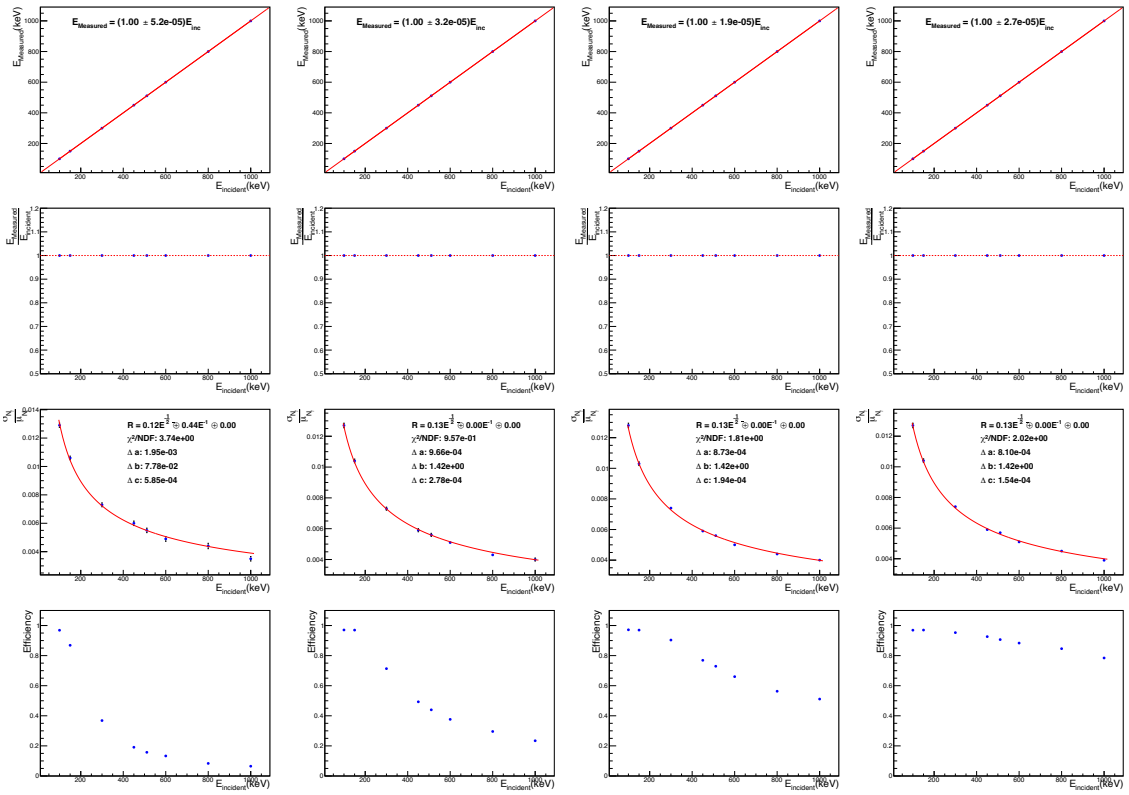

Figure A.40: Results from fitting for different thicknesses of $LaBr_3$ (1cm, 2.5cm, 5cm, 10cm thickness respectively in a row)

A.8 Effect of material thickness on resolution & efficiency

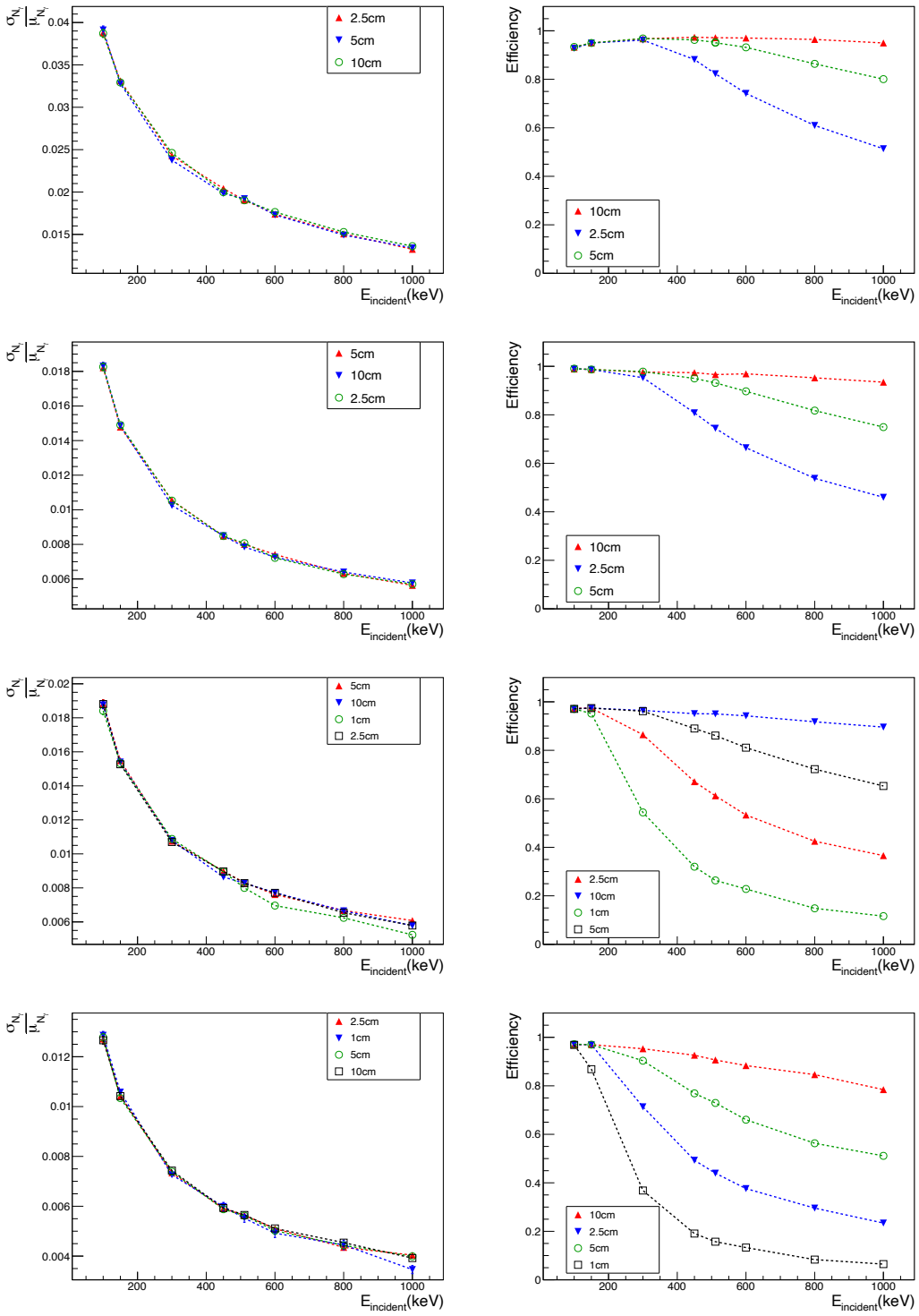

Figure A.41: Comparing effects of material thickness in energy resolution (left column) and efficiencies (right column) of BGO (first row), LYSO (second row), GAGG (third row) and $LaBr_3$ (fourth row)

A.9 Energy resolution & efficiencies in different materials and material thicknesses for 20cm $\times$ 20cm transverse cross section

Einc	Resolution		
(keV)	2.5cm	5cm	10cm
100	0.2353	0.2372	0.2303
150	0.1917	0.1918	0.1895
300	0.1333	0.1352	0.1387
450	0.1127	0.1122	0.1136
511	0.104	0.1046	0.1036
600	0.0966	0.098	0.0959
800	0.084	0.0811	0.0849
1000	0.0733	0.0764	0.0751

Einc	Efficiency		
(keV)	2.5cm	5cm	10cm
100	0.995	0.9939	0.9944
150	0.9931	0.9939	0.9929
300	0.9837	0.986	0.9874
450	0.9248	0.9842	0.9837
511	0.8848	0.9776	0.9837
600	0.8199	0.962	0.9824
800	0.6766	0.9132	0.9834
1000	0.5942	0.856	0.976

Table A.1: Table for energy resolution and efficiency of $PbWO_4$

Einc	Resolution		
(keV)	2.5cm	5cm	10cm
100	0.0388	0.0391	0.0387
150	0.0331	0.0328	0.0329
300	0.0243	0.0238	0.0246
450	0.0204	0.0198	0.02
511	0.019	0.0192	0.019
600	0.0174	0.0173	0.0176
800	0.0151	0.0149	0.0153
1000	0.0132	0.0134	0.0136

Einc	Efficiency		
(keV)	2.5cm	5cm	10cm
100	0.9277	0.9335	0.9324
150	0.9497	0.9498	0.9498
300	0.9617	0.9684	0.9669
450	0.8815	0.9626	0.9735
511	0.8228	0.9508	0.9716
600	0.7419	0.9318	0.9703
800	0.6096	0.8638	0.9644
1000	0.5137	0.8007	0.9499

Table A.2: Table for energy resolution and efficiency of BGO

Einc	Resolution		
(keV)	2.5cm	5cm	10cm
100	0.0183	0.0182	0.0183
150	0.0149	0.0148	0.0149
300	0.0105	0.0105	0.0102
450	0.0085	0.0085	0.0085
511	0.0081	0.008	0.0079
600	0.0072	0.0074	0.0073
800	0.0063	0.0063	0.0064
1000	0.0057	0.0056	0.0058

Einc	Efficiency		
(keV)	2.5cm	5cm	10cm
100	0.9897	0.9905	0.9888
150	0.9867	0.9868	0.9872
300	0.9532	0.9781	0.976
450	0.8082	0.9501	0.9739
511	0.7445	0.9317	0.9659
600	0.6642	0.8969	0.969
800	0.538	0.8174	0.9525
1000	0.4598	0.7493	0.9346

Table A.3: Table for energy resolution and efficiency of LYSO

Einc	Resolution			
(keV)	1cm	2.5cm	5cm	10cm
100	0.0184	0.0188	0.0188	0.0188
150	0.0153	0.0153	0.0155	0.0154
300	0.0109	0.0107	0.0108	0.0108
450	0.009	0.009	0.009	0.0086
511	0.008	0.0083	0.0083	0.0083
600	0.007	0.0077	0.0076	0.0077
800	0.0062	0.0065	0.0067	0.0067
1000	0.0052	0.0058	0.0061	0.0058

Einc	Efficiency			
(keV)	1cm	2.5cm	5cm	10cm
100	0.9706	0.9734	0.9708	0.9711
150	0.9516	0.9742	0.9741	0.9742
300	0.5439	0.8644	0.9613	0.9644
450	0.3201	0.6707	0.8899	0.9511
511	0.2635	0.6124	0.8609	0.9501
600	0.2282	0.5332	0.8109	0.9422
800	0.1484	0.425	0.7223	0.9177
1000	0.1162	0.3658	0.6529	0.8957

Table A.4: Table for energy resolution and efficiency of GAGG

Einc	Resolution			
(keV)	1cm	2.5cm	5cm	10cm
100	0.0129	0.0127	0.0128	0.0127
150	0.0106	0.0104	0.0103	0.0104
300	0.0073	0.0073	0.0074	0.0074
450	0.006	0.0059	0.0059	0.0059
511	0.0055	0.0056	0.0056	0.0057
600	0.0049	0.0051	0.005	0.0051
800	0.0044	0.0043	0.0044	0.0045
1000	0.0035	0.004	0.004	0.0039

Einc	Efficiency			
(keV)	1cm	2.5cm	5cm	10cm
100	0.9686	0.9705	0.9716	0.9691
150	0.8686	0.9696	0.9697	0.9699
300	0.3683	0.7134	0.9035	0.9528
450	0.1908	0.493	0.7689	0.9262
511	0.1572	0.4397	0.7293	0.9065
600	0.133	0.3762	0.6602	0.8834
800	0.0834	0.2957	0.5631	0.8461
1000	0.0648	0.2341	0.5112	0.7843

Table A.5: Table for energy resolution and efficiency of $LaBr_3$

A.10 Effect of transverse size of the material on energy resolution and efficiency

For $PbWO_4$

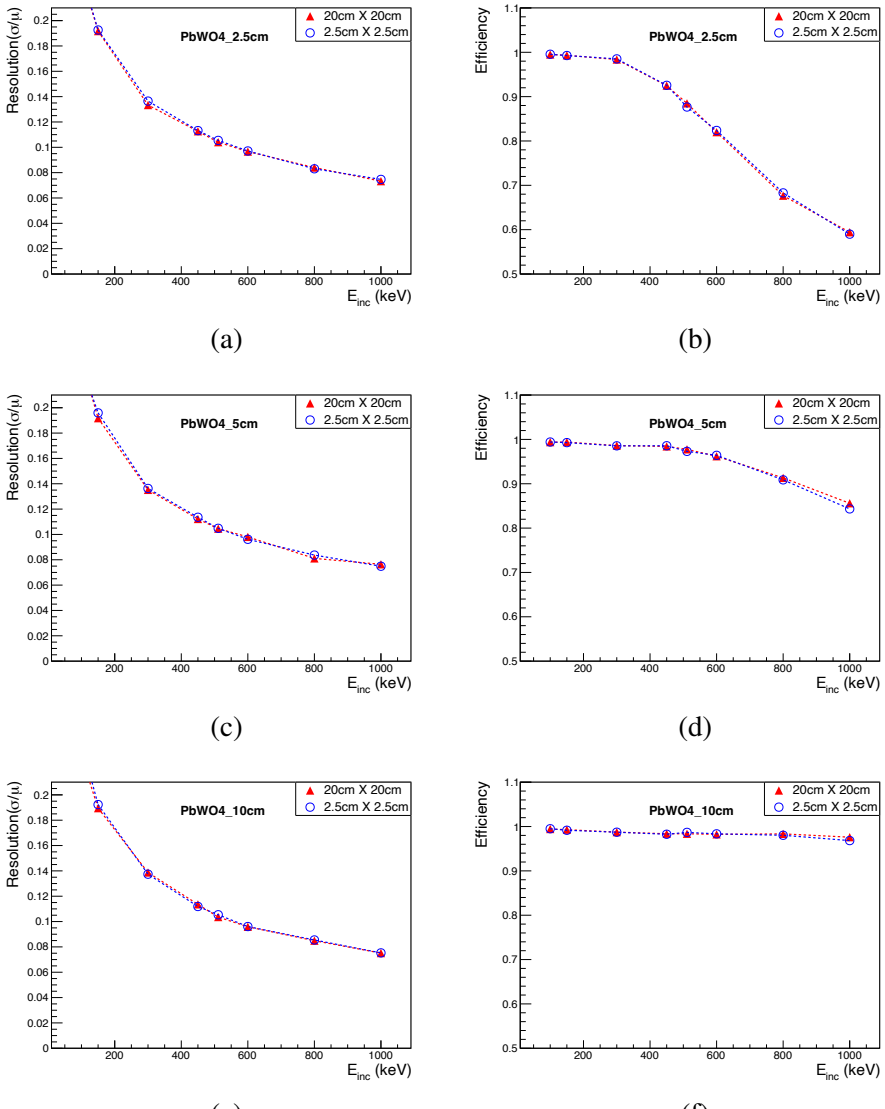

Figure A.42: Comparing the energy resolution (left column) and efficiency (right column) of $PbWO_4$ in two different transverse sizes of the material ($2.5\ cm \times 2.5\ cm$ and $20\ cm \times 20\ cm$). Comparison is shown for 3 different material thicknesses: 2.5 cm (upper row), 5 cm (middle row), 10 cm (bottom row)

For BGO

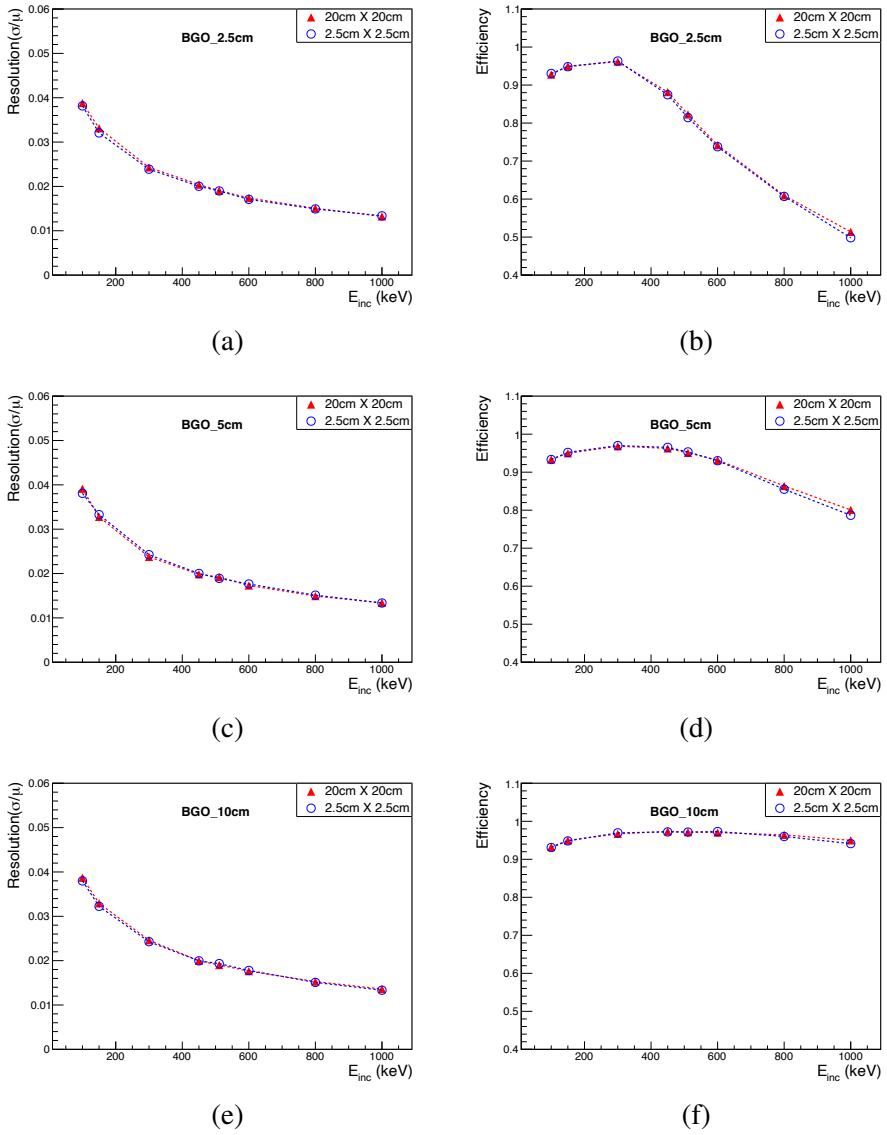

Figure A.43: Comparing the energy resolution (left column) and efficiency (right column) of BGO in two different transverse sizes of the material ($2.5\ cm \times 2.5\ cm$ and $20\ cm \times 20\ cm$). Comparison is shown for 3 different material thicknesses: 2.5 cm (upper row), 5 cm (middle row), 10 cm (bottom row)

LYSO

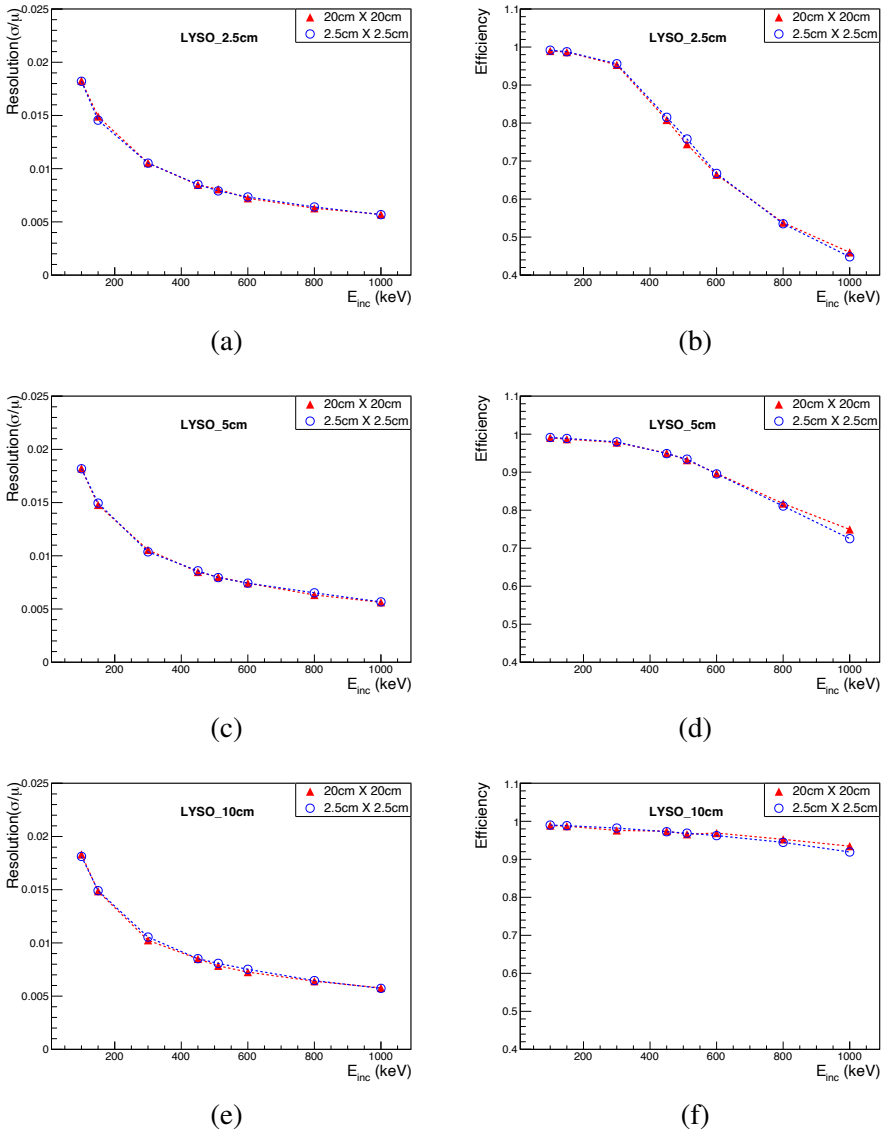

Figure A.44: Comparing the energy resolution (left column) and efficiency (right column) of LYSO in two different transverse sizes of the material ($2.5\ cm \times 2.5\ cm$ and $20\ cm \times 20\ cm$). Comparison is shown for 3 different material thicknesses: 2.5 cm (upper row), 5 cm (middle row), 10 cm (bottom row)

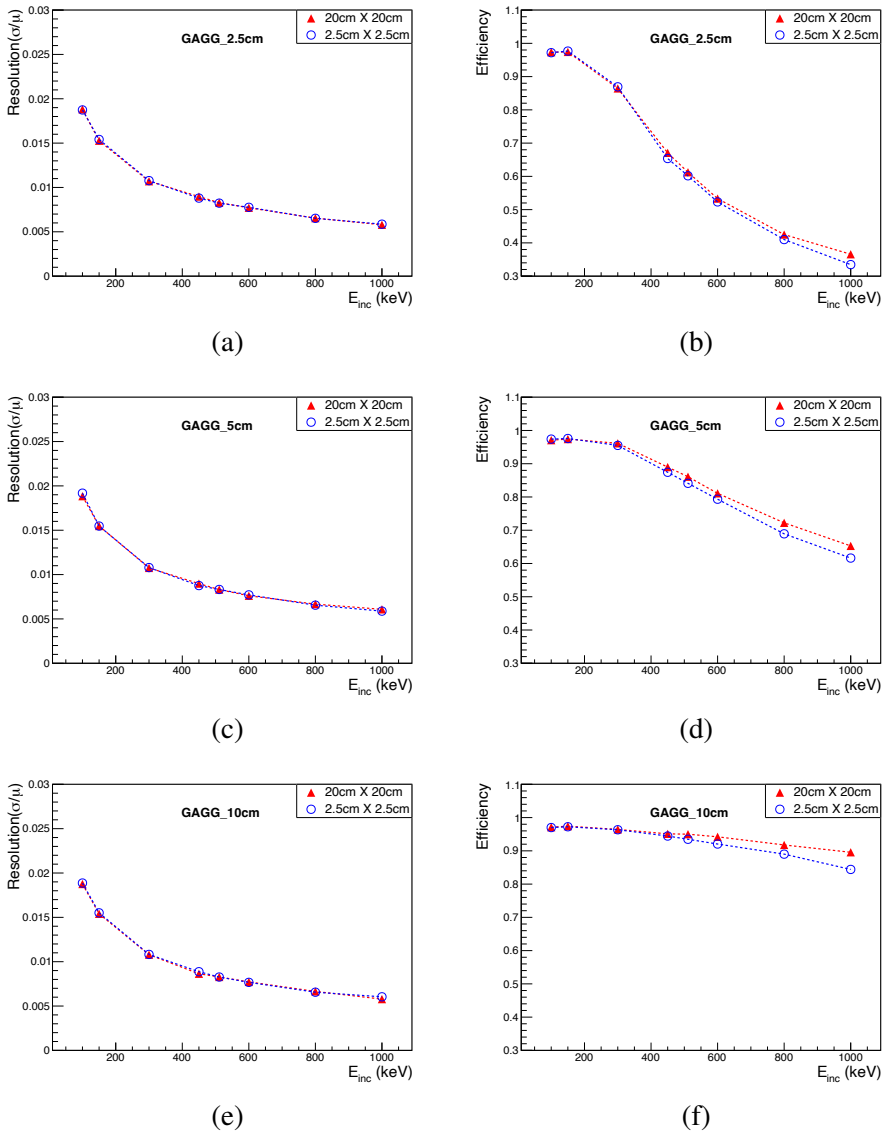

Figure A.45: Comparing the energy resolution (left column) and efficiency (right column) of GAGG in two different transverse sizes of the material ($2.5\ cm \times 2.5\ cm$ and $20\ cm \times 20\ cm$). Comparison is shown for 3 different material thicknesses: 2.5 cm (upper row), 5 cm (middle row), 10 cm (bottom row)

Bibliography

[1] Makoto Asai. Geant4 — documents and examples (version 10.7.p02). https://indico.bnl.gov/event/12272/contributions/51190/attachments/35562/58060/Geant4_DocAndExamples.pdf, 2021. Accessed: 2025-10-18.

[2] V.Ðaniel Elvira. Impact of detector simulation in particle physics collider experiments. *Physics Reports*, 673:1–48, 2017.

[3] Luciano Pandola. Geant4 physics: Particles, processes and physics lists. https://indico.global/event/11040/contributions/103116/attachments/47526/90017/Pandola-Physics-1.pdf, 2024. Presented at VIEnna Workshop on Simulations (VIEWS24), Vienna, April 22-25, 2024; Accessed: 2025-10-19.

[4] Thorben Swirski. *Studies on the Effect of Gas Contaminations in Micromegas Detectors and Production of Micromegas Detectors for the New Small Wheel of the ATLAS Detector*. PhD thesis, Universität Würzburg, 2021. Unrestricted access via OPUS repository.

[5] J. H. Hubbell. Radiation physics. In Robert A. Meyers, editor, *Encyclopedia of Physical Science and Technology*, page 634. Academic Press, 2003. Chapter on coherent scattering etc.

[6] Wikipedia contributors. Scintillation counter — Wikipedia, the free encyclopedia. https://en.wikipedia.org/wiki/Scintillation_counter, 2025. Accessed 14 October 2025.

[7] Wolfgang R. Leo. *Techniques for Nuclear and Particle Physics Experiments: A How-to Approach*. Springer, 2nd edition, 1994. DOI: 10.1007/978-3-642-57920-2.

[8] FindLight. Polarization control: Utilizing the direction of light for optimal optics. https://www.findlight.net/blog/polarization-control/, 2017. Accessed: 2025-10-19.

[9] P. Moskal and et al. Non-maximal entanglement of photons from positron-electron annihilation demonstrated using a novel plastic pet scanner. *Science Advances*, 10(eadp2840), 2025. Published online 17 Dec 2024.

[10] OpenAI. Chatgpt (gpt-5 mini) [large language model]. https://openai.com/chatgpt, 2025. Accessed: 2025-10-19.

[11] CERN Courier. J-PET's plastic revolution. https://cerncourier.com/a/j-pets-plastic-revolution/, Oct 2018. Accessed: 2025-10-19.

[12] P. Moskal and et al. Feasibility studies of the polarization of photons beyond the optical wavelength regime with the J-PET detector. *European Physical Journal C*, 78(11):970, November 2018.

[13] Ana Marija Kožuljević and et al. Study of multi-pixel scintillator detector configurations for measuring polarized gamma radiation. *Condensed Matter*, 6(4):43, 2021. Published 16 November 2021.

[14] Devanshi Arora and et al. Enhancing energy resolution and particle identification via chromatic calorimetry: A concept validation study. In *20th International Conference on Calorimetry in Particle Physics (CALOR 2024)*, volume 320 of *EPJ Web of Conferences*, page 00029, 2025. Published online 7 March 2025.

[15] S. N. Gninenko, N. V. Krasnikov, V. A. Matveev, and A. Rubbia. Some aspects of positronium physics. *Physics of Particles and Nuclei*, 37(3):321–346, 2006.

[16] S. Davidson, S. Hannestad, and G. Raffelt. Updated bounds on milli-charged particles. *Journal of High Energy Physics*, 2000(05):003, 2000.

[17] Pierre Fayet. Effects of the spin-1 partner of the goldstino (gravitino) on neutral current phenomenology. *Physics Letters B*, 95:285–288, 1980. CERN-TH-2800.

[18] L. B. Okun. Mirror particles and mirror matter: 50 years of speculation and search. https://arxiv.org/abs/hep-ph/0606202, 2006.

[19] Lisa Randall and Raman Sundrum. A large mass hierarchy from a small extra dimension. *Physical Review Letters*, 83:3370–3373, 1999.

[20] Lisa Randall and Raman Sundrum. An alternative to compactification. *Physical Review Letters*, 83:4690–4693, 1999.

[21] K. Dulski, P. Moskal, and et al. The J-PET detector—a tool for precision studies of ortho-positronium decays. *Nuclear Instruments and Methods in Physics Research Section A*, 1008:165452, 2021.

[22] CMS Collaboration. Cms experiment — cern. https://cms.cern/, 2025. Accessed: 2025-10-18.

[23] ATLAS Collaboration. Atlas experiment — cern. https://atlas.cern/, 2025. Accessed: 2025-10-18.

[24] CERN. The large hadron collider. https://home.cern/science/accelerators/large-hadron-collider, 2025. Accessed: 2025-10-21.

[25] CERN. Home — cern. https://home.cern/, 2025. Accessed: 2025-10-17.

[26] S. Agostinelli et al. Geant4 – a simulation toolkit. *Nuclear Instruments and Methods in Physics Research Section A: Accelerators, Spectrometers, Detectors and Associated Equipment*, 506(3):250–303, July 2003.

[27] High Energy Accelerator Research Organization (KEK). Kek - high energy accelerator research organization. https://www.kek.jp/en/, 2025. Accessed: 2025-10-19.

[28] Geant4 Collaboration. Geant4: A toolkit for the simulation of the passage of particles through matter. https://geant4.web.cern.ch/, 2025. Accessed: 2025-10-19.

[29] FLUKA Collaboration. Fluka — particle transport simulation. https://www.fluka.eu/Fluka/www/html/fluka.php, 2025. Accessed: 2025-10-17.

[30] MARS Collaboration. Mars — monte carlo simulation code for radiation transport and detector design. https://inspirehep.net/experiments/2660153, 2025. Accessed: 2025-10-17.

[31] John Apostolakis and Dennis H. Wright. An overview of the GEANT4 toolkit. In *Proceedings of the International Conference (2007)*, 2007.

[32] PYTHIA Collaboration. Pythia — event generator for high-energy physics collisions. https://pythia.org/, 2025. Accessed: 2025-10-18.

[33] MadGraph5_aMC@NLO Collaboration. Madgraph5_amc@nlo — matrix element and event generator framework. https://madgraph.phys.ucl.ac.be/, 2025. Accessed: 2025-10-18.

[34] Geant4 Collaboration. Physics reference manual (version 11.x). https://geant4.web.cern.ch/documentation/dev/prm_html/PhysicsReferenceManual/, 2025. Accessed: 2025-10-21.

[35] Geant4 Collaboration. Geant4 physics reference manual: Electromagnetic models – livermore photoelectric model. https://geant4.web.cern.ch/documentation, 2025. Accessed: 2025-10-19.

[36] Geant4 Collaboration. Geant4 physics reference manual: Electromagnetic models – livermore photoelectric model. https://geant4.web.cern.ch/documentation, 2025. Accessed: 2025-10-19.

[37] Geant4 Collaboration. *Scintillation — Geant4 Physics Processes*. CERN, 2025. Book for Application Developers, doc Rev9.2 (section 11.3, Tracking and Physics).

[38] Alexander Howard. Optical photons (geant4 advanced tutorial – optics). https://indico.cern.ch/event/1019834/contributions/4280329/attachments/2210479/3956320/AH_OpticalPhotons_G4advanced_v2021_final.pdf, 2021. Lecture slides, Geant4 Advanced Course, CERN, 6 October 2021.

[39] William H. McMaster. Matrix representation of polarization. *Reviews of Modern Physics*, 33(1):8–28, 1961.

[40] Eugene Hecht. *Optics*. Pearson Education, 5th edition, 2017.

[41] Geant4 Collaboration. *Polarized Electron/Positron/Gamma Incident — Physics Reference Manual, Section 11.3*, 2008. Doc. Rev. 9.2, Physics Reference Manual, Geant4.

[42] D. Habs, M. M. Günther, M. Jentschel, and W. Urban. The refractive index of silicon at gamma ray energies. 2011.

[43] O. Klein and Y. Nishina. On the scattering of radiation by free electrons according to dirac's new relativistic quantum mechanics. *Zeitschrift für Physik*, 52:853–868, 1929.

[44] Germany Merck KGaA, Darmstadt. Sigma-aldrich india website. https://www.sigmaaldrich.com/IN/en, 2025. Accessed: 2025-10-16.

[45] Eljen Technology. Ej-228, ej-230 - fast timing plastic scintillator. https://eljentechnology.com/products/plastic-scintillators/ej-228-ej-230, 2025. Accessed: 2025-10-16.

[46] Sushil K. Sharma, Haytham Al-Makdah, Michal Banaszkiewicz, and et al. J-PET detection modules based on plastic scintillators for performing studies with positron and positronium beams. *Journal of Instrumentation*, 18(02):C02027, 2023.

[47] Hamamatsu Photonics. Hamamatsu photonics official website. https://www.hamamatsu.com/, 2025. Accessed: 2025-10-19.

[48] Geant4 Collaboration. *Geant4 Material Database — Material Names Appendix*, 2024. Book for Application Developers, Section 11.3, Doc Rev 9.2.

[49] National Institute of Standards and Technology (NIST). Materials data repository, 2025. Accessed: 2025-10-16.

[50] B. C. Hiesmayr and P. Moskal. Witnessing entanglement in compton scattering processes via mutually unbiased bases. *Scientific Reports*, 9:44570, 2019.